University of Calgary

PRISM Repository **https://prism.ucalgary.ca**

The Vault Open Theses and Dissertations

2014-09-15

Transport of Ultra-Fine Particles in Suspension through Structured Porous Media

Sajjadiani, Simin

Sajjadiani, S. (2014). Transport of Ultra-Fine Particles in Suspension through Structured Porous Media (Master's thesis, University of Calgary, Calgary, Canada). Retrieved from https://prism.ucalgary.ca. doi:10.11575/PRISM/28518

http://hdl.handle.net/11023/1763

Downloaded from PRISM Repository, University of Calgary

UNIVERSITY OF CALGARY

Transport of Ultra-Fine Particles in Suspension through Structured Porous Media

by

Simin Sajjadiani

A THESIS SUBMITTTED TO THE FACULTY OF GRADUATE STUDIES IN PARTIAL FULFILMENT OF THE REQUIREMENTS FOR THE DEGREE OF MASTER OF SCIENCE IN CHEMICAL ENGINEERING

DEPARTMENT OF CHEMICAL AND PETROLEUM ENGINEERING

CALGARY, ALBERTA

August 2014

© Simin Sajjadiani

ABSTRACT

Transport of suspensions of ultrafine and colloidal particles through porous structures is a common occurrence. Commercial filters are examples of media usually consisting of randomly-oriented fibers in layers to capture large particles. Aquifers, fixed-bed catalytic reactors and hydrocarbon reservoirs are granular formations with high spatial interconnectivity that allow small particles to be carried with the percolating fluid. Often, of interest is how far the particles would penetrate into the structure on advective streams. Experiments were conducted to record the paths of nanoparticles in dilute suspensions through micromodels of porous media. The particles are primarily propelled by hydrodynamic forces through regular arrays of cylindrical posts arranged between two closely-spaced flat surfaces. The setup consisted of the test cell, an inverted microscope, a high speed camera, a data processor, a precise actuating syringe pump, and spherical silica particles (0.2, 0.5 and 1.5 μm diameter) that encapsulated a fluorescent dye. The particle trajectories deviated from the streamlines for particle-free fluids through the domain, and the slip condition was prevalent in an environment in which the fluid velocity field and the particle motion affected each other. The trajectories show evidence of Brownian motion more significantly for the smaller particles that were also dispersed faster through the less porous media. Suspensions were dispersed in the Hele-Shaw section primarily by advection, and the extent was directly correlated to the flow rates and inversely correlated to the particle diameter, the solid volume fraction and the concentration. Axial dispersion was slower in the micro-models than in the Hele-Shaw cell.

ACKNOWLEDGEMENT

First of all, I would like to express my deep gratitude to Professor Jeje, my research supervisor for his outstanding support, patient guidance, enthusiastic encouragement, immense knowledge and useful critiques of this research that without all these I was so lost in this work. Aside from research issues, his fatherly and also friendly attitudes and advices helped me to easily endure the problems and frustrations that come from the nature of research work. Everything he taught me will always help me in my professional and personal life.

I am particularly grateful for the assistance of Professor Matthias Amrein at the microscopy and imaging facilities of the faculty of Medicine. His creative ideas and immense knowledge helped me to understand and apply the best and most effective methods for nanoparticle microscopy and working with micro scale devices as PDMS micro-models. Advices given by other people in lab such as Dr. Michael Shoel who assisted in running the experiments and had great ideas for optimizing the experiments procedures have been a great help.

My grateful thanks are also extended to Dr Javadpour as one of my advisor. His valuable and helpful ideas during this research work and his willingness to give his time so generously has been very much appreciated.

I am very thankful of my defence committee, Dr. B. Maini, Dr M. Foley, and Dr M. Amrein for reading my thesis and helping me to improve the quality of my research by their precious comments and ideas.

I would also like to extend my thanks to the Department of Chemical and Petroleum Engineering, University of Calgary and the Advanced Energy Consortium of the University of Texas at Austin for financial support.

Finally, I wish to have my greatest appreciations to my parents, my sister and my partner Gregory Magnin and also my friends for their support and encouragement throughout my study.

DEDICATED TO MY FAMILY,

GREGORY MAGNIN, REZA SAJJADIAN, HOMA ASSAREH, SIMA SAJJADIAN, POUYAN SHIVA

TABLE OF CONTENTS

Title page……..……....i

Abstract……..….i

Acknowledgement…….....iii

Dedication…….……..v

Table of Contents……..….vi

List of Tables and Figures……..……..ix

Nomenclature…….....xii

CHAPTER 1: INTRODUCTION…….....1

1.1. Scope of study…….…….…….1

1.2. Thesis layout…….……...…….....3

CHAPTER 2: LITTRETURE REVIEW…….....4

2.1. Particle trajectories through porous media……...…….……...…….....4

2.2. Dispersion of suspension of particles suspensions in porous structures…….……..6

CHAPTER 3: EXPERIMENTAL METHODS…….……..12

3.1. Materials and methods……..…….12

3.2. Preliminary Tests……..…..20

3.2.1. Particle Agglomeration experiments……...…20

3.2.2. Photo-Bleaching Experiments……....22

3.3 Micro-model experiments ……..…….23

3.3.1. Trajectory experiments……....23

3.3.2. Dispersion experiments…….…...25

CHAPTER 4: ISOLATED NANOPARTICLES TRAVERSING STRUCTURED MICROMODELS……....27

4.1. Experiments…….....28

4.2. Results and Discussions……..……28

4.2.1. Profiles in the fluid; the kinematics.....……....42

4.2.2. Forces on isolated spherical particles in a viscous fluid; the dynamics……..49

4.2.3. Displacements of Nano-particles in a flowing fluid…….……..54

CHAPTER 5: SHEAR-INDUCED DISPERSION OF COLLOIDAL PARTICLES

5.1. Results…….....62

5.2. Estimation of Longitudinal Dispersion Coefficients……..75

5.2.1. Processing of data for KL ……..……..…….....77

5.3 Discussion……...……...……..83

CHAPTER 6: CONCLUSIONS AND RECOMMENDATIONS……..……..80

REFERENCES……..…...87

APPENDIX A: COMSOL Simulations……96

APPENDIX B: Particle Trajectory Results……..97

APPENDIX C: Potential source of errors……..……107

APPENDIX D: Image recording times……..…….108

LIST OF FIGURES

3.1. Schematic of experimental set-up……...13

3.2. Sketch of the arrays of Micro-Models……....14

3.3. Rate of light absorption in different wavelengths …….....15

3.4. Clusters formation and deformation.....….....17

3.5. Analyzed zone of 5 partitions at the inlet and center of a micro-model…….....22

4.1. Fluid streamlines for micro-model configuration II, generated by COMSO…….....26

4.2. Samples of particle trajectory for 200 nm diameter .....….....27

4.3. Samples of particle trajectory for 500 nm diameter …….....28

4.4. Samples of particle trajectory for 1500 nm diameter …….....29

4.5. Example of particle streaks at high flow rates……....30

4.6. Velocity vector plots for configuration I ……...31

4.7. Velocity vector plots for configuration II .....……32

4.8. Velocity vector plots for configuration III ……..…33

4.9. Simulation of velocity profile between two adjacent pores……....40

4.10. Particles Dimensionless Longitudinal Dispersion Coefficient (KL/Di) …….…….56

5.1 Schematic of test cell area …….…….…….61

5.2. Concentration profile at the inlet area of micro-model II.…….…….…….66

5.3. Concentration profile at the inlet area of micro-model II……...67

5.4. Concentration profile at the inlet area of micro-model II……..……..68

5.5. Laminar flow in the Hele-Shaw cell……...…….…….…….…….69

5.6. The Classical error function concentration profile.....….....74

5.7 Concentration profiles at the inlet and centre of the micro-model …….……76

LIST OF TABLES

3.1. Geometric parameters for the test micro-models……...….11

3.2. Flow conditions in micro-models……...12

4.1. Data for Micro-model Configuration I (Superficial velocity Us = 54.7 µm/s, umax|pore = 176.7 µm/s, umax|plates = 82 µm/s, Reynolds number Repost equals 4.7×10-4)…….…...35

4.2. Data for Micro-Model Configuration II (Superficial velocity Us = 54.7 µm/s, umax|pore = 309.2 µm/s, umax|plates = 82 µm/s, Reynolds number Repost equals 1.64×10-3)…….....36

4.3. Data for Micro-Model Configuration III (Superficial velocity Us = 54.7 µm/s, umax|pore = 231.9 µm/s, umax|plates = 82 µm/s Reynolds number Repost equals 1.23×10-3)……..37

4.4. Tortuosity in micro-model configuration I (5-7-9)…….....51

4.5. Mean particle speeds through micro-models and Dispersion Coefficients……....52

5.1. Relationship between suspension concentrations, solid fraction and population density……....58

5.2. Particle counts in the inlet and inside of micro-model for Conf. I…….....62

5.3. Particle counts in the inlet and inside of micro-model for Conf. I…….63

5.4. Particle counts in the inlet and inside of micro-model for Conf. I…….....64

5.5. Concentration values obtained from experimental data versus concentration values obtained from single factor Boltzmann equation……..…..…..……75

5.6. Inlet Dispersion coefficient values from experimental data for Conf. I, Conf. II and Conf. III……..77

Nomenclature

k = the Boltzmann's constant

T = absolute temperature

K_L = Dispersion Coefficient

PDMS = Poly-Di-Methyl Siloxane

D_p = Post diameter, µm

Re_D = Reynolds number on the basis of the post diameter D_p

$|\overline{u}|$ = Particle speed µm/s

D_h= the hydraulic diameter

Re^+ = Reynolds number on the basis of D_h

L_{hy} = length or distance for flow development

ρ_f = fluid density,

C_D = drag coefficient,

A = projected area, m^2

$\vec{u}$ = velocity vectors for the continuous phase

$\vec{v}$ = velocity vectors for the particle

a = radius of spherical particle

d = shortest perpendicular distance from the wall, diameter of particle

V_{Ls} = velocity of particle based on the displacement µm/s

V_{La},= velocity of particle based on the actual travel distance µm/s

v_x = average velocity derivable from Darcy's law

C= Concentration

L_{ai} = actual distance travelled

$L_{a\ Av}$ = average distances

Pe = Peclet number

l = length scale

D_i = coefficient of diffusion

N = number of particles

P = pressure, kpa

t = time, s

Greek

μ = viscosity, mpa.s

ν_s = superficial velocity, m/s

ρ = density, kg/m^3

θ = contact angle

κ = viscosity ratio

ϕ = porosity, fraction

σ = standard deviation

λ = tortuosity

κ = (radius of spherical particle, a / shortest perpendicular distance from the wall, d)

β (radius of spherical particle, a / principal or characteristic radius of curvature of the wall, $D_p/2$)

CHAPTER 1

INTRODUCTION

1.1. Scope of study

Suspensions of solid particles and/or liquid droplets in fluids are ubiquitous. The air we breathe, as an example, contains ultra-fine particles of dusts, salts, micro-organisms and liquid droplets (Penttinen et al., 2001) that vary with location, time and circumstances but are generally low on a volume fraction basis. On inhaling, such particles pass through and may be captured within the airways of the lung, a structured porous medium. Blood, is also a complex suspension that flows through microvascular networks. In underground reservoir systems and aquifers, tiny particles of clay and other species are displaced with the fluid and are sometimes captured to plug the flow path. For protecting aquifers, suspensions of particles have been injected into formations as tracers to determine potential pathways for migration of pollutants and contaminants (Zheng and Bennett, 1995) from industrial surface operations or piles of waste. Into reservoirs of heavy oils and bitumen, particles of catalysts may be driven to promote degradation of the large molecules and thus lower the viscosity of the hydrocarbon liquids in situ. Patterns characteristic of the above examples are exhibited in deep-bed filtration in which particles are removed from a stream by granules or fibers in highly porous structures like furnace filters or white blood cells are removed by passing blood components (such as platelet rich plasma) through filters.

In these situations, it is of technological interest to understand how particles of micron and submicron sizes move, at pore scale level, through porous media (Lee and Koplik, 1999) and how far they penetrate into the media at prevailing displacement rates of the suspending fluid.

"Well mixed" suspensions of ultrafine particles are seldom homogeneous at the microscopic level, i.e. they do not have uniform and constant concentrations especially in time-scales less than 1 μs as a result of thermal fluctuations or the Brownian effect. At macroscopic scales and for longer relaxation times, the suspensions may look more homogeneous but transients in local concentrations (and associated characteristics such as dynamic viscosity) do occur as a result of advection, diffusion downstream of concentration gradients, short-range surface forces (Israelachvili , 2011) (that lead to rapid cluster formation and dissociation, agglomeration and adhesion to boundaries), or hydrodynamic interactions (collisions and velocity field overlap) between particles.

Of interest is this study are also how concentration (population density) gradients evolve and are manifest at the transition zone of a colloidal suspension that is displacing or is being displaced by a suspension of the same materials but at a lower or zero solid content through a porous media. In the model built for this study flow occurs first between parallel plates (the Hele-Shaw cell) and then through simple-structure representations of porous media. Inter-particle collisions, surface forces or Brownian motion may enhance or impede the spreading of particles in the transition zone between the solvent and suspension for laminar flow within conduits. Dispersion of solutes, rather than particles, in porous media has attracted much more prior attention (Taylor, 1953; Aris, 1956; Saffman, 1960; Perkin, 1963; Rubinstein and Mauri, 1986; Edwards et al, 1992; Vishinski, 2009).

Dispersion of solutes and suspension is within a porous medium is hard to observe quantitatively because the medium is opaque. The flow patterns are also complicated unlike flow through a single straight tube or between parallel surfaces with transparent walls as studies by Taylor (1953) for example. For this reason the porous medium is designed in this work to be thin and accessible to visual inspection and monitoring. The porous media were fabricated by soft lithography as well-defined structure or porous micro-chips. The flow through the micro-chips is laminar but the streamlines are not straight as in a tube. The porosity (or void volumes) and the arrangement of the obstacles (or posts) were changed from one test cell to another. The test cells were also thin and the walls were transparent for observations under a microscope.

1.2. Thesis Layout

The rest of the thesis starts with a literature review on particle motion and dispersion in porous media. Chapter 3 deals with the different types of micro-chips experiments designed to study dispersion and particle motion in micro-chips. Also, in this chapter image analysis and data processing for each experiment are explained.

In Chapter 4 and 5 the observations, results, and analysis approaches to single particle motion and dispersion of high concentration particle suspensions in porous media are presented. Conclusions and recommendations for future work are presented in Chapters 6.

CHAPTER 2

LITERATURE REVIEW

In this chapter, the literature study on single particle trajectories through micro - models and shear induced dispersion of high concentration particles suspensions in porous structures are presented.

2.1 Particle trajectories through porous media

The typical porous medium is a complex structure of pores and cavities within arrangements of irregular and opaque particles or fiber strands. Tracking submicron and colloidal particles through such geometry is not often feasible and investigators have attempted to understand the dynamics by resorting to micromodels (Karadimitriou and Hassnizadeh, 2011). These are effectively two-dimensional patterns or thin slices of a porous medium mounted within parallel optically-clear plates. Such an arrangement allows visual observation of fluid flow through interstices between solid elements and the displacement of one fluid by another. When there is an interface for immiscible fluid displacement, the fluids near the interface move in response to local capillary forces and applied pressure. The flow through the pores in this region is spatially integrated at the front, even if unstable, and the displacement qualifies as 2-dimensional flow (Wilson et al., 1988). When particles much smaller than the pores are in suspension and their movements are to be tracked in miscible displacement, as is of current interest, the flow of the suspending fluid (assuming it is, not a gas at low pressure) is described at microscopic level and the Navier-Stokes equations would be applicable. At the pore-level scale, the flow is 3-dimensional and not 2 Dimensional as often it is assumed. Moreover, the irregular and uneven internal boundaries for the flow are difficult to characterize. The resulting fluid flow patterns would be unique for each arrangement and location, and generalizations about the flow

dynamics, and the influences on particles in motion, would not be easy to identify. It is for these reasons that micromodels are often designed as structured arrays of short cylindrical post (typically in triangular or rectangular arrangements) separating two parallel transparent plates.

In other studies, highly porous filters have been modeled as an ensemble of cylinders acting as collectors (Shapiro et al., 1991) or as arrays of infinitely long cylinders oriented parallel or normal to the direction of flow of suspensions. An example of the latter involves separation of particles by size in some micro-fluidic devices have also been modeled by displacements around cylinders. Numerous analyses have been carried out to predict trajectories for suspended particles around obstacles but there have been few experimental results to provide validation. (Happel, 1959; Kuwabara, 1959; Gordon, 1978; Sangani and Carios,1982; Drummond and Tahir, 1984; Bron, 1993; Wang, 2003; Angeli et al., 2010) A micro-model is valuable for observing and tracking particles (Auset and Keller, 2004) but the flow characteristics in the structure require attention as the streamlines for the fluid may not be coincident with the particle trajectories of suspended isolated particles as may be anticipated for an ideal filter. Di Carlo et al. have suggested that fluid and particles interact to cause particles to follow paths unanticipated in micro-channels.

2.2 Dispersion of suspensions of particles in porous structures

The dynamics of suspensions depend on the concentration or volume fraction of the solid particles. (Eckstein et al., 1977; Acrivos et al. 1992; Ramachandran, 2013), the current study is restricted to systems of dilute colloidal suspensions with solid volumetric fractions φ less than 20%. The particles are close enough to interact hydrodynamically but are yet distinct that distribution patterns can be observed. The investigative approach taken follows those earlier reported by Taylor (1953, 1954) on the mixing of a solute (the "point size" particle) in solution with a solvent downstream as they both flow slowly in a straight circular tube. Taylor's analysis has been generalized by Aris (1956), Horn (1971), Brenner (1980, 1982) and his collaborators (Brenner and Edwards, 1993). While focusing on fluids in laminar flow in straight tubes, the investigators have shown that the dispersion of a solute in a solvent is facilitated by advection downstream and radial diffusion (or thermal fluctuations). Random bombardment of fluid molecules (because of their thermal energy) against the particle suspended in it are named as Brownian diffusion forces and results in irregular wiggling motion of the particle which is called Brownian motion. These forces are proportional to kT /a where k is the Boltzmann's constant and T is the absolute temperature. When the solute particles are finite-sized (colloidal and non-colloidal in the 0.1 – 20 μm size range), collisions between particles, interactions of their velocity fields and Brownian motion, in varying proportions, contribute to the shear that determines the rates of dispersion (Batchelor, 1976; Acrivos et al., 1992).

The migration behaviour of colloids representing fine particles in solution and dissolved solutes in porous media are relatively different. (Sirivithayapakorn and Keller, 2003), for instance it has been shown that colloids can travel at a greater distance than predicted by typical approaches for tracer cases (McDowell et al., 1986; Champ and Schroeter, 1988). Also in breakthrough column

experiments it has been observed that colloids arrive faster in the effluent and have earlier breakthrough compared to solutes dissolved in a solvent (Champ and Schroeter, 1988; Niehren and Kinzelbach, 1998). Numerous efforts have been made during the last two decades in order to predict colloidal transport using laboratory and field studies as well as numerical models and unlike Taylor (1953) and other dispersion theories mentioned above for tracer cases, the finite size of particles has been considered as an important factor effecting the fate of particles in porous media (James and Crystopolous, 2003). In migration of particles in a fluid flow, if the density of particles is the same as the density of fluid in which are immersed they are called neutrally buoyant particles and the force of gravity has no effect on their motion. In many colloid transport studies this type of particles has been used to study the physics of transport and the dispersion phenomenon.

During the three last decades, it has been a challenging problem for scientists to find a model of particle dispersion in porous media. The main reason has been the lack of sufficient information on particle interactions with fluid or solid matrix of porous medium to precisely define parameters as effective particle velocity and effective particle dispersion and define an accurate process for dispersion of particles in porous media.

Theoretical models for particle transport behaviour in porous media generally hypothesise that particles experience the same physical processes that affect tracer particles transport in a porous medium, specifically advection, hydrodynamic dispersion and mass transfer between the fluid and solid matrix of porous medium (Bradford et al., 2002).

The migration behaviour of particles in porous media is complex and deals with multiphysical processes. Particle characteristics like shape, size, mass density, and surface properties; fluid

properties like viscosity, density, pH, ionic strength, and porous media characteristics like pore topography, morphology, and pore wall surface forces, and operating conditions such as flow rates and temperature would control the fate of a particle moving through the domain, and whether it passes through or is captured and retained locally. [Javadpour et al., 2011]

As mentioned above it has been observed that colloids have an earlier breakthrough compared to solute tracers, in column experiments (Niehren and Kinzelbach, 1998). Reimus (1995) hypothesized that this effect results from the larger size of colloids compared to solutes. They explained that larger particles diffuse too slowly to enter the slow velocity regions in fractured medium. Niehren and Kinzelbach [1998] performed column experiments to compare the behaviour of tracers and colloids. They suggested that the pore diameter should be several times bigger than particle diameter until the particle could pass through it. They also concluded that the highly reduced matrix diffusion of colloids compared to tracers is the most important factor of difference in transport behaviour between them.

Some other researchers also confirmed that the observed different behaviour of tracers and colloids is due to a size-exclusion effect (Sirivithayapakorn and Keller, 2003)

DiMarzio and Guttman (1970) applied the concept of size exclusion to explain their theory of particles separation by flow. Later Avogadro and de Marsily [1984] concluded that colloid transport in porous media might be comparable to the transport process that happens in hydrodynamic chromatography. In the same context, Sirivithayapakorn and Arturo Keller (2003), applied micromodels as the representatives of porous media for their experiments and by direct observations at the pore-scale, presented experimental evidence of the effect of colloid exclusion from areas of small pore sizes. They suggested that for a particle to enter a pore, the

ratio of a pore throat to colloid diameter should be around 1.5 and colloids larger than about 1–2 μm are excluded from most small pore throats. They concluded that larger colloids will travel through a reduced number of pathways thus they will have less resident time compared to smaller particles which will have a corresponding effect on average particle velocity and also dispersion. They confirmed the work of Grindrod et al. (1996) that had proposed that the average velocity of colloids is larger than of a tracer and the earlier colloid breakthrough can imply a lower effective dispersion rate. James and Chrysikopoulos (2003) derived mathematical formulations for velocity distribution and dispersion of hard sphere neutrally buoyant particles flowing in a saturated fracture. They showed that the size exclusion of particles increases the particle effective velocity due to excluding particles from the slowest portions of velocity profile and decreases its effective dispersion coefficient.

Auset and Keller (2004) used manual trajectory analysis to obtain similar results for different network arrangement in their micromodels. They suggested that dispersion coefficient and dispersivity are controlled by pore space geometry and positively correlated by colloid size. They showed that larger particles experience faster velocities due to their preferential paths through centre stream lines resulting in more straight trajectories and therefore lower residence times. In this context, Baumann et al. (2010) conducted transport experiments in silicon micromodels and provided quantitative data on colloid dispersion at pore scale. They found that pore topology is the dominant controlling factor among other effects. In addition, they reported that increasing ionic strength and flow velocity positively affects the dispersivity and the colloid size has a decreasing effect on the colloids dispersion.

This study reports the effects of shear-induced diffusion on dispersion, and how dispersion changes when a suspension flowing in a Hele-Shaw cell transitions abruptly into a micro-model

representation of a porous medium. The primary differences between the two physically juxtaposed domains are the void fractions (reduced) and the surface area in contact with the fluid (increased). In each domain, particle interactions would be expected to depend on the solid volume fraction that is related to particle population density. Under such circumstances, it may be then be anticipated that local values for the dispersion coefficient, K_L, would vary with position in the zone of transition from a "uniform" suspension to particle-free solvent downstream of the flow. Such variations are not of present concern, and thus the results to be presented are global or space-averaged values for each set of experimental conditions.

The domain of flow is a highly simplified model of a fibrous filter or a packed bed of consolidated or unconsolidated sand that are normally randomly organized structures. The particles are small enough to be subjected to thermal fluctuations (Brownian motion). They collide with each other and are carried through tortuous paths in the porous medium. The particle distribution, at the microscopic level, is considered homogeneous but particle motions are unsteady. Such a system has not been much examined. Griffith and Stone (2012) analyzed the dispersion of colloidal suspensions in a straight, uniform-bore, circular tube. They concluded that the rate of axial dispersion for dilute colloidal suspensions is reduced significantly, compared to dispersion of molecular solutes in a similar system, as a result of lateral particle migration. It was not exactly clear what (for them) constituted dilute suspensions and what particle sizes would be subject to Brownian motion since they made reference to 20 μm diameter particles in 200μm radius channel for validation. Ramachandran (2013), in a recent paper on dispersion of non-Brownian particles in a straight circular tube, concluded that for concentrated suspensions (20-50% by volume), the effective diffusivity or dispersion coefficient decreased monotonically with increase in particle concentration. Significant lateral particle migration was reported by both

Ramachandran and Frank et al. (2003) at high particle concentrations (above 20%) and migration was not significant at concentrations below 5%. This last result would suggest that, for the conditions of this study, net lateral particle migration would be insignificant.

CHAPTER 3

EXPERIMENTAL METHODS

The experimental set-up and methods are presented in this chapter. The apparatus and protocols for runs, including the assembly of micro-model and preparation of suspensions, are described. Issues that needed to be resolved such as undesirable agglomeration of particles and "bleaching" of fluorescent particles being tracked are discussed. Finally, the procedures for collecting data for isolated particles in dilute suspensions and for dispersion of particles in concentrated suspensions are presented.

3.1. Materials and Methods

The apparatus

A schematic of the experimental set up is shown in Figure 3.1 (a). It consists of four components; the test cell, an inverted microscope, image recording and storage devices and an actuating pump. The test cell, viewed from above, is shown in Figure 3.1 (b). It comprises a rectangular channel between two parallel plates that are 28 mm long and 1 mm wide. The spacing between the plates is 20 μm. The bottom plate with sides is fabricated from Poly-Di-Methyl Siloxane (PDMS) from silicon wafer molds that have cylindrical holes etched in a region in prescribed patterns by soft lithographic methods (Javadpour and Jeje, 2012) When cured and stripped from the mold, the clear polymer becomes the bottom plate and side walls. A section of the plate has cylindrical posts that are 5 or 10 μm in diameter and uniformly 20 μm long projecting out. The posts are in triangular arrays in this study and are within a 1 x 1 mm square

area, as shown in Figure 3.1 (b). The top plate of the test cell is a glass cover slip, with injection and withdrawal ports pre-drilled through. The micro-model of a porous medium is where the posts are located; and the 10 and 17 mm long sections on either side of this area constitute Hele-Shaw cells through which flows stabilize before entering and after leaving the micro-model. Sketches of the arrays of the posts are in Figure 3.2 (a), (b) and (c). The arrays are identified as configurations I, II and III in subsequent references. It is important to note that the axes of the posts do not form vertices of equilateral triangles. Test cell parameters are listed in Table 3.1. The solid density is the fraction of the test section occupied by the posts, or 1 minus the porosity. The values were between 0.13 and 0.35 for the configurations. For a typical porous medium, areas ascribed to the bounding walls (if present) are negligible fractions of the total surface area exposed to contacting fluids. This is not the case for the micromodels in Table 3.1. Contributions of the bounding surfaces to the observed velocity field that developed and to the viscous resistance to flow in the system cannot be dismissed.

The second component of the setup is an inverted light microscope (ZEISS / AXIOVERT 200, 40 Lens: plan-Apochromat 40X/1.4 oil) equipped with a high speed digital camera (Andor Neo, SCMOS). The objective was focused at the mid-plane of the test cell. The depth of field was ~ 10 μm and the field of view was 895 x 850 μm. The high speed camera was operated at a frame rate of 30 per second and 25 ms exposures. Both the camera and a computer constitute the image capture and storage devices. The fourth piece of the apparatus is a calibrated syringe pump (model 341B, SAGE Instruments) for drawing fluid at constant volumetric rates out of the test cell. The cells were previously cleaned and saturated with deionized water at room temperature, density ~ 1000 kg/m^3.

The particles used were spherical silica particles encapsulating a fluorescent green dye (Microspheres-Nanospheres). The surfaces were electrically neutral. The density was 1448 kg/m^3 and the diameters were 0.2, 0.5 and 1.5 μm. Particles in the size range used are at or below the resolution limits for optical microscopes, hence the dye trapped within. When exposed to light of an appropriate frequency, the trapped dye fluoresces and thus allows the particles to be located. Fluorophores, however, undergo photon-induced chemical damage and covalent modification leading to fading and ultimately loss of the ability to be excited on continuous exposure to light. This phenomenon is photo-bleaching. The dye in the silica particles used required 3-4 minutes of continuous illumination to start fading and over 5 minutes to be unexcitable. Photo-bleaching did not occur for runs lasting less than 2 minutes.

Since the particles are denser than water, the prospect of gravity displacing particles from the focus of the microscope was considered. Settling was only detected in particle suspensions in a Ultraviolet-Visible light spectrometer only after 20 minutes (Figure 3.3). Particles moved through the field of view in 15 to 120 seconds. Of importance also was that there were no agglomerates. The 5% v/v suspensions purchased were subjected to ultrasonic vibrations to dissociate clusters before being diluted to concentrations of ~ 10^8 per ml. At this concentration, particles moved singly.

Presented in Table 3.2 are the flow conditions. Three different flow rates give superficial (and thus average) velocities of 6.13, 14.88 and 54.68 μm/s at any cross-section of the channel. The corresponding pore velocities and the Reynolds numbers relative to the diameters of the posts of the test sections are also shown in the table. The Reynolds numbers are less than 2×10^{-3}.

Table 3.1 Geometric parameters for the test micro-models

Configuration	Post diameter, D µm	Post separation in rows, y µm	Centre-line row separation, x µm	Solid density or (1-porosity)	Exposed area of plane wall to area of posts
I	5	7	12.65	0.13	0.84
II	10	5	15.26	0.34	0.48
III	10	8	17.86	0.24	0.77

Table 3.2 Flow conditions in the micro-models. Superficial velocity is injection rate / channel cross-sectional area, pore velocity U is the average value between the posts, and Re_D is the Reynolds number on the basis of the post diameter D_p (= $U\rho D_p/\mu$); ρ and μ are respectively the density and viscosity of the fluid.

Flow conditions			Micro-model Configurations					
			I	I	II	II	III	III
Category	Injection rate, (10^{-5}) $\mu m^3/s$	Superficial Velocity, $\mu m/s$	Pore vel., $\mu m/s$	Re_D (10^5)	Pore vel., $\mu m/s$	Re_D (10^4)	Pore vel., $\mu m/s$	Re_D (10^4)
Slow	1.23	6.13	10.5	5.25	18.38	1.84	13.79	1.38
Interm.	2.98	14.88	25.5	12.8	44.63	4.46	33.48	3.35
High	10.9	54.68	93.74	46.9	164.04	16.4	123.03	12.3

(a)

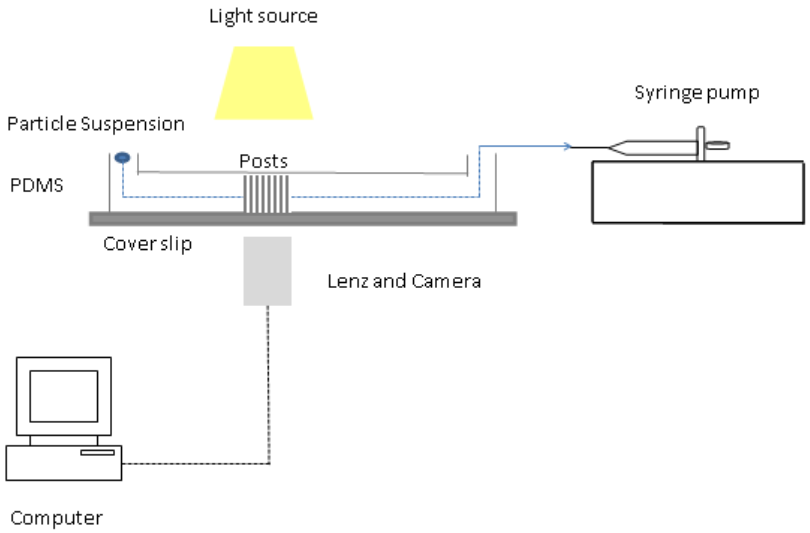

(b)

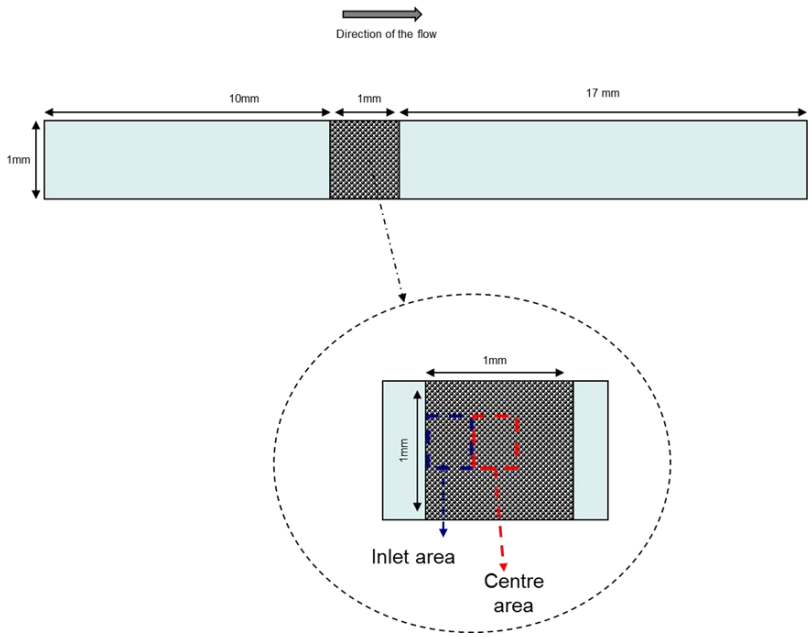

Figure 3.1 Schematic diagrams of the micromodel setup. (a) The apparatus consists of the test cell, a syringe pump, an inverted light microscope, a high speed camera and a computer. (b) A schematic diagram of the test cell in top view.

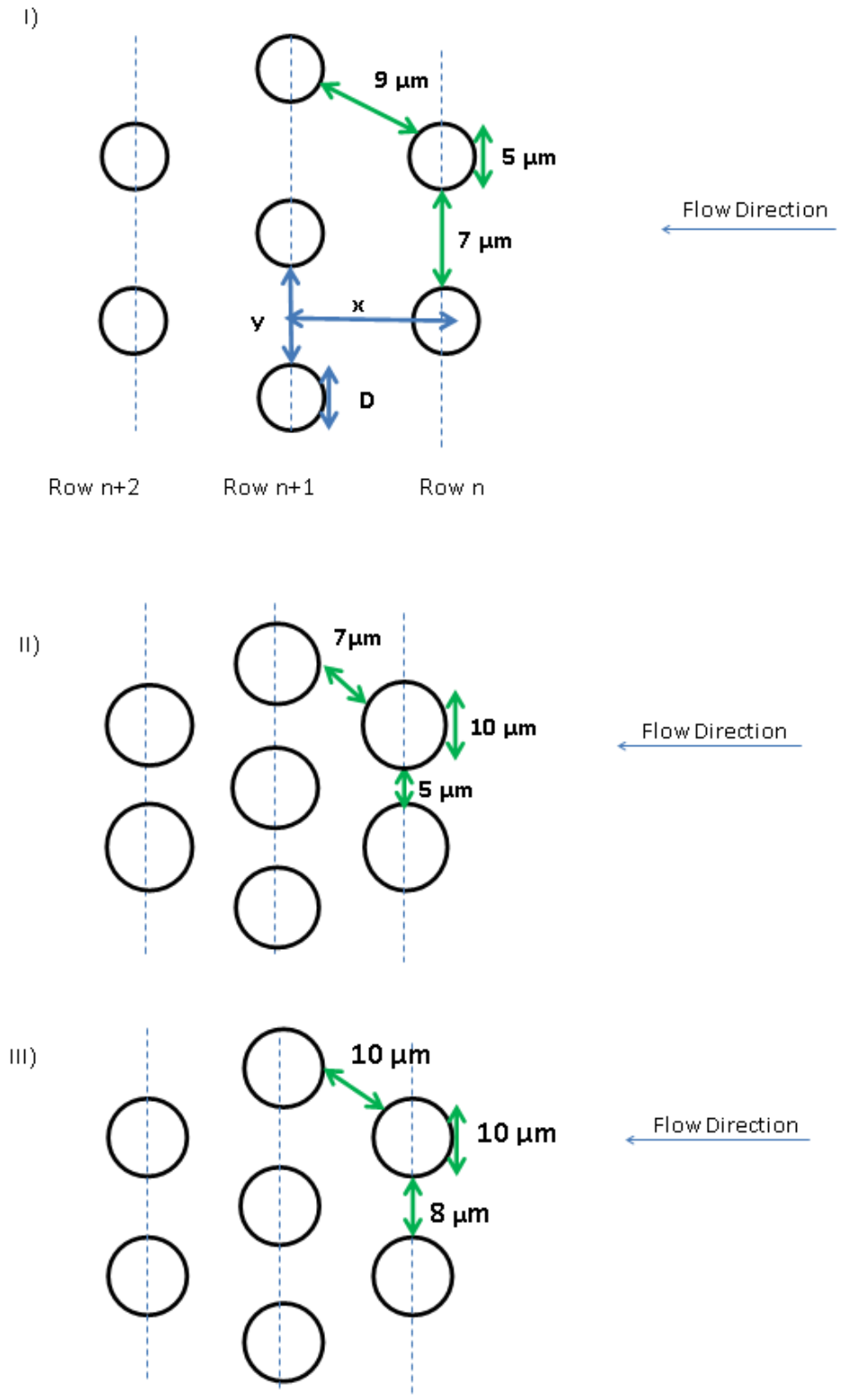

Figure 3.2 The configurations for the micromodels, in triangular arrays

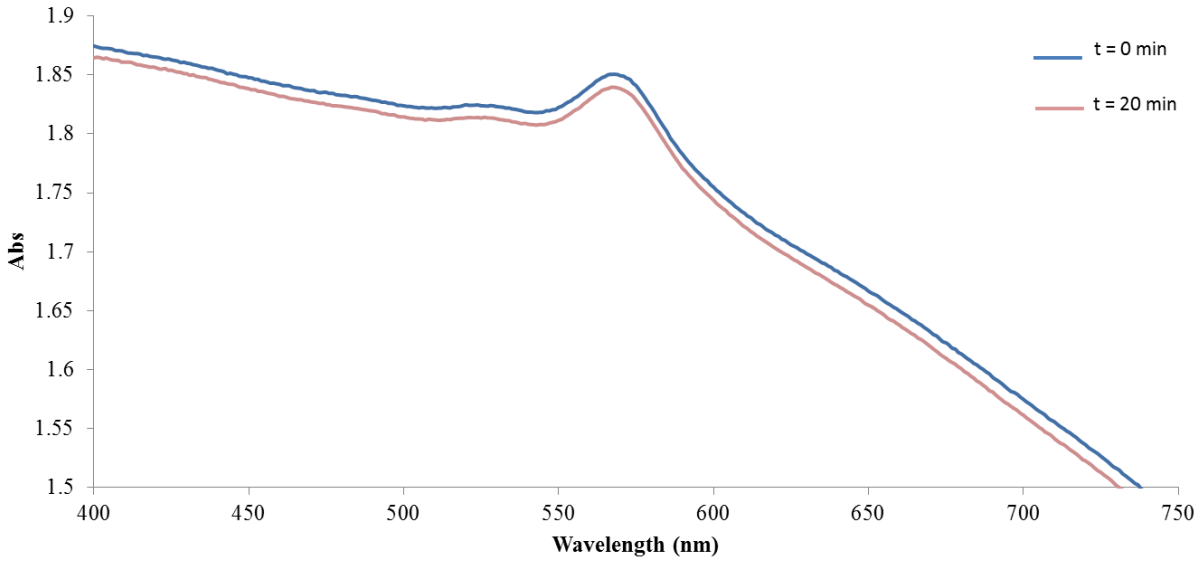

Figure 3.3 Rate of light absorption in different wavelengths for 1500nm particles after 20 minutes **(**Generated by UV-Visible Spectroscope)

3.2. Preliminary tests

It is important for this study to ensure that the particle suspensions are mono dispersed or relatively free of clusters. Aggregates of unknown size distribution would lead to an increase in settling rates, arbitrary distortions of particle trajectories and bright spots that overwhelm fluorescence from adjacent single particles. Photo bleaching is also a phenomenon that would interfere with monitoring the particle path lines and thus data collection.

3.2.1. Particle Agglomeration

There is a natural tendency for the silica particles to form clusters. The clusters are dissociated by placing the suspension samples in an ultra-sonic vibrator for 45 minutes, as earlier described. To check the rates at which clusters re-form, a 20μl drop of 200nm particle suspension was placed on a microscope glass slide and a cover slip (22mm×22mm) was placed on the drop. Fluid squeezed out from around the cover slip is cleaned up and nail polish was used to stick the cover slip to the glass slide.

The prepared slide was placed horizontally under the objective of the microscope (ZEISS /AXIOVERT 200, 40 Lens: plan-Apochromat 40X/1.4 oil) equipped with a digital high speed camera (Andor Neo, SCMOS) mounted directly onto the eyepiece. Images were taken every minute from the particle motions. The experiment was repeated several times at the same and different suspension concentrations. As shown in Figure 3.4, the particles remained substantially isolated over the period of observation.

The small clusters noted in Figure 3.4 were not stable and gradually disintegrated. This confirms that the particles would remain separated for the duration of the flow experiments.

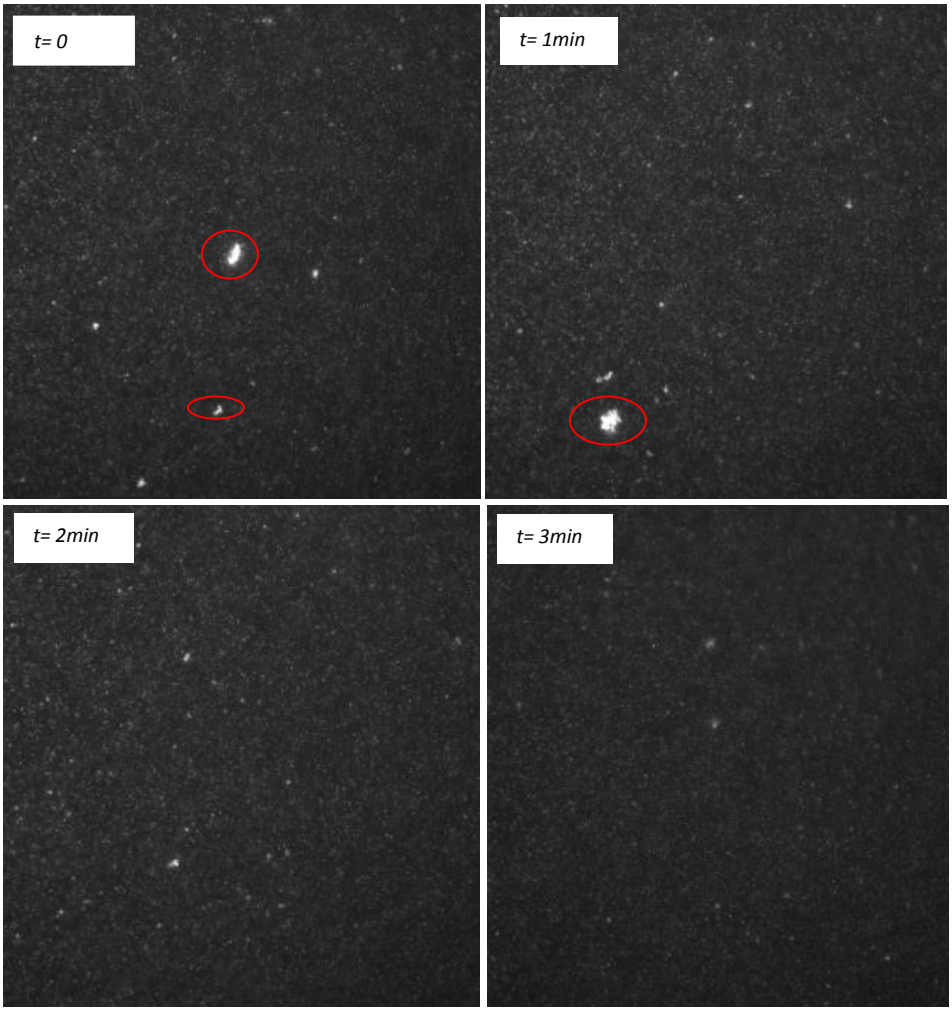

Figure 3.4 Clusters formation and deformation, images were taken every minute. Red circles highlight particle clusters

3.2.2 Photo Bleaching

The displacement of tiny particles will be tracked in this study. The particles are < 2μm in diameter and they are difficult to resolve in regular microscopy. In order to track them, the particles have been filled with material that fluoresces on illumination with light of certain wavelengths. However, due to photon-induced chemical damage and covalent modification, a fluorophore can permanently lose the ability to fluoresce. This phenomenon is called photo-bleaching or fading. Transition from an excited singlet state to the excited triplet state may lead to fluorophores and other molecules interactions to produce irreversible covalent modifications. The triplet state is relatively long-lived compared to the singlet state, thus, chemical reactions with components in the environment will be more probable for the excited molecules.

The molecular structure and the local environment are important parameters affecting the average number of excitation and emission cycles that happen for a particular fluorophore before photo-bleaching. Whilst some fluorophores bleach quickly after emitting only a few photons, more robust fluorophores can experience thousands or millions of cycles before bleaching.

Preliminary experiments were conducted to confirm that photo-bleaching would not be a factor in the study as follows.

Samples used for this set of experiments were handled exactly the same way as for those used in the agglomeration experiments. The focus was on 200nm diameter particles as these were most susceptible to photo-bleaching maybe because of the limited quantity of fluorophore each particle contains. Pictures of illuminated particles were taken every 30 seconds over an interval of 10 minutes and the bright spots were counted. A steadily decreasing number of bright spots would suggest that progressively fewer particles are fluorescing or more particles are settling and

moving away from the plane of focus. The plane of focus was varied from top to bottom and pictures taken at different levels of the field.

The average intensity of images, using ImageJ software, was determined for both top and bottom focus planes. About 3-4 minutes were required for the particles to start to lose their intensity at both levels. And it took about 5 minutes for photo-bleaching to occur. Since the duration of each experimental run for transport of particles through the micro model is less than 2 minutes, photo-bleaching is not an issue of concern. Occasionally, it is observed that a particle's emitted light "disappears" during a run. This is not ascribed to photo-bleaching. Particles in transit may have their emitted light blocked by other particles at higher planes or the particles may have moved out of focus through collisions or gravitational pull.

3.3 Micro-model Experiments

Particle trajectory and front experiments presented in this section were conducted to obtain the core required data for this study to calculate the local particle average velocities and understand the particle behavior compared to flow streamlines.

3.3.1 Trajectory experiments

The displacements of particles were obtained from this set of experiments. The experimental set-up is explained in section 3.1 and illustrated in Figure 3.1.

The micro-model was placed under an inverted light microscope (ZEISS / AXIOVERT 200, 40 Lens: plan-Apochromat 40X/1.4 oil) equipped with a high speed digital camera (Andor Neo, SCMOS). Particle suspension was sucked in with a precise syringe pump (model 341B, SAGE Instruments) at pre-specified rates. Migrated particle were visualized through an inverted light

microscope and images were recorded at a frequency of 30 frames/s. There was no control on temperature, but the room temperature was kept constant (20±2 $^{\circ}$C).

To completely presaturate the micro-model with water, At least 5 pore volumes of the alcohol were flushed through the model to reduce the hydrophobic properties of PDMS. Then 15 pore volumes of deionised water were pulled back to make sure all the alcohol is removed from the system and the micro-model is completely saturated with deionised water. After obtaining the steady state flow, particle suspension was poured into the inlet hole with a micropipette and the drops of particles were sucked back from the inlet hole into the model. The dispersion of the particles, their trajectory and their interactions with micro-posts were observed under an inverted-light microscope at a half-depth focal point of the channels (Javadpour and Amrein, 2011).

Image processing and analysis was then performed using ImageJ®software. Each stack contained 200 images taken at a frequency of 30 frames per second. In all experiments, particle tracking was performed for at least 35 particles at each region of the pores. ImageJ manual tracking module was used to prevent false assignments of particles and to obtain more precise, detailed and complex trajectories.

3.3.2 Dispersion Experiments

These experiments were conducted to quantify particle dispersion in porous media. High concentration suspensions were used in order to better visualize the front and boundary of particles proceeding in porous media.

The experimental set-up used for this set of experiments is exactly the same as particle tracking experiments. As the leading edge of fluid containing particles just reached the front row of posts for the micro-model section, a picture was taken and the camera was immediately moved to the center of the micro-model section (with field-of-view centered about 500 μm from the inlet) to take another picture with the advancing front and the zone upstream showing in the frame. For this distance into the test section, the leading edge of the particle suspension would have traversed in excess of 15 cycles from inlet and any flow-induced transients would have dissipated. The area of the field-of-view recorded was 895 by 850 μm. The particles images were for the entire cross-section of the test cell, i.e. greater than 20 μm depth of field, and they were sharp.

From the recorded images of the inlet region, particles were counted in an area of 150 μm along the flow direction and 85 μm in the transverse direction. The lengthwise side was divided into 5 sections, each 30 μm long. For images at the center of the micro-model, the section length used was 34.5 μm, 45 μm, and 39.7 μm for Configuration I, II and III respectively to compensate for the areas occupied by the posts and keeps the fluid volume the same for each section. Each front or transition region should ideally exhibit a concentration profile as illustrated in Fig. 3.5. The particle count for the injection region is used to divide the count for all the other sections, that is, to normalize other values outside and inside the micro-model region.

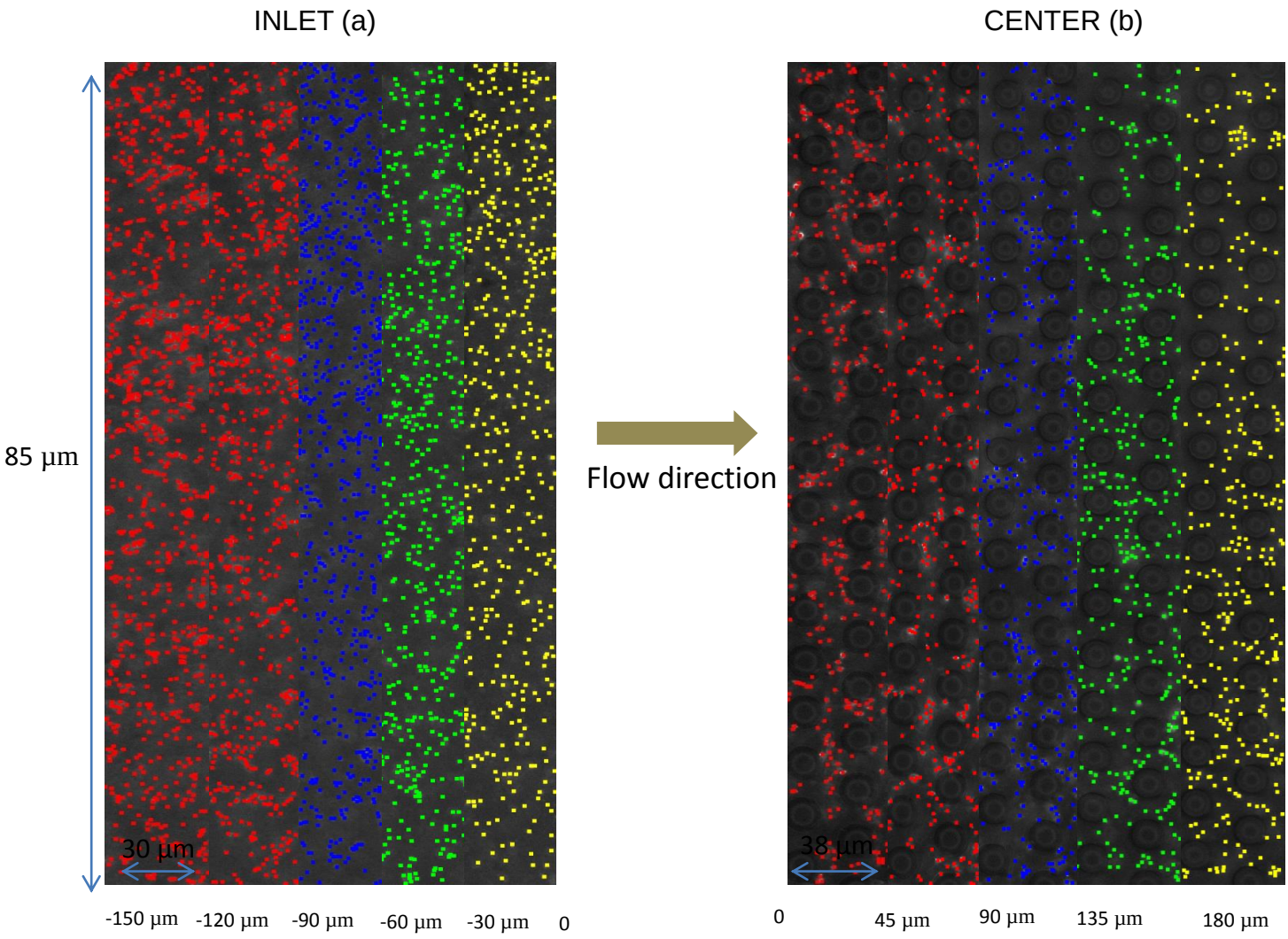

Figure 3.5 Five partitions selected at the Inlet (right before posts start) and Centre Area (centre of the porous section) of a micro-model. Particles were counted in each partition and indicated with red, red, blue, green and yellow colour respectively

CHAPTER 4

ISOLATED NANOPARTICLES TRAVERSING STRUCTURED MICRO-MODELS

The trajectory analysis of single particles traversing the micro-models and the corresponding dispersion coefficients are discussed in this chapter. Particles being displaced within a viscous fluid in motion are under the effect of hydrodynamic forces. For the present system, the flow is in the horizontal plane and gravity force is neglected. It is assumed that the particles are isolated and not subject to other short and long range electromagnetic and surface forces. The silica particles, density of 1448 kg/m^3 and 0.2, 0.5 and 1.5 μm diameter, are small enough to reflect the effects of Brownian forces due to thermal fluctuations within the continuous phase – water at a density ~1000 kg/m^3. The domain, within which flow occurs, the micro-model, is herein described as cylindrical posts (5 or 10 μm diameter) arranged in a staggered (triangular) array between two transparent parallel plates. Cross-sections and corresponding dimensions were shown in Fig. 3.2 for the three configurations used and the parameters were presented in Table 3.1. the solid density is the fraction of the test section occupied by the posts, or 1 minus the porosity. The values were between 0.13 and 0.35 for the configurations. A typical porous medium has a small fraction of the total surface area ascribed to the bounding walls. For micro-models, the areas of the confining surfaces are usually insignificant compared to other areas within the domain. The ratios for the current system, as shown in Table 3.1, are substantial and the contribution of the flat surfaces to the viscous resistance to flow may not be negligible.

The separation between the parallel surfaces is 20 μm. up and downstream of the test section with posts are zones of lengths 10 and 17 μm for flow development. The upstream section is to allow the attainment of a fully developed, laterally-uniform Poiseuille flow before posts are

encountered. The downstream region is to ensure a uniform flow prevailed along the width of the model as fluid emerged from the test section. The third experimental variable (after particle size and array patterns) is the flow rate of the fluid through the domain. As shown in Table 3.2, fluid was admitted at three different flow rates to give superficial (and thus average) velocities of 6.13, 14.88 and 54.68 μm/s at the approach to the first row of posts. Corresponding pore velocities and the Reynolds numbers relative to the diameters of the posts in the test sections are shown in the table. The Reynolds numbers were less than 2×10^{-3}.

4.1 Experiments

The protocols for the experiments are described in Chapter 3. The concentrations of the particles in water are low such that particles were observed as moving independent of each other. Collisions were rare and clusters or agglomerates were few or nonexistent. In the field of view, the particles were not attracted to and captured by the posts in detectable numbers as the tracers moved through the micro-model.

4.2 Results and Discussion

Representative trajectories of the particles of different sizes, at different flow rates for configuration II are shown in Figures 4.2 to 4.4. In Figures 4.1 stream lines for particle-free liquid are calculated and plotted on COMSOL for the same array of posts (Javadpour, 2012), with the differences that the domain is not bounded by parallel plates as for the micro-model and inertia terms in the Navier-Stokes equation are neglected. Similar plots were generated for the other two configurations and are presented in Appendix A and B. At low Reynolds numbers, the patterns of the streamlines for the fluid depend only on the array structure, but the value assigned to a particular line depends on the flow rates though the network. Some differences are

immediately obvious for the two contours. The particles (that are denser than the continuous phase) do not move in predictable manner. The path-line tracked by a particle, compared as it travelled between the grids or rows of posts, shows differences from one cycle to another. Typically, a particle travelling fast as it leaves a grid at the midpoint between two posts would slow down and graze the side of the post in the next grid, and from either side. Similarly, a particle that tracked close to a post in one grid ended up in the mid part of the adjacent grid downstream. Two particles, originally and apparently on the same path do not follow the same exact trajectories, even for the larger particles with reduced influence of thermal fluctuations. The pattern is not reversible and there is a distinct lack of symmetry of the path-lines on either side of the line (or more appropriately, plane) through the centers of the posts in each row of grids. Random, higher frequency, lateral displacements are also more noticeable as the particle size decreased, as would be consistent with Brownian motion superposed on the axial motion.

The above observations would appear to have consequences for using particles to reveal flow streams and path-lines in flow visualization studies at low stream velocities, in microfluidic devices and micro-models. Steam-lines and path-lines are not coincident. The trajectories in Figure 4.2 to 4.4 were obtained by joining consecutive images of individual particles that were recorded at 30 frames per second and an exposure of 25 ms per frame. At the highest of the three flow rates, the particles showed streaks, as illustrated if Fig 4.5 The length of the streaks divided by the exposure time yields an integrated value for the local velocity over the period. In digital images, the accuracy of determining the length of a streak is limited by the size of a pixel. Nonetheless, estimates of local, steady-state speeds and the direction of movement of particles are obtained and presented for three micro-model configurations, three particle sizes and the high flow rate of Table 3.2 in Figures 4.6, 4.7 and 4.8.

Figure 4.1 Fluid streamlines for micro-model configuration II, generated by COMSOL

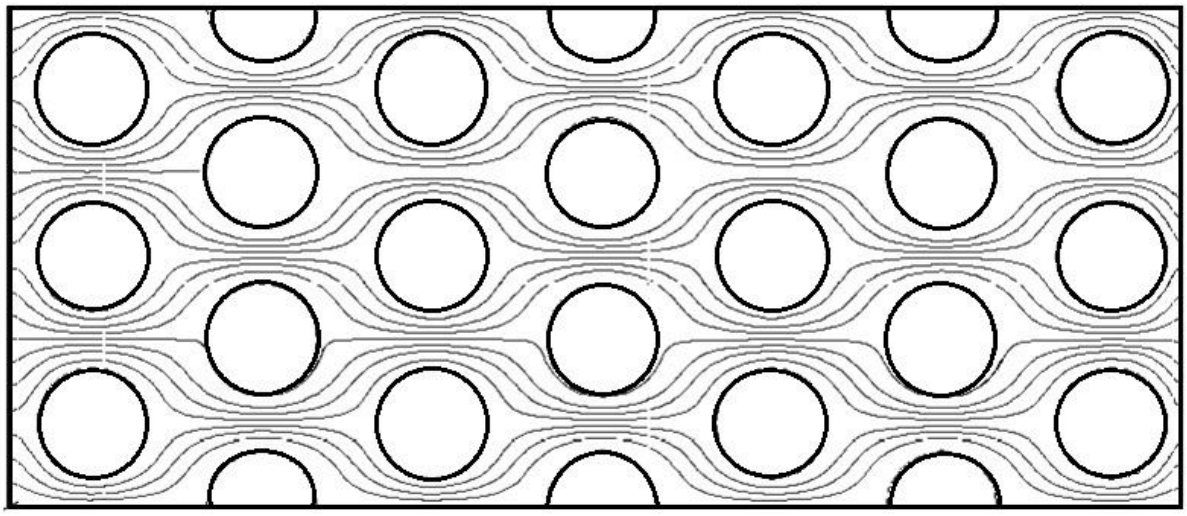

Figure 4.2 Samples of particle trajectory for 200 nm diameter spherical silica particles in micro-model configuration II at the (a) slow, (b) intermediate and (c) high suspension injection rate

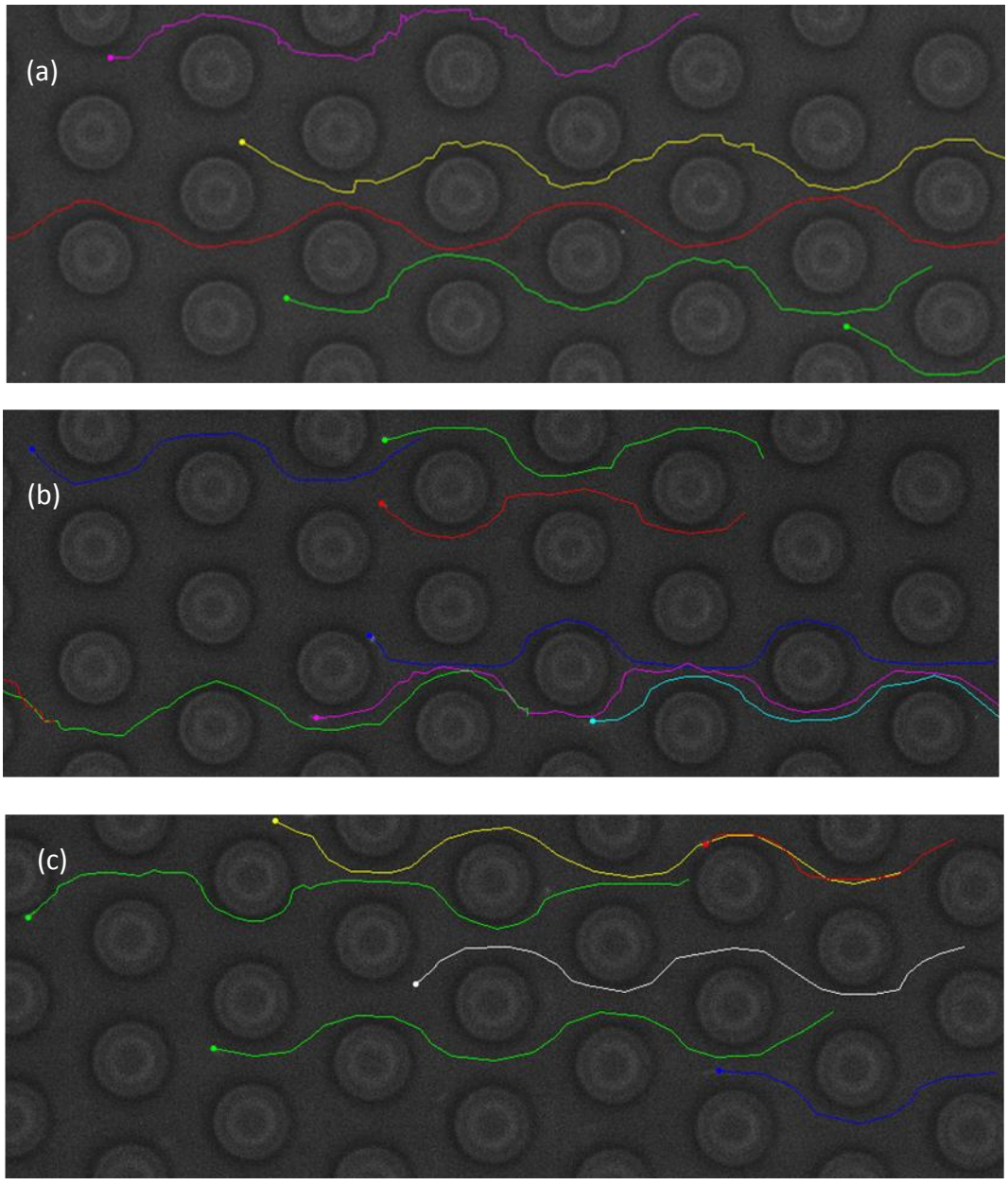

Figure 4.3 Samples of particle trajectory for 500 nm diameter spherical silica particles in micro-model configuration II at the (a) slow, (b) intermediate and (c) high suspension injection rates

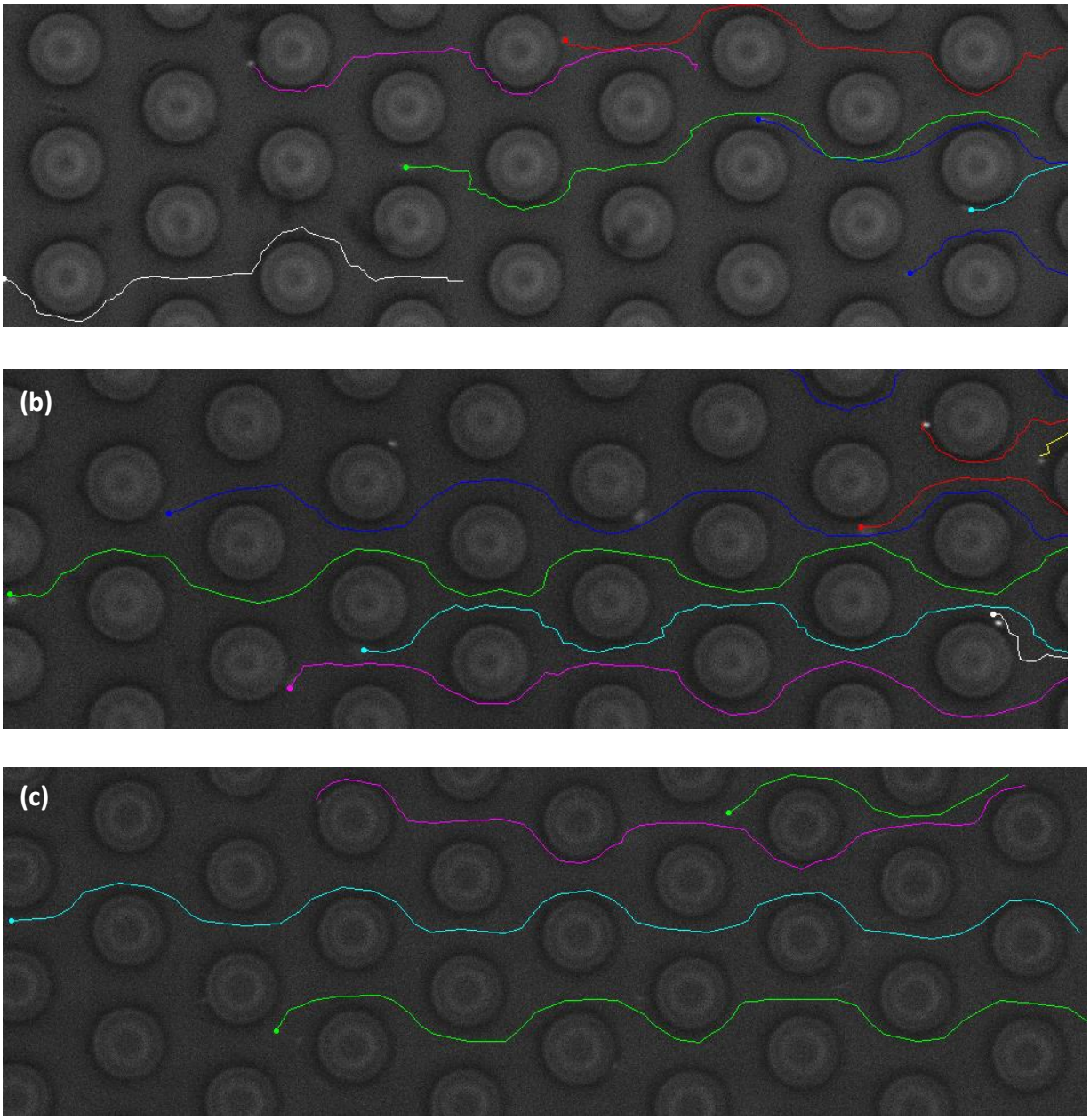

Figure 4.4 Samples of particle trajectory for 1500 nm diameter spherical silica particles in micro-model configuration II at the (a) slow, (b) intermediate and (c) high suspension injection rates

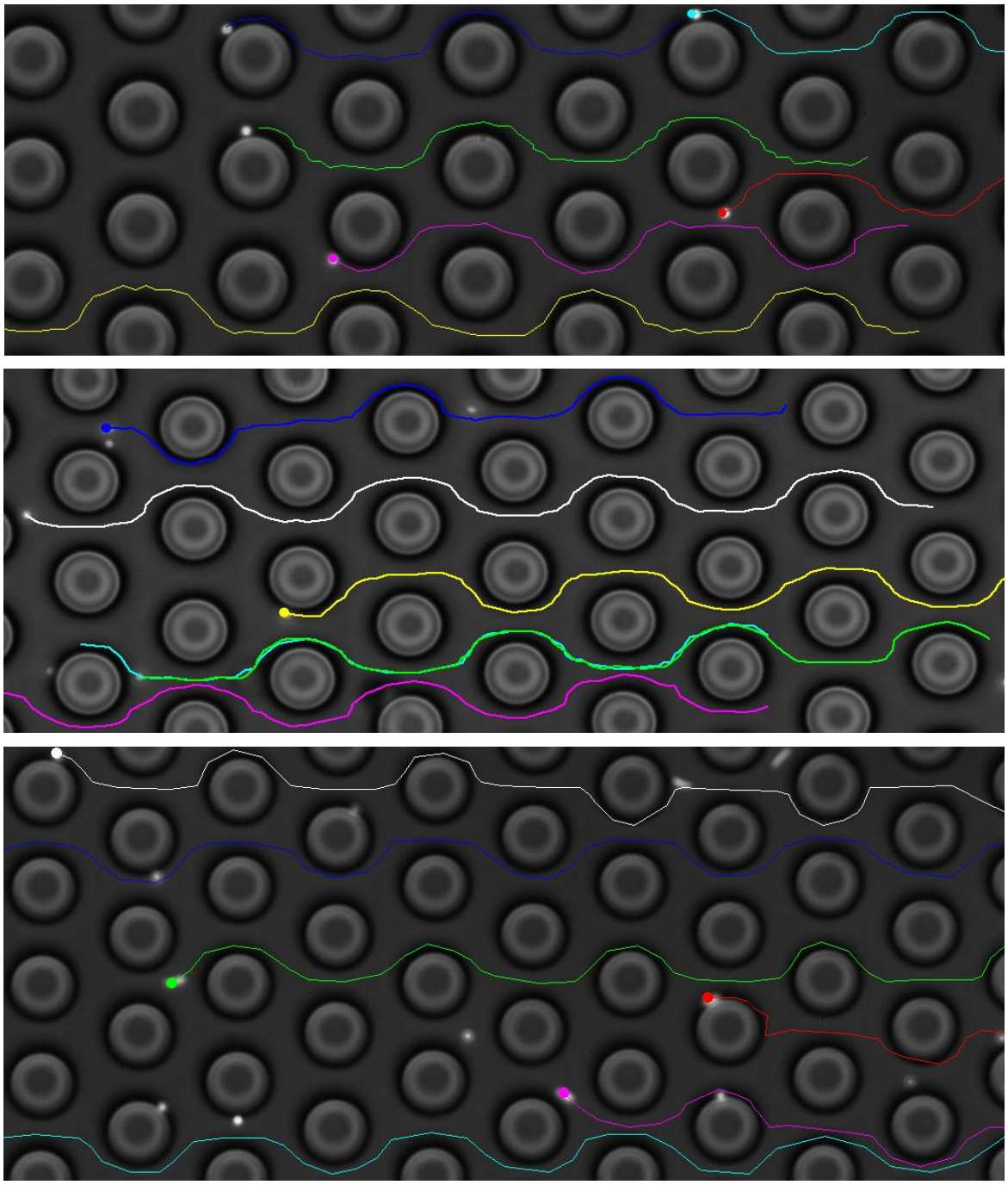

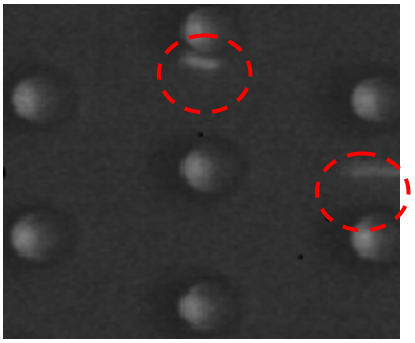

Figure 4.5 Example of particle streaks at high flow rates

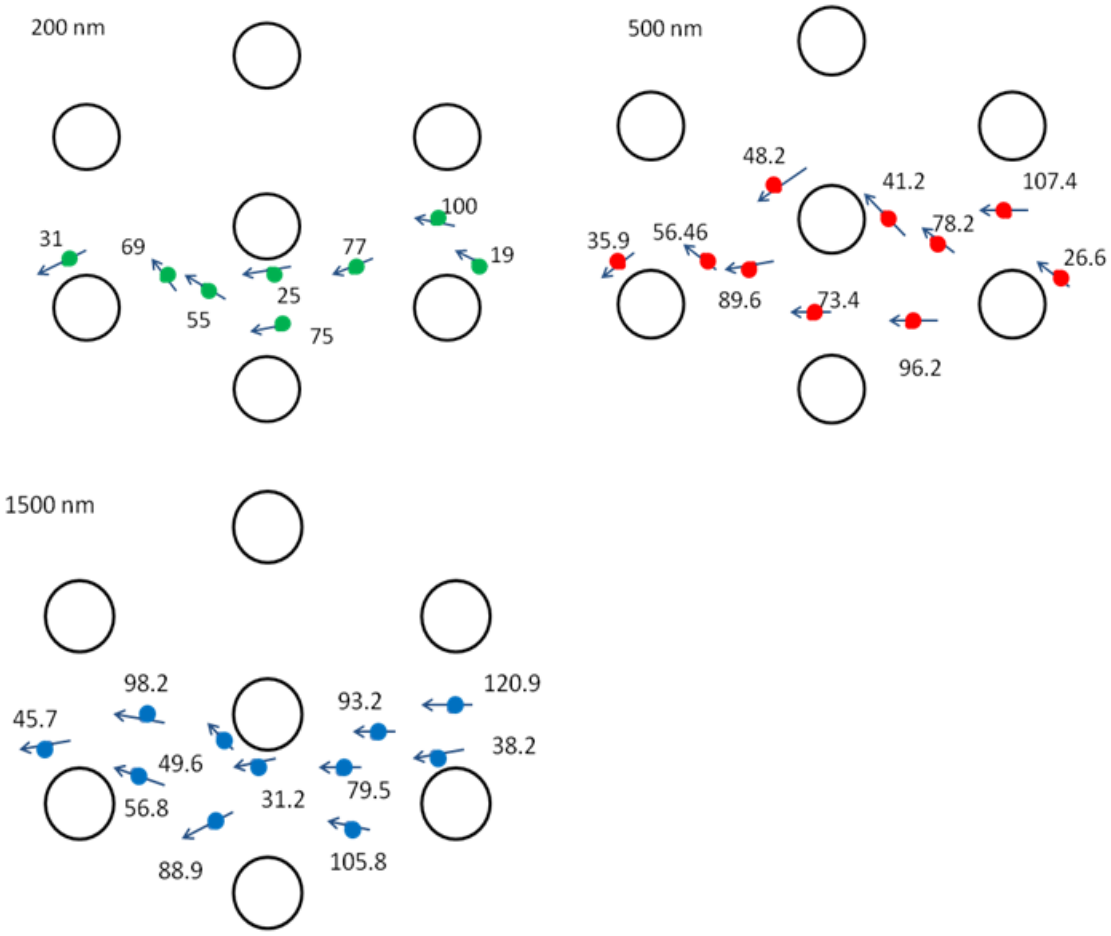

Figure 4.6 Velocity vector plots for configuration I , 200 nm particle, 500nm particle and 1500nm particle

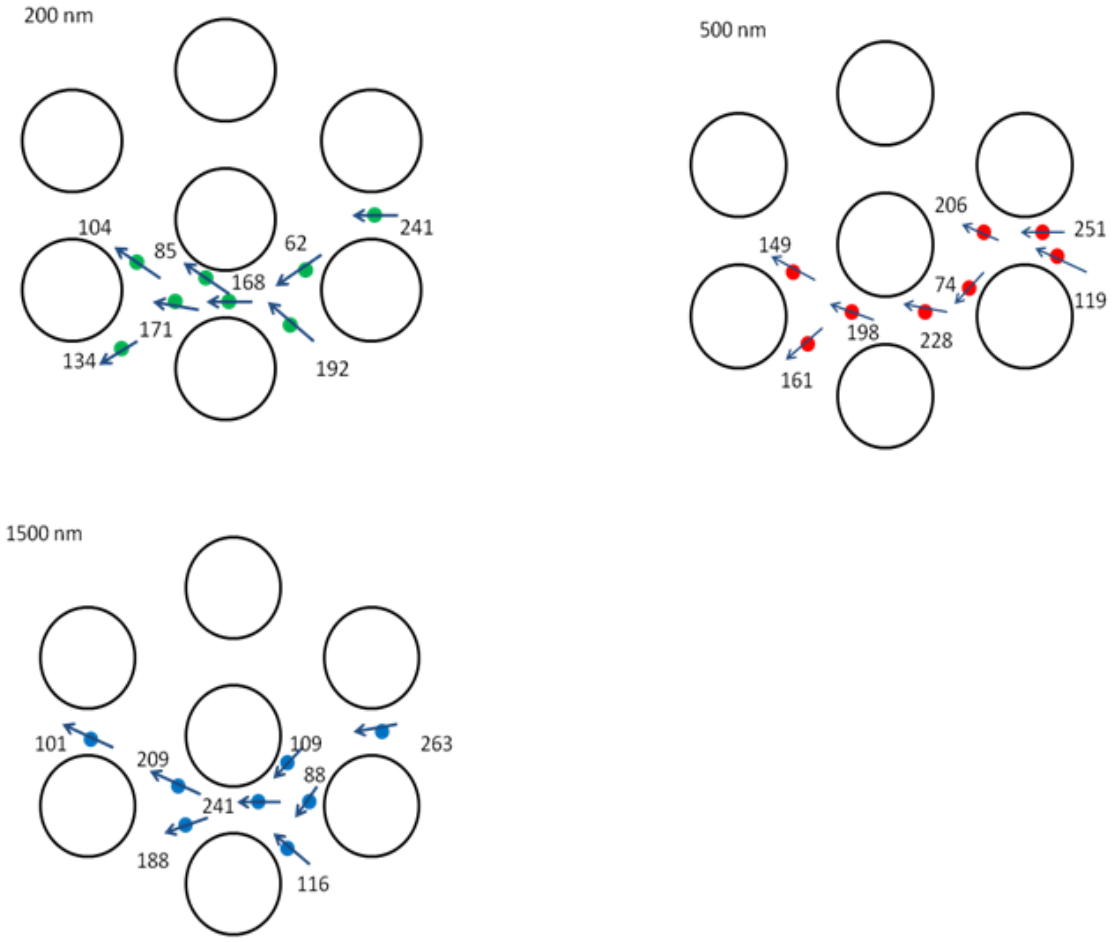

Figure 4.7 Velocity vector plots for configuration II , 200 nm particle, 500nm particlem and 1500nm particle

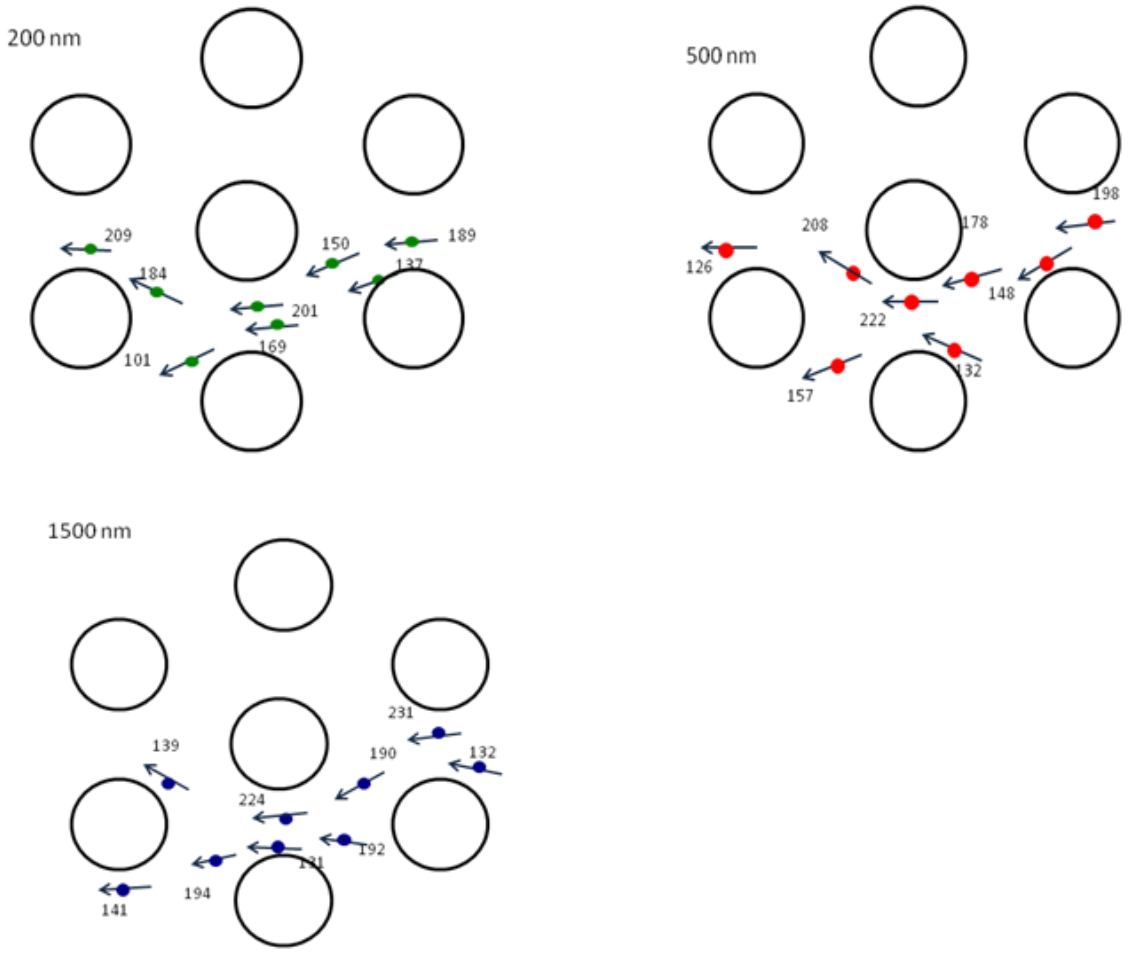

Figure 4.8 Velocity vector plots for configuration I , 200 nm particle, 500nm particlem and 1500nm particle

The data are presented in Tables 4.1- 4.3. The images were recorded for particles at or near the mid-plane between the parallel horizontal bounding surfaces of the micro-model structures. The depth-of-field about the mid-plane was ±5 μm in the gap that was 20 μm wide.

Some general trends are consistently noticed in the data in Figures 4.6, 4.7 and 4.8. Local velocities are highest near or at the mid-point between adjacent posts in each row oriented normal to the bulk flow. Such velocities decreased as the particle size are smaller. Particles accelerated towards the constriction presented by the posts, the pores, and decelerated rapidly once they emerged. Particles near the posts moved at velocities much slower than away from the wall. These results demonstrate that velocity profiles that vary with position are established within the micro-model configurations.

Table 4.1 Data for Micro-model Configuration I (Superficial velocity U_s = 54.7 μm/s, $u_{max|pore}$ = 176.7 μm/s, $u_{max|plates}$ = 82 μm/s, Reynolds number Re_{post} equals 4.7×10^{-4})

	$\overline{\lvert u \rvert}$, Particle speed μm/s	Particle direction **θ**, degrees	Minimum distance of particle center to post **d**, μm	Parameter κ = a/d
D_p = 1.5μm = 2a	120.9	178	3.46	0.21
$\kappa_{no\ slip}$ = 0.553	38.2	-165	0.66	1.14
κ_{min} = 0.214	93.2	169	4.45	0.17
β = 0.3 = a/R_o	79.5	-172	2.73	0.27
	105.8	175	4.79	0.15
	31.2	179	4.59	0.16
	89	-144	2.8	0.27
	49.7	148	1.07	0.7
	56.8	147	1.67	0.45
	98.2	164	4.69	0.16
	45.7	-159	1.82	0.41
D_p = 0.5μm	107.4	179	3.37	0.07
$\kappa_{no\ slip}$ = 0.383	26.6	150	0.54	0.46
κ_{min} = 0.0714	78.2	155	3.99	0.06
β = 0.1	41.3	155	1.03	0.24
	96.2	180	4.65	0.05
	73.4	175	2.55	0.1
	89.6	-176	4.54	0.06
	56.5	162	2.24	0.11
	35.9	-143	1.01	0.25
D_p = 0.2μm	100	177	3.37	0.03
$\kappa_{no\ slip}$ = 0.282	19	146.7	1.36	0.074
κ_{min} = 0.0286	77.6	-157	2.93	0.034
β = 0.04	25.7	-143	0.66	0.152
	75.7	177	2.68	0.037
	55	161	2.17	0.046
	69	144	4.01	0.025
	31	-168	0.8	0.125

Table 4.2 Data for Micro-Model Configuration II (Superficial velocity U_s = 54.7 μm/s, $u_{max|pore}$ = 309.2 μm/s, $u_{max|plates}$ = 82 μm/s, Reynolds number Re_{post} equals 1.64×10^{-3})

	$\|\overline{u}\|$, Particle speed μm/s	Particle direction **θ**, degrees	Minimum distance of particle center to post **d**, μm	Parameter κ = a/d
D_p = 1.5μm = 2a $\kappa_{no\ slip}$ = 0.439 κ_{min} = 0.3 $\beta = 0.15 = a/R_o$	263	176	2.14	0.35
	88	133	1.1	0.68
	116	146	2.03	0.37
	109	-142	1.5	0.5
	241	174	2.05	0.37
	209	159	1.88	0.4
	188	-160	1.66	0.45
	101	150	1.44	0.52
D_p = 0.5μm $\kappa_{no\ slip}$ = 0.304 κ_{min} = 0.1 β = 0.05	251	-178	2.26	0.11
	206	156	3.12	0.08
	119	163	0.8	0.31
	74	-147	1.12	0.22
	228	176	2.25	0.11
	198	159	2.08	0.12
	149	163	2.24	0.11
	161	-150	2.86	0.09
D_p = 0.2μm $\kappa_{no\ slip}$ = 0.224 κ_{min} = 0.04 β = 0.02	241	174	2.36	0.04
	62	-138	1.08	0.09
	192	150	2.18	0.05
	168	180	0.71	0.14
	85	156	1.13	0.09
	171	178	3.44	0.03
	134	146	1.86	0.05
	104	157	1.42	0.07

Table 4.3 Data for Micro-Model Configuration III (Superficial velocity U_s = 54.7 μm/s, $u_{max|pore}$ = 231.9 μm/s, $u_{max|plates}$ = 82 μm/s Reynolds number Re_{post} equals 1.23×10^{-3})

	$\|\overline{u}\|$, Particle speed μm/s	Particle direction **θ**, degrees	Minimum distance of particle center to post **d**, μm	Parameter κ = a/d
D_p = 1.5μm = 2a $\kappa_{no\ slip}$ = 0.439 κ_{min} = 0.1875 β = 0.15 = a/R_o	231	-177	3.12	0.24
	132	166	1.47	0.51
	190	-155	3.26	0.23
	192	168	4.68	0.16
	224	-177	3.9	0.19
	131	176	1.4	0.54
	194	-166	4.69	0.16
	139	146	1.56	0.48
	141	180	1.72	0.44
D_p = 0.5μm $\kappa_{no\ slip}$ = 0.304 κ_{min} = 0.0625 β = 0.05	198	-175	2.81	0.09
	148	-154	1.36	0.18
	178	-167	2.06	0.12
	132	155	2.1	0.12
	222	180	3.59	0.07
	208	149	2.98	0.08
	157	-160	2.12	0.12
	126	-178	1.25	0.2
D_p = 0.2μm $\kappa_{no\ slip}$ = 0.224 κ_{min} = 0.025 β = 0.02	189	-172	2.5	0.04
	137	-154	1.54	0.06
	150	-158	4.13	0.02
	201	-178	2.34	0.04
	169	-171	3.5	0.03
	101	-151	1.61	0.06
	184	144	4.19	0.02
	209	180	3.49	0.03

The mid-plane between the flat surfaces (the location at which images are recorded) is also the plane of symmetry for the velocity field. At this location, contours of streamlines for particle-free flow of the continuous medium will be identical to those for arrays of parallel posts of the same configuration at low Reynolds numbers. As earlier noted, in calculating the streamlines, the inertia term of the Navier-Stokes equations were neglected. Thus the patterns are symmetric in successive cycles about planes through the axes of posts in each row and indicate that the flows are reversible. The trajectories in Figures 4.2 to 4.4 have already shown that the particle pathlines are not coincident with the calculated streamlines and are distinctly asymmetric. The local particle velocities, magnitudes and directions, are also different from the fluid's. These features are explored further in the following.

4.2.1 Profiles in the fluid; the kinematics

The flow within each micro-model configuration is complex. Limiting or bounding solutions are considered at two locations. For low Reynolds number flows, velocity profiles develop quickly when a fluid enters a channel. The two extreme profiles under conditions of reversibility and full development, would be between two adjacent posts (the pore), and at the mid-plane between two consecutive rows or grids. At the plane through the axes of adjacent posts, the flow approximates that through a rectangular duct of the same projection – 5, 7 or 8 μm wide (depending on the configuration) and 20 μm tall. The fully developed velocity profile in a rectangular duct, for a viscous fluid, is (Dryden et al, 1932; Hartnett and Kostic, 1989)

$$u(y,z) = \varphi \sum_{i=1}^{\alpha} \left[\frac{(-1)^{i-1}}{(2i-1)^3}\right] . \left\{1 - \frac{\cosh(2i-1)(\frac{\pi y}{2a})}{\cosh(2i-1)(\frac{\pi b}{2a})}\right\} . \cos\frac{(2i-1)\pi z}{2a} \qquad (4.1)$$

$$\varphi = \frac{16a^2}{\pi^3}\frac{1}{\mu}\left(-\frac{dp}{dx}\right) \tag{4.2}$$

Figure 4.9 Rectangular duct cross section

An approximate profile that is more convenient is (Purday, 1949)

$$\overline{u} = \frac{u_{max}}{ab}\int_0^b \int_0^b \left[1-\left(\frac{y}{b}\right)^r\right]\left[1-\left(\frac{z}{a}\right)^s\right] dydz \tag{4.3}$$

where the exponent *r* (for profile across the narrow side) equals 2 to yield a parabolic profile, and the exponent *s* depends on the aspect ratio α (narrow side : long side) by the relationships:

$s = 1.54/\alpha$ for $0 < \alpha \leq 0.67$; and $s = 2.3$ for $0.67 < \alpha \leq 1$.

For the cross-section that is 7 x 20 μm, as in configuration 1 of the micro-models, $s \approx 4.4$. The resulting velocity profiles are similar to those shown in Figure 2 of the study reported by Qu and Mudawar (2002) through solving the equation of motion numerically. In the figure, reproduced

in Figure 4.9 below, the velocity is maximum at the geometric center of the cross-section. The average velocity is determined by integrating over the section:

$$\frac{u(y,z)}{u_{max}} = \left[1 - \left(\frac{y}{b}\right)^r\right]\left[1 - \left(\frac{z}{a}\right)^s\right] \quad (4.4)$$

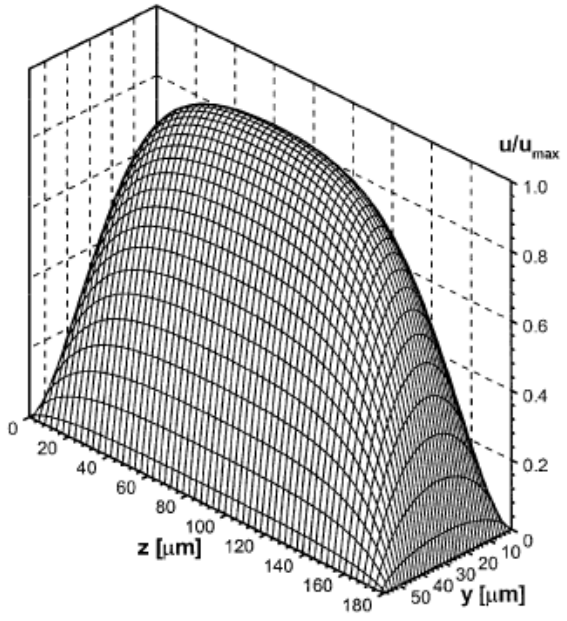

Figure 4.10 Numerical analysis results for the velocity profile in a rectangular channel (Qu and Mudawar , 2002)

From the profile suggested by Natarajan and Lakshmanan (1972), values of r and s in equation 4 were set at 2.006 and 3.874 respectively to obtain the relationship

$\frac{u_{max}}{u} = [\frac{(r+1)}{r}][\frac{(s+1)}{s}] = 1.885$ for the rectangular cross-section 7 x 20 µm being used for illustration.

At the highest flow rate, the superficial velocity into the micro-model is 54.68 µm/s, the average pore velocity U is calculated to be 93.7 µm/s, and the maximum velocity is estimated at 176.7 µm/s from the foregoing relationship. A comparison with the maximum particle velocities, at the same locations in Figure 4.6 (a, b and c), show that the fluid is faster and thus would be dragging the particles forward towards and at the constriction. The largest of the particle sizes (1.5 µm diameter) has the highest local velocity between two posts at 120.9 µm/s. The velocities for the 0.5 and 0.2 µm particles were 107.4 and 100 µm/s respectively at similar locations.

Since a fully developed profile was assumed to estimate the maximum velocity between posts, it is essential to justify that such profiles are attainable. The entrance length into a rectangular duct may be estimated from the analysis reproduced by Hartnett and Kostic (1989) in Figure 11. For the micro-model configuration 1, the aspect ratio α equals 0.35 and the dimensionless entrance length $L^{+}_{hy} \approx 0.08$.

$$L^{+}_{hy} = \frac{L_{hy}}{D_h Re^{+}} \quad (4.6)$$

$$Re^{+} = \frac{\rho u D_h}{\mu} \quad (4.7)$$

$$D_h = \frac{2ab}{(a+b)} \quad (4.8)$$

where a and b are the sides of the rectangular cross-section, D_h is the hydraulic diameter, Re^{+} is the Reynolds number and L_{hy} is the length or distance for flow development. On substituting values, D_h equals 10.37 µm and Re^{+} equals 9.72×10^{-4} at the highest flow rate. L_{hy} has a value of

8.34×10^{-4} μm. That is, velocity profiles develop over very short distances and the assumption of a fully developed profile in the "pore" is justified.

Downstream of a row of posts or grid, the fluid pattern adjusts. The fluid in the wake of posts accelerates while that emerging from the pores slows down while spreading laterally. Particle motions in Figures 4.6 to 4.8 do reflect directional and speed changes. If the fluid flow is reversible and velocity profiles change rapidly, flow through the mid-plane between two rows can be approximated, in the limit, as fully developed between two flat plates. The velocity profile would be parabolic and given by

$$u = u_{max}\left(1 - \frac{y^2}{a^2}\right) \tag{4.9}$$

where a is the half width of the gap separating the plates.

The velocity is maximum at y = 0 or along the mid-plane of the two bounding surfaces, and the value is 1.5 times the average velocity. Thus for configuration 1, the maximum fluid velocity would be 1.5×54.68 or 82 μm/s. An inspection of Figure 4.6, although not conclusive, would suggest that the particles are moving faster than the fluid at this location and are therefore experiencing deceleration due to hydrodynamic forces in the first half of the space between consecutive rows of posts.

The foregoing are bounding limits for actual velocity profiles that have been calculated for viscous flow through arrays of parallel cylinders (Happel, 1959; Kuwabara, 1959; Kirsch and Fuchs, 1967; Gordon, 1978; Sangani and Acrivos, 1982; Drummond and Tahir, 1984; Ingham et al, 1991; Brown, 1993; Wang, 2003; Hellou and Yazidi, 2004).

The distance separating the rows of an array are quite important as to whether the limit of fully developed flow between parallel plates is a reasonable approximation at the plane of symmetry when inertia is neglected, that is, for Stoke's flow.

The closest experimental work to this study, in terms of tracking trajectories of particles passing through arrays of cylinders, is that reported by Kirsch and Fuchs (1967). The primary difference is that the current study involves much smaller spatial and time scales. The Reynolds numbers (with reference to the post diameter) was one to two orders of magnitude higher (at 0.01 – 0.05) compared to the values for the current study. Moreover, the 20—30 μm diameter spherical granules of polymethylmethacrylate coated with gold were neutrally buoyant in the 95% glycerol liquid used. The particles are also much smaller than the post diameters (7 and 14 mm) and the spacing between the posts in equilateral triangular arrays. The volume fractions occupied by the posts were 0.05 and 0.2. This means that post wall to post wall at the narrowest parts of a row were 22.8 mm wide for the 7 mm diameter posts and 15.8 mm wide for the 14 mm diameter cylinders. The tracking particles (diameter/pore width < 1/500) are too small to alter the bulk flow patterns. These are in contrast to the conditions for the present study for which the particle diameter: pore width is in the range 1/16 to 1/3. The pathlines for the particles in Kirsch and Fuchs' Figure 3 indicate that the streamlines around the cylinders have substantially recovered to the upstream patterns at about ½ to 1 particle diameter downstream. In effect, for post separation of the order of one post diameter, the streamlines are like for flow around isolated cylinders at the low Reynolds numbers for the study.

Other recent experimental studies that involved tracking of particles in micro-models are those of Auset and Keller (2004), Lazouskaya, et al., (2006) and Baumann et al.(2010) . Auset and Keller were interested in pore-scale effects of particle and pore sizes on colloidal dispersion in micro-

models. The micro-models were quadrilateral arrays of rounded rectangular posts with straight, intersecting channels of constant 10 and 20 μm width separating the posts in two configurations, and a third configuration with both 10 and 20 μm channel width and paths that are not straight. The height of the channels was 12 μm. The colloidal particles were 2, 3, 5 and 7 μm diameter, large enough to modify local flow patterns in the channels but not exhibit significant Brownian motion. The particles were also about 5% denser than water, the medium of suspension. The authors concluded that larger colloid particles were less dispersed than smaller ones because larger particles travelled in the center streamlines, at higher velocities, and with less detours. This appears to be a conjecture as neither the positions nor the instantaneous velocities of particles were reported. For micro-model configuration 3 that they called the "zigzag network", particles are shown to have migrated from one side of a channel to the opposite side. This would require that streamlines are crossed. Image resolution was probably not high enough to ascertain these values, if they were of interest. Particles that detoured into side channels appear to be moving, at upstream locations, close to a wall adjacent to the side streams into which they are diverted irrespective of pore size. There is also the presumption that the particles would track streamlines without deviations, contrary to what has been observed in the current work.

Lazouskaya et al. (2006) were interested in the transport and retention of colloidal particles at air-water interfaces of partially saturated porous media. They used a straight channel with a square cross-section, 500 μm a side, and open to air at the top. The particles tracked were 1.1 μm diameter latex microspheres with a density of 1055 kg/m^3. The particles are much smaller than the channel dimensions and they seem to follow the stream lines in the bulk flow, at least along the mid-plane in the longitudinal direction. Another interesting observation reported was that the air-water interface was semi-rigid as the no-slip condition at solid walls was nearly satisfied. The

interface itself moved along the flow direction in the middle of the channel, and backwards near the walls.

Baumann et al.'s study is similar to Auset and Keller's. The primary differences were that the micromodel arrays only regular and ellipsoidal for a configuration, (the other two were heterogeneous and irregular), 0.5 and 1 μm diameter polystyrene microspheres were used for tracing and the pore throats were between 30 and 60 μm wide, the channel depth was 50 μm and the porosities were 0.26 to 0.36. Pictures of the particles were taken at 10 frames per second and the results analyzed were the path lengths traversed.

4.2.2. Forces on isolated spherical particles in a viscous fluid; the dynamics

Shown in Table 3.2 are conditions for the experiments, the volume flow rates and velocities calculated upstream of the micromodels (the superficial velocities), the pore velocities through the rows of posts normal to the flow direction and the corresponding Reynolds numbers for the three configurations. Figures 4.6, 4.7 and 4.8 as earlier presented, show instantaneous velocities (values and direction) at points within the micro-models. Local particle velocities in the pore throat, particularly near the center, significantly exceed the calculated average fluid pore velocities in Table 3.2. It has also been shown earlier that the local velocities of the particles and the suspending media are not equal both upstream and downstream of pores. The forces that may act on the particles are reviewed in the following as the basis for explaining the results.

The forces that act on particles in fluids in motion have been extensively studied since Stokes' analysis in 1851 (Boussineesq, 1885; Basset, 1888; Oseen, 1927). Excellent reviews have been done by Odar and Hamilton (1964), Happel and Brenner (1965), Leal (1980)and Crowe, Sommerfield and Tsuji (1998) amongst others. When the suspending fluid can be considered to

be a continuum, i.e. dense, and thermal fluctuations or Brownian motion can be ignored, isolated particles can be under the influence of several forces depending on the environment.

In a uniform, steady flow, the force on a particle may be expressed as

$$F_D = \frac{1}{2}\,\rho_f\, C_D A|\vec{u} - \vec{v}|\,(\vec{u} - \vec{v}) \qquad (4.10)$$

Where ρ_f is the fluid density, C_D is the drag coefficient, A is the projected area and $\vec{u}$ and $\vec{v}$ are respectively the velocity vectors for the continuous phase and the particle. At low Reynolds numbers, defined with the characteristic velocity as $|\vec{u} - \vec{v}|$the coefficient of drag is estimated from

$$C_D \approx \frac{24}{Re} \qquad (4.11)$$

Where $Re = \frac{D_p|\vec{u} - \vec{v}|\,\rho}{\mu}$, D_p is particle diameter and ρ and μ are the fluid density and dynamic viscosity respectively. The force is

$$F_D = 3\pi\mu D_P|\vec{u} - \vec{v}| \qquad (4.12)$$

By Stoke's law, valid to Re < ~ 2 (on the basis of empirical data). The particle moves through the fluid by deforming it and viscous shear at its surface is more significant than inertia. The motion of the particle affects the fluid at considerable distances from the body. For walls located at around 20 to 30 diameters or less away from a particle, Stoke's law requires a correction. (Happel and Brenner, 1973; Bungay and Brenner, 1973; Ganatos et al., 1980; Dagans et al., 1982; Falade and Brenner, 1988; Pozkiridis, 1994) For the system of current interest, the proximity of the particle to bounding surfaces within the micromodels indicate that the stationary walls would significantly affect the motion of the particles, unlike the system for Kirsch and

Fuchs (1967) but similar to Auset and Keller's (2004). The analysis of Falade and Brenner (1988) on the effects of wall curvature on Stokes resistance on a proximate particle is particularly relevant to the current work, when the particle is located at the mid-plane between the flat bounding walls and is close to the posts as it travels through the pore or space between adjacent posts in each row or grid. For particles next to a cylinder, and satisfying the conditions that κ (radius of spherical particle, a / shortest perpendicular distance from the wall, d) is between 0 and 1 and β (radius of spherical particle, a / principal or characteristic radius of curvature of the wall, $D_p/2$) << 1 as is the case for the current experiments, the particle would be moving faster than the fluid near the wall (κ of O(1)) and slower than the fluid in which it is suspended when $\kappa < (9\beta/16)^{1/3}$, that is further away from the nearest post. Local particle velocity vectors in Figures 4.6 to 4.8 have been earlier shown, at least at the center of the pores (where, for example, κ = 0.0286, 0.0714 and 0.214 for the 0.2, 0.5 and 1.5 μm diameter particles respectively for micromodel configuration I), to be moving slower than the suspending medium. Another condition is that β/κ <<1. For the current experiments, however, velocity vectors are provided also for β/κ up to O (1).

The flow field within the micromodels is also not uniform at the pore and elsewhere. In a non-uniform field, the Faxen (Faxen, 1922) force (Happel and Brenner, 1965) contributes to particle drag. That is,

$$F_D = 3\pi\mu D_P(\vec{u} - \vec{v}) + \frac{\pi}{8}\mu D_P^3 \nabla^2\vec{u} \qquad (4.13)$$

where the Laplacian of the velocity vector for the continuous phase, $V^2\vec{u}$, is evaluated at the position of the particle.

In an unsteady flow field, the particle is accelerated and decelerated along its path in response to the suspending medium flowing in and out of pores, and changing directions between rows of cylinders in the micromodels. Forces that accompany changes in velocity are added (or virtual) mass effects and the Basset force (Odar and Hamilton, 1964; Happel and Brenner, 1965; Schöneborn, 1975; Maxey and Riley, 1983; Mei et al., 1991; Voir and Michaelides, 1991; Michaelides and Feng, 1996; Michaelides and Roig, 2011). The "added mass" effect is associated with the force required to change the velocity of the fluid in the neighborhood of the particle. The "Basset force" is related to the delay in developing the viscous boundary layer around the particle in response to changes in its relative velocity with the medium.

The "added mass" is estimated from the form drag a particle develops to change the kinetic energy of the fluid through which it is passing, assuming potential flow (Crowe at al.; 1998). The relationship is

$$F_{ave} = \frac{M_f}{2}\left(\frac{D\vec{u}}{Dt} - \frac{d\vec{v}}{dt}\right) = \frac{\pi}{12}\rho D_P^3\left(\frac{D\vec{u}}{Dt} - \frac{d\vec{v}}{dt}\right) \qquad (4.14)$$

where ρ_f is the fluid density.

For particles moving in an oscillating fluid, Odar and Hamilton (1964) and Schöneborn (1975) have shown that M_f should be corrected.

For an impulsive displacement of a sphere from a stationary position in a viscous fluid, the Basset force is given by (Crowe et al., 1998)

$$F_B = \frac{3}{2}\, D_P^2 \sqrt{(\pi\mu\rho)} \left[\int_0^t \frac{\frac{D\vec{u}}{Dt} - \frac{d\vec{v}}{dt}}{\sqrt{t-t'}}\, dt' \right] \qquad (4.15)$$

For a moving sphere subjected to an impulse, the expression developed by Reeks and McKee (1984) is

$$F_B = \frac{3}{2}\, D_P^2 \sqrt{(\pi\mu\rho)} \left[\int_0^t \frac{\frac{D\vec{u}}{Dt} - \frac{d\vec{v}}{dt}}{\sqrt{t-t'}}\, dt' \right] \qquad (4.16)$$

On combining the terms, the equation of motion for an isolated particle, neglecting the effects of nearby walls and Brownian motion, was presented by Maxey and Riley (1983) as for horizontal flow.

$$m\frac{d\vec{v}}{dt} = 3\pi\mu D_p(\vec{u} - \vec{v}) + \frac{\pi}{8}\mu\, D_p^3 \nabla^2\vec{u} + \frac{\pi}{6}\, D_p^3(-\nabla P + \nabla\pi) + \frac{\pi}{12}\, D_p^3\rho_f \left(\frac{D\vec{u}}{Dt} - \frac{d\vec{v}}{dt} - \frac{D_p^2}{40}\, \frac{d\,(\nabla^2\vec{u})}{dt} \right) +$$

$$\frac{3}{2}\, D_p^2(\pi\rho\mu)^{0.5} \cdot \left[\int_0^t \frac{\frac{D\vec{u}}{Dt} - \frac{d\vec{v}}{dt}}{\sqrt{t-t'}}\, dt' + \frac{(\vec{u}-\vec{v})_0}{\sqrt{t}} \right] \qquad (4.17)$$

The wall effect on particle motion, at least the influence of the walls of the posts at the mid-plane of the micro-models and at the pore throat, has been earlier examined. In Figs 4.6 through 4.8, particles close to the posts appear to be moving faster than estimates of the velocity of the suspending medium without particles at the same locations. Particles further away from the posts moved slower than the fluid on approach to and at the pores. Particles emerging from the pores, however, did not lose speed at the same rate as the fluid and appear carried forward by inertia and added mass. Evaluation of the individual contributions of the components of equation 17 is not feasible because of lack of data or theoretical values for the fluid velocity field v_2 as altered by the presence of the particles.

4.2.3. Displacements of Nano-particles in a flowing fluid

Nano-particles experience all the same forces as for particles greater than about 2 μm diameters but they are also subject to thermally fluctuations, and thus random displacements known as Brownian motion (Chandrasekhar, 1943; Probstein, 1998; Mazo, 2002) in the suspending medium.

Traces of the trajectories of particles in the micro-model configurations presented in Figs 4.2 to 4.4 are representative of recorded tracks chosen at random. For each configuration, the traces are for different particle sizes and flow rates of the suspension. Features common can be seen with reference to one of the configurations, e.g. the 5-7-9 micro-model. The details are at three levels. First, at the pore scale level, the tracks of a particle between alternate rows or grids (a cycle) vary from one cycle to the next, i.e. flow is periodic but not repeating . This is amply demonstrated in Fig 4.3 (a, b and c) for which two tracks of 500 nm diameter particles nearly overlay for one or more cycles either to diverge downstream or be seen to have originated from different positions. Second, particles tend to undergo lateral displacements as they move downstream. This is reflected in tracks changing directions (anticlockwise to clockwise, and vice versa) around posts from cycle to cycle. Lateral drifts away from the direction of net fluid flow are more obvious at slow suspension injection rates. The third detail is at a much smaller scale than pore dimensions. Irregular and short-range displacements are noted along the paths of the particles as may be ascribed to Brownian motion. The degree of resolution of the fluctuations (Chandrasekhar, 1949) is determined by the rate of image capture and magnification, in this case, 30 frames per second and a magnification of 40.The extent of deviations from a harmonic pattern is suppressed as the particle size increased and flow rates are increased.

Three issues are to be explored on the basis of the data; tortuosity of the particle paths, space-averaged axial velocities and longitudinal dispersion. Each of these involve considering collective data for several particles. The tortuosity λ is the total actual distance a particle travels (along a smooth path) divided by the linear distance between the start and terminal locations. It has an effect on the rate of diffusion through the media (Fetter , 1993). The results for over 50 particles at each flow condition and particle size for micro-model configuration I (5-7-9) are shown in Table 4.4. For this configuration, a maximum value for λ of around 1.62 – 1.65 is estimated for a particle travelling furthest from all posts. Measured values in Table 4 are lower and they show trends.

Table 4.4 Tortuosity in micro-model configuration I (5-7-9) (the scatter for this data is about 3%)

Superficial velocity in micro-model, μm/s	Particle diameter 200 nm	Particle diameter 500 nm	Particle diameter 1500 nm
6.13	1.40	1.21	1.14
14.88	1.34	1.15	1.10
54.68	1.29	1.11	1.05

The results suggest that the paths for the larger particles were more "straight" and track variations less. The configuration with the highest porosity (lowest solid density) also has the potential for allowing particles to travel longer distances. The maximum λ for configuration II (10-5-7) with the lowest porosity, for example, is around 1.28.

The mean speeds at which particles percolate or pass through a porous medium is often of more interest than local values. Particles accelerate when entering pores, reach peak velocities there

and slow down at the exit due to hydrodynamic forces. The average speed is the integrated value over at least a geometric cycle of the micro-model. For the data reported in Table 4.5 below, any two points separated by four cycles were considered. Both the linear distances $\mathbf{L_s}$ and actual tracks $\mathbf{L_a}$ covered by particles were determined and divided by the time that elapsed for each particle to cover the distances. For each micro-model configuration, the average speeds for 35 to 45 particles were determined for each of the particle diameter and suspension flow rates.

Table 4.5 Mean particle speeds through micro-models and Dispersion Coefficients

Configuration	Pore velocity, µm/s	D_p = 200 nm	D_p =500 nm	D_p =1500 nm
		VLs, µm/s - VLa, µm/s - KL(10^12), m2/s		
I	10.50 ± 0.02	8.87 ± 0.72 14.01 ± 0.91 42.69	9.22 ± 0.52 13.04 ± 0.88 31.4	10.10 ± 0.91 12.07 ± 0.83 18.54
	25.50 ± 0.05	14.77 ± 0.28 22.14 ± 1.67 56.66	16.37 ± 0.99 21.03 ± 1.69 45.69	17.59 ± 0.7 20.24 ± 1.9 26.75
	93.74 ± 0.20	54.28 ± 5.33 77.96 ± 4.56 121.76	58.64 ± 4.70 71.72 ± 7.19 105.41	63.33 ± 4.6 68.73 ± 3.9 63.11
II	18.38 ± 0.02	11.95 ± 1.27 16.70 ± 0.81 71.04	12.82 ± 1.04 15.53 ± 0.92 64.3	13.15 ± 0.96 14.97 ± 1.27 36.7
	44.63 ± 0.05	22.38 ± 1.97 30.08 ± 2.21 90.84	24.46 ± 2.13 28.37 ± 2.71 82.6	25.34 ± 2.25 27.78 ± 3.04 60.1
	164.04 ± 10.2	84.16 ± 6.51 109.15 ± 4.24 170.33	95.63 ± 6.73 106.54 ± 5.92 147.2	100.19 ± 5.69 104.85 ± 7.01 135.69
III	13.79 ± 0.02	9.42 ± 0.93 12.01 ± 0.7 66.85	10.12 ± 0.62 11.61 ± 0.79 36.25	10.57 ± 0.95 11.02 ± 0.87 21.58
	33.48 ± 0.05	23.37 ± 1.58 27.19 ± 1.42 83.65	24.30 ± 1.66 26.40 ± 1.29 55.58	24.82 ± 1.99 25.57 ± 2.68 48.76
	123.03 ± 0.20	93.48 ± 7.19 105.72 ± 5.59 149.58	97.22 ± 3.59 104.01 ± 6.28 135.69	100.43 ± 5.46 103.18 ± 4.19 119.69

The results in Table 4.5 for V_{Ls} confirm that larger particles would penetrate deeper, over a given interval, than smaller particles into a porous medium in the absence of steric hindrance. This is consistent with the data on tortuosity and that higher hydrodynamic forces propel the larger particles. The values of actual average speeds, V_{La}, for the smaller particles are higher than for the large particle because the smaller particles travel longer distances in the circuit, i.e. the tracks are longer. These results are consistent for the different configurations.

Translational dispersion coefficients were also calculated from the data and reported in Table 4.5. Dispersion (or spreading) of particles in the suspension will occur as a result of a combination of at least three effects; at any cross-section, the velocity of the fluid is non-uniform (Taylor dispersion), the channel is tortuous and particles travel at different average speeds along different paths that depend on where each initially happens to be located and particles experience lateral displacements due to lift induced by rotation or collisions (the chromatographic effect), and particles are subject to thermal fluctuations that change their directions of motion on short time scales (Brownian motion).

At the macroscopic scale, the micro-models are treated as 1-dimensional, homogeneous domains but they are not isotropic. For a net bulk flow of a suspension along direction x and a suspension with a solid population density C, the material balance equation at steady state is:

$$K_L \frac{\partial^2 C}{\partial x^2} - V_x \frac{\partial C}{\partial x} = 0 \qquad (4.18)$$

Where v_x is an average velocity derivable from Darcy's law, and KL is the coefficient of longitudinal dispersion. The coefficient is estimated from (Fetter, 1999; Auset and Keller, 2004)

$$K_L = \frac{\sigma_L^2}{2t} \qquad (4.19)$$

$$K_L = \frac{1}{N}\sum(L_{ai} - L_{a\,Avg})^2/2t_i \quad (4.20)$$

Where L_{ai} is the actual distance travelled by a particle from its initial position 4 cycles earlier (a cycle is the space between alternate rows of posts or grids, i.e. 10 consecutive pores), and $L_{a\,Av}$ are the average distances for N particles in a set, and t_i is the time elapsed for each particle. It is noted that values of L_a depend on the recorded particle paths and they would be larger at higher frame rates of the camera (and the path will be impossibly difficult to trace if fluctuations up to 10^{21}/s can be recorded (Chandrasekhar, 1943), but K_L is not expected to change substantially as a consequence of the randomness of fluid molecules – suspended particle collisions.

The result presented in Tables 4.5 show that dispersion increases with the flow rate of the suspension for all particles sizes, is larger for the smaller particles and increases with the solid density of the micromodel configuration.

The relative contributions of hydrodynamic factors (advection) and thermal fluctuations to dispersion can be explored by reference to a dimensionless quantity, the Peclet number, ul/D_i where u is a characteristic fluid velocity, l is a length scale and D_i is the coefficient of diffusion. For this study, u is the average pore velocity, l is the diameter of the post (corresponding to grain size in a particulate bed) and D_i is the diffusion coefficient for particles in suspension. The present case corresponds to the situation for dilute suspensions in which particles denser than the fluid do not interact (Einstein, 1956; Chandrasekhar, 1943; Lebowitz and Rubin, 1963). The translational diffusion coefficient for a sphere is given by the Stokes-Einstein equation (Einstein, 1956)

$$D_i = \frac{kT}{6\pi\mu a} \quad (4.21)$$

Where k is the Boltzman constant, T is absolute temperature, μ id the dynamic viscosity of the fluid and a is the radius of the sphere. At 20°C, estimates for D_i (10^{12}) are 2.15, 0.86 and 0.286 m^2/s for the 200, 500 and 1500 nm diameter particles respectively.

Experimentally derived dispersion coefficient divided by the diffusion coefficients are plotted versus Peclet number for all the experimental conditions in Fig 19 As per previous studies, the data suggest that the dispersion of the suspended particles is controlled by advection rather than by diffusion for Pe > 10.

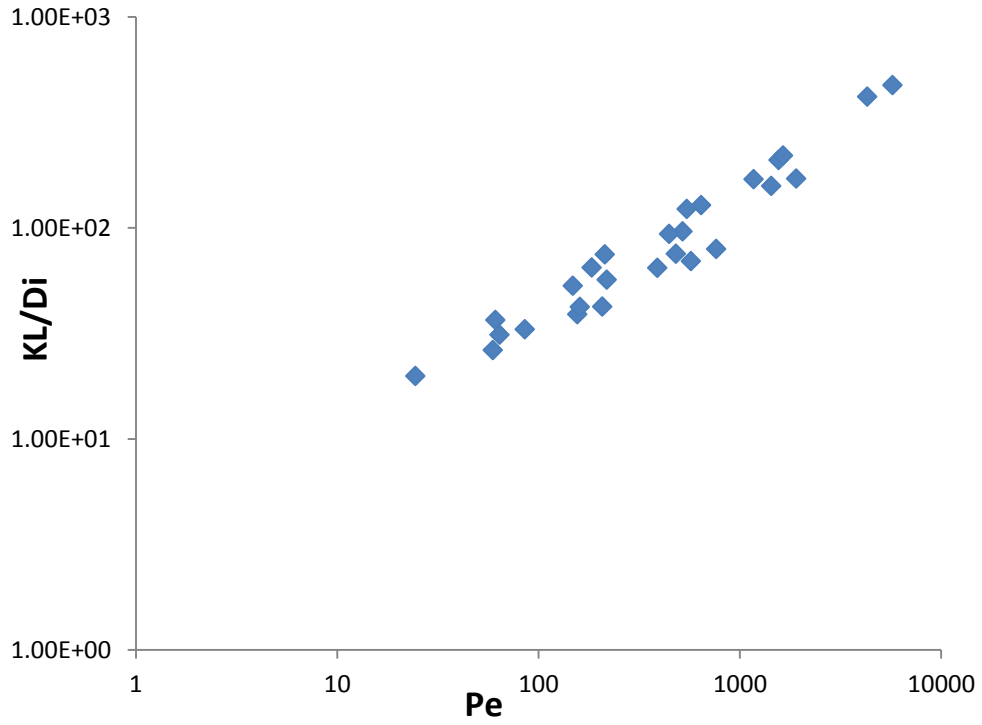

Figure 4.11 Particles Dimensionless Longitudinal Dispersion Coefficient (K_L/D_i) versus Pe number for all experimental data

Chapter 5

SHEAR-INDUCED DISPERSION OF COLLOIDAL PARTICLES

Transport and dispersion of suspensions of colloids and nanoparticles in fluids occurs in nature, in industrial processing and in the domestic environment. For example, the air humans breathe typically contains $10^4 – 5\times10^4$/ml ultra-fine particles of dusts, salts, micro-organisms and liquid droplets (Pentinnen et al., 2001). A fraction of these are trapped in the airways of the lung (an anisotropic porous medium) in each breathing cycle of inhalation and exhalation. Captured particle are expelled with mucus, or absorbed into the body to be retained or rejected by other means. Particles remaining in suspension are more rapidly mixed with air downstream than would be promoted by thermally-induced fluctuations, or diffusion. Blood, at a hematocrit of 40, is also a complex suspension that flows through human vascular and microvascular networks. Saline administered intravenously and pharmaceuticals injected into arteries mix with blood plasma while flow is occurring in the vessels. The flow, even when laminar, enhances the mixing. Other examples abound. The systems are characterized by the presence of gradients of particle population density in flowing streams.

Of interest is this study are how particle population density gradients evolve and are manifest in the transition zone of a colloidal suspension that is displacing or is being displaced by a suspension of the same materials but at a lower or zero solid content. In the system of current interest, the suspension flows between parallel plates (the Hele-Shaw section of the test cell) and then through simple-structure models of porous media.

The system studied here consists of dilute aqueous suspensions of spherical silica particles that are 200, 500 and 1,500 nm in diameter, constituting 0.018-17.5 volume % in water (as presented

in Table 5.1) displacing particle-free water slowly. At high concentrations (more than 20%) the viscosity of the suspension will increase and might affect the results. The apparatus is diagrammatically shown in Fig.3.2 and configurations for the micro-models are presented in Table 3.1. As described in chapter 3 the micro-model is connected to a flow system and mounted on a microscope equipped with a digital camera (figure 3.1). Dilute suspensions of coated silica particles encasing a fluorescent dye are prepared and pulled by suction into the test cell.

On entering the proximal end of the cell from which water was being withdrawn, the suspension quickly spreads laterally and advanced through a distance of 10 mm to reach the first row of posts for the micro-model. This is the inlet or Hele-Shaw section with an aspect ratio (path length over gap width) of 500. At the highest superficial velocity (of 55 μm/s), when one uses the physical properties of water at room temperature, the flow can be shown to be essentially fully developed in about 2 μm distance from the inlet, on admission of the suspension into the test cell. Shorter distances are required at slower flow rates. The detailed protocols for the experiments are described in Chapter 3. The relationship between suspension concentrations and solid fraction is shown in Table 5.1. The solutions used in these experiments were made such that the particle population density at the inlet into the test cell for these diameters was kept at ~4.4×10^{10} per ml for the lower concentrations (level 1) and it was at ~$9.9\text{x}10^{10}$ per ml for the higher concentrations (level 2)

Table 5.1 Relationship between suspension concentrations and solid fraction

Particle diameter, nm	Concentration level	Solid fraction, φ_s (10^3)
200	1	0.184
	2	0.414
500	1	2.878
	2	6.474
1500	1	77.75
	2	174.81

5.1 Results

Instantaneous values of particle concentrations at two areas of the test cell were obtained from photographic records. The areas, as illustrated in Fig 5.1, are at the end of the Hele shaw section or the inlet into the micromodel section (1), and at the centre of the micro-model (2). Area 1 is 150 µm long and its width in the direction perpendicular to the flow is 85 µm. An image typical of those recorded in area 1 is presented in figure 3.5a. In order to reveal the gradients in particle population density, area 1 was divided into 5 equal zones (each a 30 µm strip) and the number of particles counted within each zone. The particle counts were for the entire flow cross-section and thereby represented the number of particles instantaneously present in a volume 30 µm × 85 µm × 20 µm for a zone at the inlet. The results are presented in Tables 5.2 to 5.4 for the different experimental conditions. From the particle counts, the particle densities per unit ml were calculated for each zone. Those values were then normalized by dividing by the particle density for the feed suspension to reflect the local extent of dilution accompanying the advection. A sample plot of the normalized density versus the position at the centre of each zone is shown in Fig 5.2 a.

A corresponding image obtained in area 2, at the center of the micro-model, is shown in figure 3.5b. Calculations similar to above were done for area 2 within the micro-model for each flow condition. A sample plot of the particle density profile is shown in Fig 5.2 b. Unlike for area 1, the width of the strips of the zones for area 2 varied with the micro-model configuration in order to keep the suspension volume examined the same, as was discussed in section 3.3.2

It is important to emphasize that the pictures were taken when it appears that the leading front of particles was passing through the field of view in the microscope for both areas 1 and 2. The few leading particles do indeed pass through the field before exposures were taken. A frame was selected for analysis from the high-speed imaging. Thus, for each picture, it is not clear which section of the transition zone was recorded and absolute number of particles cannot be compared from one set of experiments to another. Until the data was processed, as to be soon described, the primary statement that can be made is that the local particle density errors associated with undercounting because of particles obscuring other are expected to be small.

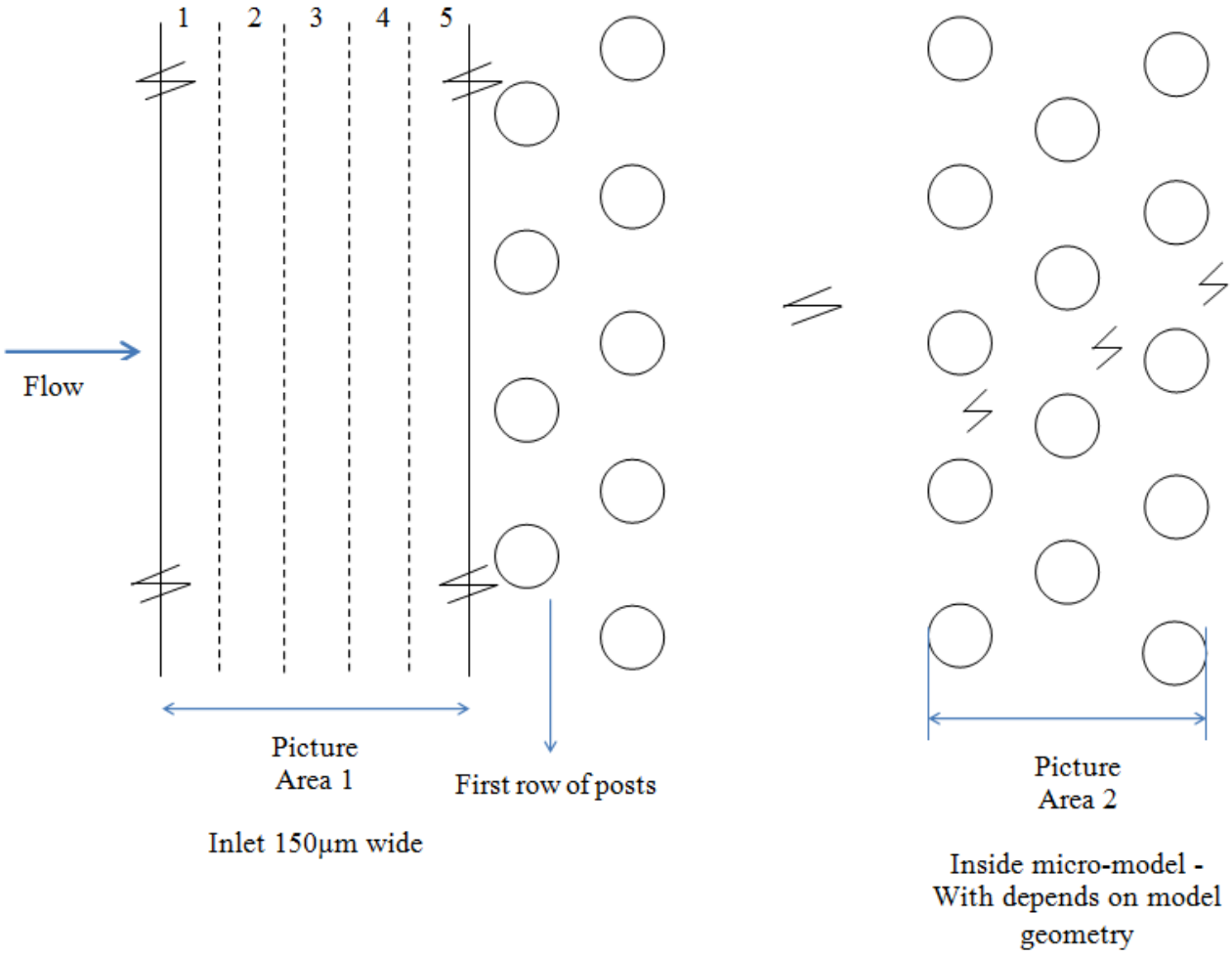

Figure 5.1 Schematic of test cell area used for particle concentration analysis, inlet (area1) and inside micro-model (area 2)

Table 5.2 Particle counts in the inlet and inside of micro-model for Conf. I

Experiment Condition				Particle Count									
				Inlet					Inside				
Micro-Model Configuration	Particle Diameter	Flow rate	Concentration Level	1	2	3	4	5	1	2	3	4	5
I	200 nm	slow	1	1243	1204	1139	1058	985	799	786	776	764	749
			2	2735	2568	2477	2372	2213	1869	1827	1814	1781	1746
I	500 nm	slow	1	1467	1358	1322	1258	1152	1041	1022	987	969	941
			2	2696	2487	2316	2213	2018	1842	1788	1761	1728	1707
I	1500 nm	slow	1	1493	1435	1362	1268	1140	1035	1024	1003	989	968
			2	3008	2880	2723	2508	2250	2070	2004	1946	1875	1836
I	200 nm	Int	1	1298	1221	1105	1016	949	486	479	468	459	438
			2	2709	2628	2534	2367	2198	1899	1866	1836	1793	1737
I	500 nm	Int	1	1374	1344	1209	1129	1046	901	889	876	853	840
			2	2682	2547	2408	2298	2123	1877	1823	1772	1724	1662
I	1500 nm	Int	1	1443	1319	1191	1109	1012	855	822	789	748	719
			2	2939	2831	2673	2487	2253	2082	2055	1982	1904	1841
I	200 nm	High	1	1236	1162	1089	1009	952	505	491	485	465	451
			2	2709	2594	2499	2375	2249	1862	1853	1823	1784	1751
I	500 nm	High	1	1303	1212	1141	1065	978	852	827	803	789	774
			2	2570	2441	2324	2214	2010	1791	1751	1686	1604	1544
I	1500 nm	High	1	1347	1229	1111	1009	952	815	786	759	725	699
			2	2850	2712	2549	2354	2133	1980	1920	1874	1814	1784

Table 5.3 Particle counts in the inlet and inside of micro-model for Conf. II

Experiment Condition				Particle Count									
				Inlet					Inside				
Micro-Model Configuration	Particle Diameter	Flow rate	Concentration Level	1	2	3	4	5	1	2	3	4	5
II	200 nm	slow	1	1272	1214	1080	979	921	789	779	768	761	749
			2	2631	2451	2267	2195	2060	1680	1662	1634	1628	1581
II	500 nm	slow	1	1365	1312	1217	1108	1025	974	963	934	899	880
			2	2885	2763	2618	2418	2213	1814	1739	1689	1658	1638
II	1500 nm	slow	1	1487	1368	1305	1280	1177	1019	1002	989	965	947
			2	2981	2828	2654	2450	2234	1739	1698	1643	1614	1602
II	200 nm	Int	1	1186	1152	1060	950	908	511	503	495	484	479
			2	2567	2448	2271	2081	1947	1509	1484	1458	1431	1395
II	500 nm	Int	1	1296	1229	1091	983	923	743	732	709	698	685
			2	2784	2594	2432	2289	2123	1767	1719	1686	1667	1635
II	1500 nm	Int	1	1395	1311	1258	1201	1152	850	836	816	795	783
			2	2843	2642	2493	2342	2108	1785	1722	1644	1586	1536
II	200 nm	High	1	1110	1055	976	891	855	450	442	435	429	419
			2	2529	2376	2192	2048	1943	1379	1355	1334	1326	1274
II	500 nm	High	1	1217	1149	995	902	840	629	615	600	593	580
			2	2732	2564	2438	2360	2160	1668	1586	1517	1476	1430
II	1500 nm	High	1	1289	1198	1101	1015	940	811	789	756	720	691
			2	2724	2585	2418	2265	2018	1658	1619	1584	1518	1479

Table 5.4 Particle counts in the inlet and inside of micro-model for Conf. III

Experiment Condition				Particle Count									
				Inlet					Inside				
Micro-Model Configuration	Particle Diameter	Flow rate	Concentration Level	1	2	3	4	5	1	2	3	4	5
III	200 nm	slow	1	1279	1219	1162	1045	989	806	796	786	774	760
			2	2898	2789	2651	2454	2288	1734	1692	1664	1575	1502
III	500 nm	slow	1	1411	1349	1258	1153	1072	1009	995	977	957	935
			2	2937	2804	2622	2453	2253	1664	1647	1623	1611	1595
III	1500 nm	slow	1	1471	1401	1305	1216	1107	1085	1064	1039	1022	1002
			2	2957	2829	2658	2489	2235	2039	2025	1958	1920	1889
III	200 nm	Int	1	1309	1263	1124	1022	962	504	492	476	469	455
			2	2813	2690	2526	2358	2213	1647	1617	1584	1548	1536
III	500 nm	Int	1	1411	1321	1253	1209	1080	909	899	881	869	839
			2	2804	2703	2616	2496	2325	1847	1799	1748	1716	1686
III	1500 nm	Int	1	1410	1319	1191	1083	999	892	876	859	845	829
			2	2868	2774	2636	2453	2234	1962	1926	1896	1808	1755
III	200 nm	High	1	1149	1091	1001	912	863	490	479	468	453	440
			2	2486	2322	2115	1956	1856	1478	1449	1428	1400	1364
III	500 nm	High	1	1296	1263	1192	1083	994	819	789	775	763	744
			2	2715	2580	2460	2280	2103	1679	1652	1628	1602	1553
III	1500 nm	High	1	1347	1262	1128	1032	938	829	794	771	748	725
			2	2852	2703	2612	2459	2205	1943	1886	1844	1794	1776

Fig. 5.2, 5.3 and 5.4 show density profiles for different size particles for fast flow conditions (Table 3.2). These are in the transition zones outside and inside the micro-model. For laminar flow in the Hele-Shaw cell and a suspension displacing a pure solvent, a side view at an instant would have shown a parabolic contour of the material boundary separating the two fluids, as illustrate in Fig. 5.5 a. The sharpness of the boundary would be influenced by how fast particles undergo lateral displacements. The particle density,, averaged over the flow cross-section, would exhibit a profile associated with the diagram, Fig 5.5 b. The normalized solute density ranged from 0 to 1, with x=0 set at the location of solute injection. With data recovered from only a small section of the test sections, the full density profile shown in Fig 5.5 b cannot be recovered.

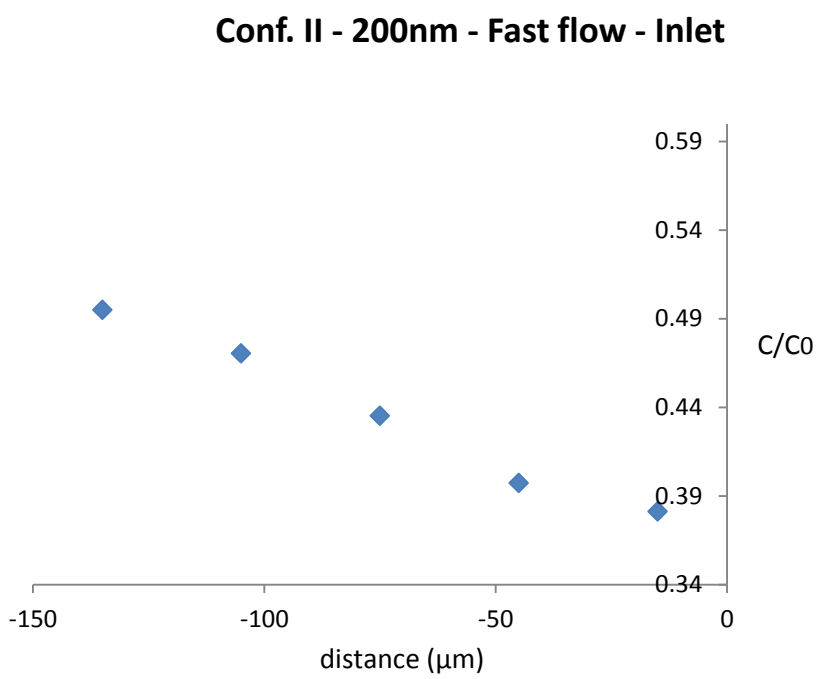

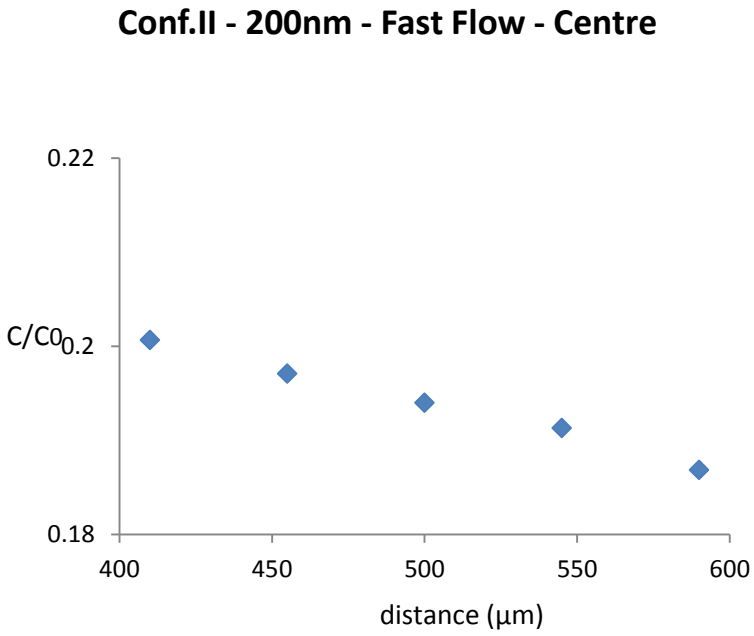

Figure 5.2 Concentration profile at the inlet area of micro-model II, 200nm particle and fast flow rate. Each point on the graph represents the normalized number of particles at each region of area.

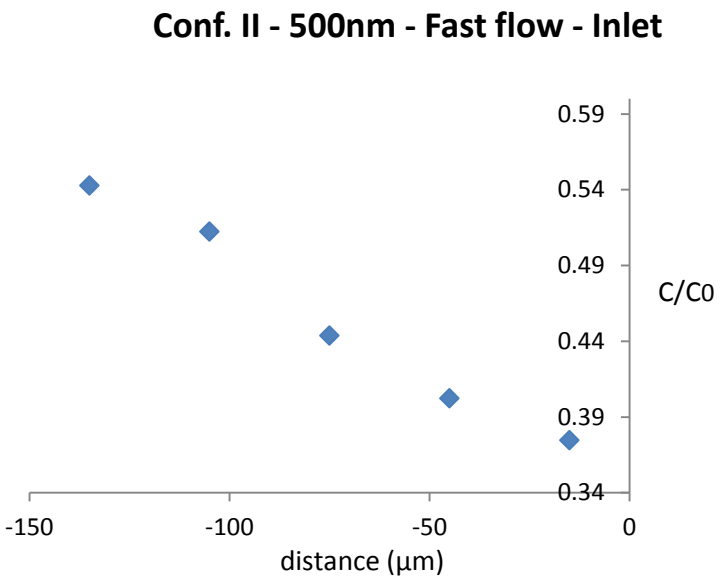

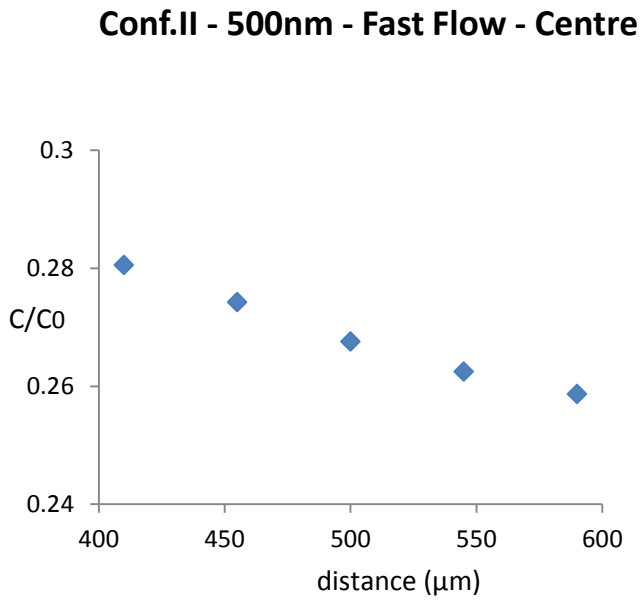

Figure 5.3 Concentration profile at the inlet area of micro-model II, 500nm particle and fast flow rate. Each point on the graph represents the normalized number of particles at each region of area.

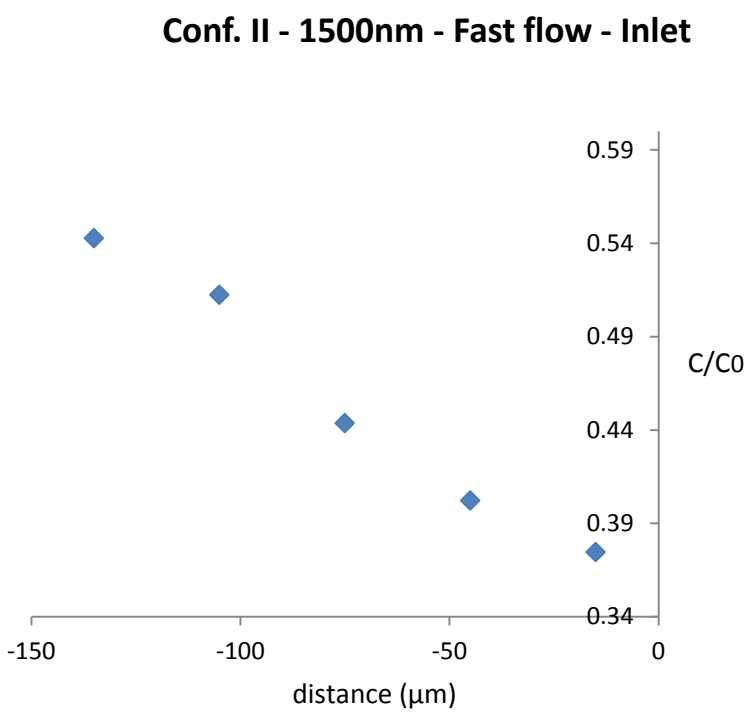

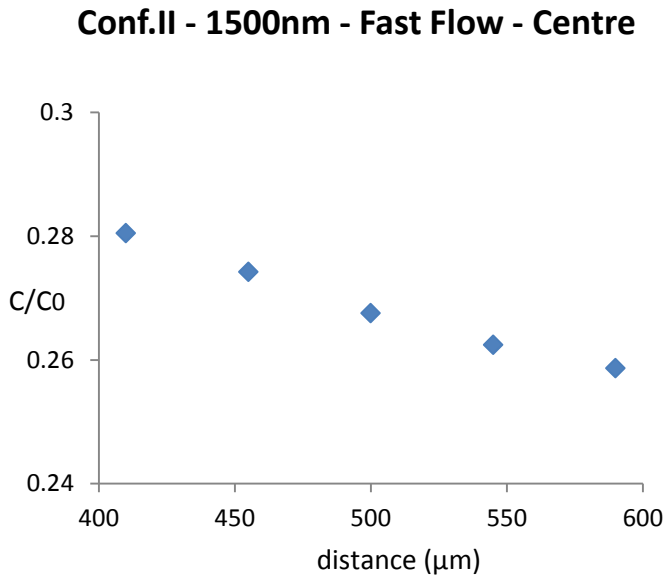

Figure 5.4 Concentration profile at the inlet area of micro-model II, 1500nm particle and fast flow rate. Each point on the graph represents the normalized number of particles at each region of area.

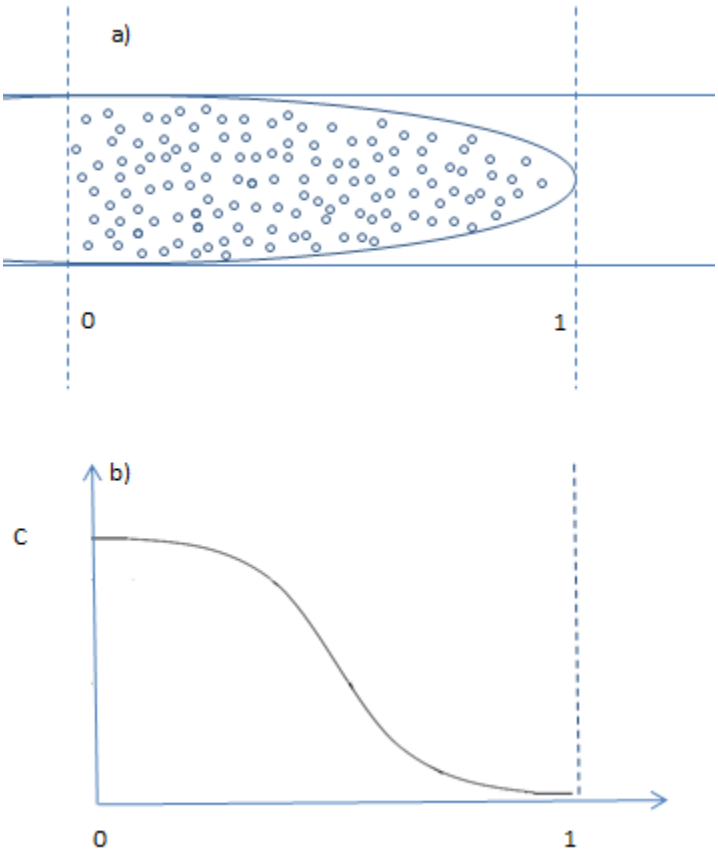

Figure 5.5 For laminar flow in the Hele-Shaw cell and a solution displacing a pure solvent, a side view at an instant would show a parabolic contour of the material boundary separating the two fluids, (a) and Concentration data recovered from sections at the leading edge of solute concentration (b)

5.2 Estimation of Longitudinal Dispersion Coefficients

The basis for estimating diffusion coefficients from the data obtained is as follows.

Consider a domain through which a solvent is being suddenly displaced by a suspension

at constant average velocity U. A balance equation for the spatial-temporal distribution of the particle density, averaged over the cross-section of flow, C(x), is given as (Fried and Combarnous, 1971)

$$K_L \frac{\partial^2 C}{\partial x^2} - U \frac{\partial C}{\partial x} = \frac{\partial C}{\partial t} \qquad (5.1)$$

For a step input function at x=0, the boundary and initial conditions are:

$$C\,(\,x = 0,\; t > 0\,) = C_0$$

$$C\,(\,x = \infty,\; t \geq 0\,) = 0$$

$$C\,(\,x \geq 0,\; t = 0\,) = 0$$

Applying Laplace transform,

$$\bar{C} = \int_0^\infty e^{-pt}\, C(x,t)dt \qquad (5.2)$$

with

$$L\left[\frac{\partial C}{\partial t}\right] = -C(x,0) + p\bar{C}(x,p) \qquad (5.3)$$

each term of equation 5.1 is transformed

$$\mathrm{L}[\mathrm{K_L}\frac{\partial^2 \mathrm{C}}{\partial \mathrm{x}^2}] = \mathrm{L}\left[\mathrm{U}\frac{\partial \mathrm{C}}{\partial \mathrm{x}}\right] + \mathrm{L}[\frac{\partial \mathrm{C}}{\partial \mathrm{t}}] \qquad (5.4)$$

$$\mathrm{L}\left[\frac{\partial \mathrm{C}}{\partial \mathrm{x}}\right] = \mathrm{P}\,\bar{\mathrm{C}}\,(\mathrm{x},\mathrm{t}) \qquad (5.5)$$

$$L[\mathrm{K_L}\frac{\partial^2 \mathrm{C}}{\partial \mathrm{x}^2}] = \mathrm{K_L}\frac{\partial^2 \bar{\mathrm{C}}}{\partial \mathrm{x}^2} \quad (5.6)$$

$$\mathrm{L}\left[\mathrm{U}\frac{\partial \mathrm{C}}{\partial \mathrm{x}}\right] = \mathrm{U}\frac{\partial \bar{\mathrm{C}}}{\partial \mathrm{x}}$$

to yield

$$\mathrm{K_L}\frac{\partial^2 \bar{\mathrm{C}}}{\partial \mathrm{x}^2} - \mathrm{U}\frac{\partial \mathrm{C}}{\partial \mathrm{x}} = \mathrm{P}\bar{\mathrm{C}} \quad (5.7)$$

$$\bar{\mathrm{C}}\ (\ \mathrm{x} = 0,\ \mathrm{t} > 0\ ) = \mathrm{C_0}/\mathrm{p}$$

$$\bar{\mathrm{C}}\ (\ \mathrm{x} = \infty,\ \mathrm{t} \geq 0\ ) = 0$$

$$\bar{\mathrm{C}}\ (\ \mathrm{x} > 0,\ t = 0\ ) = 0$$

The solution of this differential equation is:

$$\bar{C} = \frac{C_0}{p}\exp(\frac{U-(U^2+4pK)^{0.5}}{2K_L}x) = C_0 exp\left(\frac{Ux}{2K_L}\right).\ \frac{1}{p}\ exp\ [\ \frac{-x}{{K_L}^{0.5}}\left(\frac{U^2}{4K_L}+p\right)^{0.5}\ ] \quad (5.8)$$

Using a Laplace transform table, the inversion is:

$$C = \frac{C_0}{2}\ erfc\ \left(\frac{x-Ut}{2(K_L t)^{0.5}}\right) + \frac{C_0}{2}\ exp\left(\frac{Ux}{K_L}\right) erfc\left(\frac{x+Ut}{2(K_L t)^{0.5}}\right) \quad (5.9)$$

In this equation the second term is negligible compared to first term, thus the final solution of the dispersion equation may be written as a normal distribution function:

$$\frac{C}{C_0} = \frac{1}{2}\ erfc\ \left(\frac{x-Ut}{2(K_L t)^{0.5}}\right) = \frac{1}{2} - \frac{1}{2} erf\left(\frac{x-Ut}{2(K_L t)^{0.5}}\right) = 1 - F(x) \quad (5.10)$$

In which F(x) is the cumulative distribution function

$$F(x) = \frac{1}{2} + \frac{1}{2} erf\left(\frac{x-\mu}{\sqrt{2}\,\sigma}\right) \quad (5.11)$$

Here μ is the expected location of the inflection point moving at the average velocity of the flow and σ is the standard deviation.

In Fig 5.6, $\frac{C}{C_0}$ is drawn as a function of x, the standard deviation $\sigma = (2K_L t)^{0.5}$. For a

normal distribution function

$$Z = \frac{x-\mu}{\sigma} \quad (5.12)$$

Z = 1, x = μ + σ F (1) = 0.84

Z = -1, x = μ - σ F (-1) = 0.16

The width of the transition zone is a measure of rate of dispersion. If the width is defined as e = 2 σ, then

$$e = x_{0.16} - x_{0.84} = 2\,(2K_L t)^{0.5} \quad (5.13)$$

And from this expression, the longitudinal dispersion coefficient K_L is obtained as

$$K_L = \frac{(x_{0.16}-x_{0.84})^2}{8t} \quad (5.14)$$

5.2.1 Processing of data for K_L

In order to estimate the longitudinal dispersion coefficients from data in the present study, cumulative frequency distribution plots like Fig. 5.6 were generated for the Hele-Shaw region. Estimation of K_L for the region inside the micro-model is more challenging because the conditions at the inlet to the model are not stationary. The transition region within the Hele-Shaw cell is still evolving when the one within the micro-model is initiated. Thus the conditions imposed to arrive at Eq. 5.7 are not applicable. Analysis for the micro-model section has thus been deferred as part of future work. Hence only the results for the Hele-Shaw region are presented in the following.

In Eq. 5.14, estimation of K_L requires that values of distance x be determined for C/Co values of 0.84 and 0.16. The data seldom extends to that range and therefore a profile that fits the data had to be generated. A single factor Boltzmann equation

$$G(x) = \frac{1}{1+e^{(x-x½)\varphi}} \qquad (5.15)$$

was applied. In the expression, x½ is the location where G(x) = C/Co = 0.5 in the experimental data. A second point of the experimental density profile was chosen so that the constant φ in Boltzmann equation can be evaluated. Values for the resulting function G(x) are calculated and plotted.

For example, for 200 nm diameter particles in suspension flowing through the configuration II micro-model,

X½ is at a distance of 10000-135μm= 9865 μm from the injection port into the test cell. From data, G(x) = 0.5 at this location. Similarly, where G(x) =0.381, x = 9985 μm. Use of these numbers lead to the constant φ estimate to be 0.004033 for the run and the image analyzed. Values of G(x) calculated at other points are compared with the remaining experimental values in Table 5.5. The agreement is good. The data have also been plotted on the G(x) curve in Fig. 5.7 from extrapolation; values of x for G(x) equals 0.16 and 0.84 were estimated.

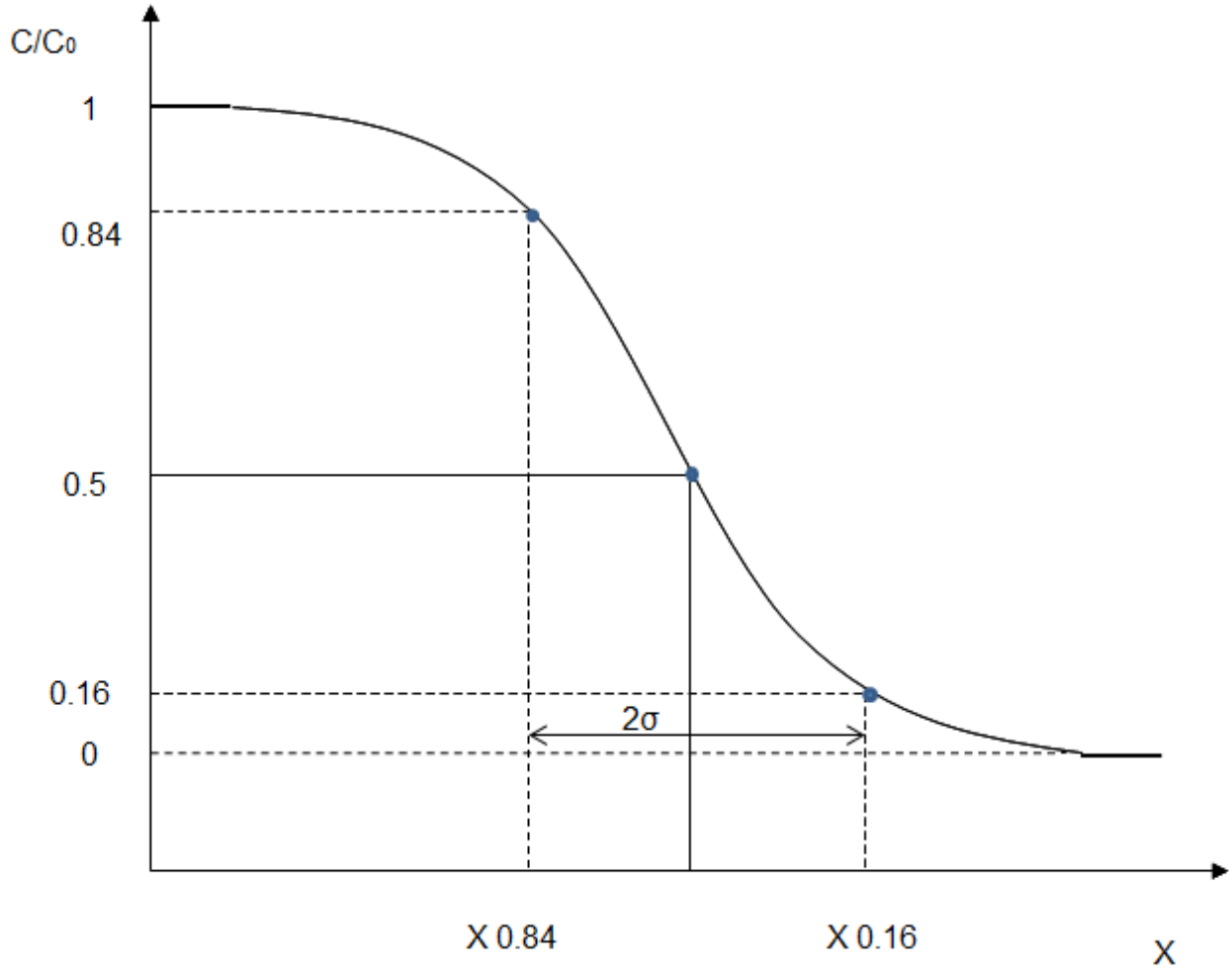

Figure 5.6 The Classical error function concentration profile

The values for σ were ± 417 μm, and since the image was recorded at 4.1 minutes (see Table in Appendix D) after the suspension was admitted into the test cell, the dispersion coefficient could be evaluated from

Equation 5.14 as

$$K_L = \frac{(417+417)^2}{8*60*4.1} = 354.71$$

Dispersion coefficients for the different runs were estimated as above and presented in Table 5.6.

Table 5.5 Concentration values obtained from experimental data versus concentration values obtained from single factor Boltzmann equation

X, µm	$X-X_{0.5}$	F(X) Boltzmann Eq.	F(X) experiment
-135	0	0.5	0.49
-105	30	0.47	0.47
-75	60	0.44	0.43
-45	90	0.41	0.39
-15	120	0.38	0.38

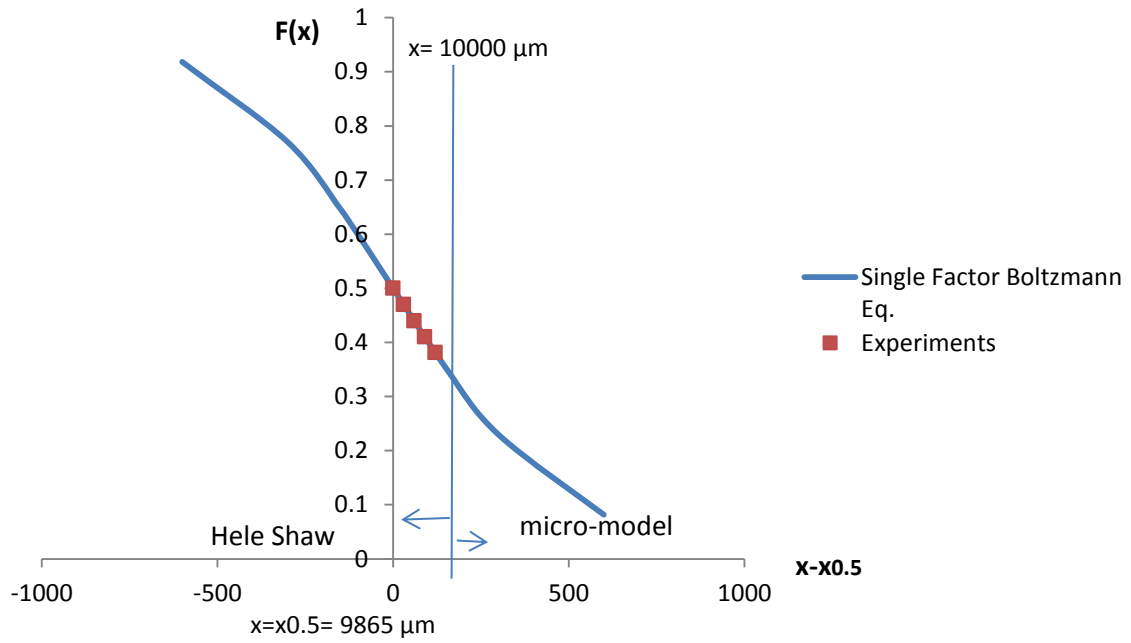

Figure 5.7 Concentration profiles at the inlet and centre of the micro-model obtained from experimental results and theoretical single factor Boltzman equation for 200nm, Conf.II and fast flow.

Concentration 1		Concentration 2	
Conf.I		**Conf.I**	
200	**inlet**	**200**	**inlet**
s	41	**s**	32
i	125	**i**	92
f	296	**f**	235
500	**inlet**	**500**	**inlet**
s	27	**s**	24
i	101	**i**	82
f	195	**f**	171
1500	**inlet**	**1500**	**inlet**
s	22	**s**	17
i	94	**i**	73
f	170	**f**	159
Conf.II		**Conf.II**	
200	**inlet**	**200**	**inlet**
s	48	**s**	38
i	143	**i**	130
f	354	**f**	315
500	**inlet**	**500**	**inlet**
s	35	**s**	28
i	124	**i**	110
f	216	**f**	201
1500	**inlet**	**1500**	**inlet**
s	27	**s**	24
i	103	**i**	75
f	190	**f**	174
Conf.III		**Conf.III**	
200	**inlet**	**200**	**inlet**
s	44	**s**	35
i	129	**i**	116
f	308	**f**	271
500	**inlet**	**500**	**inlet**
s	32	**s**	27
i	114	**i**	101
f	208	**f**	187
1500	**inlet**	**1500**	**inlet**
s	25	**s**	21
i	99	**i**	68
f	185	**f**	109

Table5.6. Inlet Dispersion Coefficient values $K_L \times 10^{12}$ (m^2 /s) from experimental data for Conf. I, Conf. II and Conf. III

5.3 Discussion

The results in Tables 5.2 to 5.4 and 5.6 reflect the dispersion of suspensions of finite size particles at concentrations considered dilute but are such that the collision frequency between particles would be high. As presented in Table 5.6, dispersion coefficients have been calculated for the entry portion of the test cell that was 10 mm long; see Fig 3.1 b. This section involved Hele-Shaw flow between two parallel plates, and a suspension at a constant particle population density was the feed. This displaced water was initially particle free. The particle density profile could not be determined for the entire length of the section that was originally designed to steady the fluid flow before the suspension enters the micro-model section. Dispersion in the latter was of primary interest. The unexpected consequence of having the Hele-Shaw section was that the suspension became dispersed before entering the micro-model. This makes an evaluation of the dispersion coefficient in the micro-model section more challenging. This analysis is still in progress.

For suspensions, inter-particle collisions would have the effect of displacing particles in the direction lateral to the flow, similar to diffusive effects for solutes within a lateral concentration gradient. In the Hele-Shaw cell, advection will be dominant compared to shear-induced "diffusive" effects. Within the micro-model, suspensions follow tortuous paths and the particles that have finite volumes and are heavier than the medium would deviate from streamlines – due to inertia and multi-body interactions.

The results in Table 5.6 are important for the validation of the experimental methods and for understanding dispersion of finite volume particles in dilute suspensions flowing in the laminar regime. Since the section is upstream of the different micro-model configurations, the degree of dispersion should be substantially independent of the configurations of the micro-models. The

results show that at a flow (e.g. slow) rate and for a particle diameter (e.g. 200 nm) at one concentration (e.g. level 1), the values of the dispersion coefficient would be the same within the limits of experimental errors. These are justified in the Table.

Trends are obvious from the results in Table 5.6. The rate of axial dispersion decreased with suspension concentration. Dispersion increased with the flow rate of suspension, i.e. as advection became more dominant. The rate of dispersion decreased with increasing particle size for apparently two reasons. The volume fraction of solids in the suspension increased with the diameter of the particles as shown in Table 5.1, and higher volume of particles would increase the frequency of collisions and lateral displacements at the expense of longitudinal movement. The second reason is that the drag is larger on the bigger particles and the slip velocity would be larger than for smaller sized particles.

CHAPTER 6

CONCLUSION

The transport of nano- and micro-particles in suspensions through micromodels of porous media has been studied experimentally under conditions that hydrodynamic factors dominate. Particle trajectories were not coincident with streamlines for the continuous phase, and particles show evidence of Brownian motion and drifts due to local velocity gradients in the suspending medium. The particles showed significant changes in speed as they traversed the media and the "slip condition" between particle and fluid seems to prevail for most of the domain. Larger particles travelled faster and further linearly into the porous medium than the smaller particles. Smaller particles, in turn, spread out axially more than the larger particles as they are carried through the medium. Dispersion was higher in the less porous structures.

These observations would appear to have consequences for using finite-sized particles for flow visualization studies in microfluidic devices and in micro-models.

A micro-model is valuable for observing and tracking particles but the flow characteristics in the structure require attention as the streamlines for the fluid and the trajectories (and velocities) of isolated particles may deviate significantly from what would be anticipated for an ideal filter,

Suspensions were dispersed in the Hele-Shaw section primarily by advection, and the extent was directly correlated to the flow rates and inversely correlated to the particle diameter, the solid volume fraction and the concentration.

It is of technological interest to continue the research in this domain. Obtaining a library of experimental data for different controlling parameters and validate the data with mathematical modeling will be useful to provide a roadmap for vast applications of particle transport in porous media.

REFERENCES

Acrivos, A., Batchelor, G.K., Hinch, E.J., Koch, D.L. and Mauri, R., 1992, Longitudinal shear-induced diffusion of spheres in a dilute suspension, J. Fluid Mech., 240, 651-657

Auset, M. and Keller, A.A., 2004, Pore-scale processes that control dispersion of colloids in saturated porous media, Water Resources Res., 40, W03503, doi: 10.1029/2003WR002800, 1-11

Avogadro, de Marsily 1984, The role of colloids in nuclear waste disposal. In Scientific Basis for Nuclear Waste Management VII, Materials Research Society Newyork; vol 26;p 495-505

Basset, A.B., 1888, A Treatise on Hydrodynamics, vol 2, Ch 21, Cambridge, Deighton, Bell and Co. (also Dover, 1961)

Batchelor, G.K., 1976, Brownian diffusion of particles with hydrodynamic interactions, J. Fluid Mech., 74, 1-29

Baumann, T., Toops, L. and Niessner, R., 2010, Colloid dispersion on the pore scale, Water Research, 44, 1246-1254

Boussinesq, J.V., 1885, Sur la resistance qu' Oppose un Liquide Indefini en Repos d'une sphere solide. Comptes Rendu, des Seances de l'Acadamie, 100, 935-7

Brenner, H. and Edwards, D.A., 1993, Macrotransport Processes, Butterworth-Heinemann

Brenner, H., 1980, a general theory of Taylor dispersion phenomena, PhysicoChem. Hydro, 1, 91-123

Brenner, H., 1982, a general theory of Taylor dispersion phenomena II An extension, PhysicoChem. Hydro., 3, 139-157

Brown, R.C., 1993, Theory of airflow through filters modelled as arrays of parallel fibers, Chem. Engg. Sci., 48(20), 3535-3543

Bungay, P.M. and Brenner, H., 1973, Pressure drop due to the motion of a sphere near the wall bounding a Poiseuille Flow, J. Fluid Mech., 60(1), 81-96

Chandrasekhar,S., 1943, Stochastic Problems in Physics and Astronomy, Rev. Mod. Phys., 15(1), 1-89

Chandrasekhar,S., 1949, Brownian motion, Dynamical Friction, and Stellar Dynamics, Rev. Mod. Phys., 21(3), 383-388

Champ, D. R., and Schroeter, J., 1988, Bacterial transport in fractured rock: A field-scale tracer test at the Chalk River Nuclear Laboratories, Water Sci. Technol., 20(11/12), 81-87.

Crowe,C., Sommerfield, M. and Tsuji, Y., 1998, Multiphase Flows with droplets and particles. Ch4. CRC Press, Boca Raton

Dagan, Z., Weinbaum, S. and Pfeffer, R., 1982, General theory for the creeping motion of a finite sphere along the axis of a circular orifice, J. Fluid Mech., 117, 143-170

Di Carlo, D.; Irimia,D. ; Tompkins, R. G. ; Toner, M., 2007, Continuous inertial focusing, ordering, and separation of particles in microchannels, PNAS.,104,No.48,18892-18897

DiMarzio, E. A.; Guttman, C. M. Macromolecules 1970, 3, 131-146. 62

Drummond, J.E. and Tahir, M.I., 1984, Laminar viscous flow through regular arrays of parallel solid cylinders, Int. J. Multiphase Flow, 10(5), 515-540

Eckstein, E.C., Bailey, D.G. and Shapiro, A.H., 1977, Self-diffusion of particles in shear flow of a suspension, J. Fluid Mech., 79(1), 191-208

Edwards, D.A., Shapiro, M. and Brenner, H., 1992, Dispersion and reaction in two-dimensional model porous media, Phys. Fluids A, 5(4), 837-848
Einstein A. Investigation on the Theory of the Brownian Movement Edited with notes by R.Furth. New York: Dover. 1956

Faxen, H., 1922, Der Widerstand gegen die Bewegung einer starren Jugel in einer zum den Flussigkeit, die zwischen zwei parallelen Ebenen Winden eigenschlossen ist, Annalen der Physik, 68, 89-119

Falade A,Brenner H., 1988, First-Order wall curvature effects upon the Stokes resistance of a spherical particle moving in close proximity to solid wall.J Fluid Mech.;193,533-568

Fetter, C.W., Contaminant Hydrogeology, Macmillan NY, 1993, p44

Frank, M., Anderson, D., Weeks, E.R. and Morris, J.F., 2003, Particle migration in pressure-driven flow of a Brownian suspension, J. Fluid Mech., 493, 363-378

Fried, J.J.;Combarnous, M.A., Dispersion in porous media, Advances in hydroscience. 1971, 7

Ganatos, P., Pfeffer, R. and Weinbaum, S., 1980, a strong interaction theory for the creeping motion of a sphere between plane parallel boundaries: Pt 2 Parallel Motion, J. Fluid Mech., 99(4), 755-783

Gordon, D., 1978, Numerical Calculations on viscous flow fields through cylinder arrays, Computers and Fluids, 6, 1-13

Griffith, I.M.and Stone, H.A., 2012, Axial dispersion via shear-enhanced diffusion in colloidal suspensions, EPL, 97, 58005, 6p.

Grindrod, P., M. S. Edwards, J. J. W. Higgo, and G. M. Williams 1996, Analysis of colloid and tracer breakthrough curves, J. Contam. Hydrol. 21, 243– 253.

Happel, J. and Brenner, H., 1965, Low Reynolds number Hydrodynamics. Prentice-Hall, Englewood Cliffs, NJ
Happel, J. and Brenner, H., 1973, Low Reynolds Number Hydrodynamics, Ch. 7, 2nd Ed., Noordhoff

Happel, J., 1959, viscous flow relative to arrays of cylinders, A.I.Ch.E. J., 5(2), 174-177

Hartnett, J.P. and Kostic, M., 1989, Heat Transfer to Newtonian and Non-Newtonian Fluids in Rectangular ducts, Adv. In Heat Transfer, vol 19, 247-356

Hellou, M., Martinez, J. and El Yazidi, M., 2004, Stokes flow through microstructural model of fibrous media, Mechanics Research Communications, 31, 97-103

Heyder J, Gebhar J, Rudolf G, Schiller CF, Stahlhofen W., 1986, Deposition of particles in the human respiratory tract in the size range 0.005-15 micrometer. J Aerosol Science, 17(5), 811

Horn, F.J.M., 1971, Calculation of dispersion coefficients by means of moments, AIChE J., 17, 613-620

Ingham, D.B., Hildyard, M.L. and Heggs, P.J., 1991, the particle collection of an array of cylinders using the boundary element method, Engg Analysis with Boundary Elements, 8(1), 36-44

Javadpour, F.; Amrein, M.; Jeje, A., 2011, Multiscale, Experimental Study of Selective Blood-Cell, Filtration in Fibrous Porous Media, J Transp. Porous Med., 91: 913-926

Israelachvili, J.N., 2011, Intermolecular and surface forces, rev. 3rd ed., Academic Press

James, S. C., Chrysikopoulos C. V. 2003, Analytical solutions for monodisperse and polydisperse colloid transport in uniform fractures, Colloids Surf. A, 226(1– 3), 101– 118.

Karadimitriou, N.K. and Hassnizadeh, S.M., 2011, A review of micromodels and their use in two-phase flow studies, Vadose Zone J. doi:10.2136/vzj2011.0072,

Kirsch, A.A. and Fuchs, N.A., 1967, The fluid flow in a system of parallel cylinders perpendicular to the flow direction at small Reynolds numbers, J. Phys. Soc. Jpn., 22, 1251-1255

Kuwabara, S., 1959, The forces experienced by randomly distributed parallel circular cylinders or spheres in a viscous flow at small Reynolds numbers, J. Phys. Soc. Jpn., 14, 527-532

Lazouskaya, V., Jin, Y. and Or, D., 2006, Interfacial interactions and colloid retention under steady flows in capillary channels, J. Colloid and Interface Sci., 303, 171-184

Leal, L.G., 1980, Particle motions in a viscous fluid, Ann. Rev. Fluid Mech., 12, 435-476

Lee J, Koplik J., 1999, Microscopic motion of particles flowing through a porous medium. J Physics of Fluids; 1176-87

Maxey, M.R. and Riley, J.J., 1983, Equation of motion for a small rigid sphere in a non-uniform flow, Phys. Fluids, 26(4), 883-889

Mazo, R.M., Brownian motion; Fluctuations, Dynamics and Applications, Clarendon Press, Oxford, 2002

Mei, R., Lawrence, C.J. and Adrian, R., 1991, Unsteady drag on a sphere at finite Reynolds number with small fluctuations in the free-stream velocity, J. Fluid Mechanics, 223, 613

Michaelides,E.E. and Feng, Z.-G., 1996, Analogies between the transient momentum and energy equations of particles, Prog. Energy and Comb. Sci., 22, 147-162

Michaelides, E.E. and Roig, A., 2011, A Reinterpretation of the Odar and Hamilton data on the Unsteady Equation of Motion of particles, AIChE J., 57(11), 2997-3002

Natarajan, N.M. and Lakshmanan, S.M. 1972, Laminar flow in rectangular ducts: prediction of velocity profiles and friction factor. Indian J. Tech., 10, 435

Niehren, S., and W. Kinzelbach. 1998. Artificial colloid tracer tests: development of a compact on-line microsphere counter and application to soil column experiments. Journal of Contaminant Hydrology 35:249-259.

Odar, F. and Hamilton, W.S., 1964, Forces on a sphere accelerating in a viscous fluid. J. Fluid Mechanics, 18, 302-314

Oseen, C.W., 1927, Hydrodynamik, Leipzig, Akademische Verlagsgesellschaft

Penttinen, P., Timonen, K.L., Tiittanen, P., Mirme, A., Ruuskanen, J. and Pekkanen, J., 2001, Number concentration and size of particles in urban air: effects on spirometric lung function in adult asthmatic subjects, Environmental and Health Perspectives, 109(4), 319-323

Perkins, T.K. and Johnston, O.C., 1963, A review of diffusion and dispersion in porous media, Soc. Petr. Eng. J., SPE 480, 70-84

Perrin, C.L., Tardy, P.M.J., Sorbie, K.S. and Crawshaw, J.C.,2005, Experimental and modeling study of nwetonian and non-newtonian fluid flow in pore network micromodels, J. Colloid and Interface Science, 295, 542-550, 2006 (doi:10.1016/j.jcis.2005.09.012)

Pozrikidis, C., 1994, the motion of particles in the Hele-Shaw cell, J. Fluid Mech., 261, 199-222

Probstein, R.F., Physicochemical Hydrodynamics; and introduction, Butterworth, Boston, 1989, p114-121

Purday, H. F. P. 1949, an introduction to the mechanics of viscous flow, Dover Publ. Co., NY

Qu, W. and Mudawar, I., 2002, Analysis of three-dimensional heat transfer in micro-channel heat sinks, Int. J. Heat and Mass Transfer, 45, 3973-3985.

Ramachandran, A., 2013, A macrotransport equation for the particle distribution in the flow of a concentrated non-colloidal suspension through a circular tube, J. Fluid Mech., 734, 219-252

Reimus, P.W., 1995. The Use Synthetic Colloids in Tracer Transport Experiments in Saturated Rock Fractures. LA-13004-T, Los Alamos National Laboratory, Los Alamos, NM.

Reeks, M.W. and McKee, S., 1984, The dispersive effects of Basset history forces on particles in motion in a turbulent flow, Physics of Fluids, 27(7), 1573

Rubinstein, J. and Mauri, R., 1986, Dispersion and convection in periodic porous media, SIAM J. Appl. Math., 46(6), 1018-1023

Saffman, P.G., 1959, a theory of dispersion in a porous medium, J. Fluid Mech., 6(3), 321-349

Saffman, P.G., 1960, Dispersion due to molecular diffusion and macroscopic mixing in flow through a network of capillaries, J. Fluid Mech., 7(2), 194-208

Sangani, A.S. and Acrivos, A., 1982, Slow flow past periodic arrays of cylinders with application to heat transfer, Int. J. Multiphase Flow, 8(3), 193-206

Schöneborn, P.-R., 1975, the interaction between a single particle and an oscillating fluid, Int. J. Multiphase Flow, 2, 307-317

Shapiro, M., Kettner, I.J. and Brenner, H., 1991, Transport Mechanics and collection of submicrometer particles in fibrous filters, J. Aerosol Sci, 22(6), 707-722

Sirivithayapakorn , Keller A. ,2003, Transport of colloids in unsaturated porous media: A pore-scale observation of processes during the dissolution of air-water interface- Water Resources Research, Volume 39, Issue 12, December 2003

Stokes, G.G.,1851, on the effect of the internal friction of fluids on the motion of pendulums. Trans. Cambridge Philos. Soc., 9, 8

Taylor, G.I., 1953, Dispersion of soluble matter in solvent flowing slowly through a tube, Proc. Roy. Soc. A219, 186-203

Taylor, G.I., 1954, Conditions under which dispersion of a solute in a stream of solvent can be used to measure molecular diffusion, Proc. Roy. Soc., A225, 473-477

Vikhansky, A., 2009, Taylor dispersion in shallow micro-channels: aspect ratio effect, Microfluid Nanofluid, 7 91-95

Voir, D.J. and Michaelides, E.E., 1994, the effect of the history term on the motion of rigid spheres in a viscous fluid. Int. J. Multiphase Flow, 20, 547-_

Wang, C.Y., (2003), Stokes slip flow through square and triangular arrays of circular cylinders, Fluid Dynamics Research, 32, 233-246

Wilson, J.L. et al., 1988, the pore level spatial distribution and saturation of organic liquids in porous media, National Water Well Association, Dublin, pp. 107–133

Zheng, C. and Bennett, G.D. Applied Contaminant Transport Modeling: Theory and Practice, van Nostrand Reinhold NY, 1995

APPENDIX A

COMSOL SIMULATIONS

Figure A.1. Fluid streamlines for micro-model Configuration I generated by COMSOL

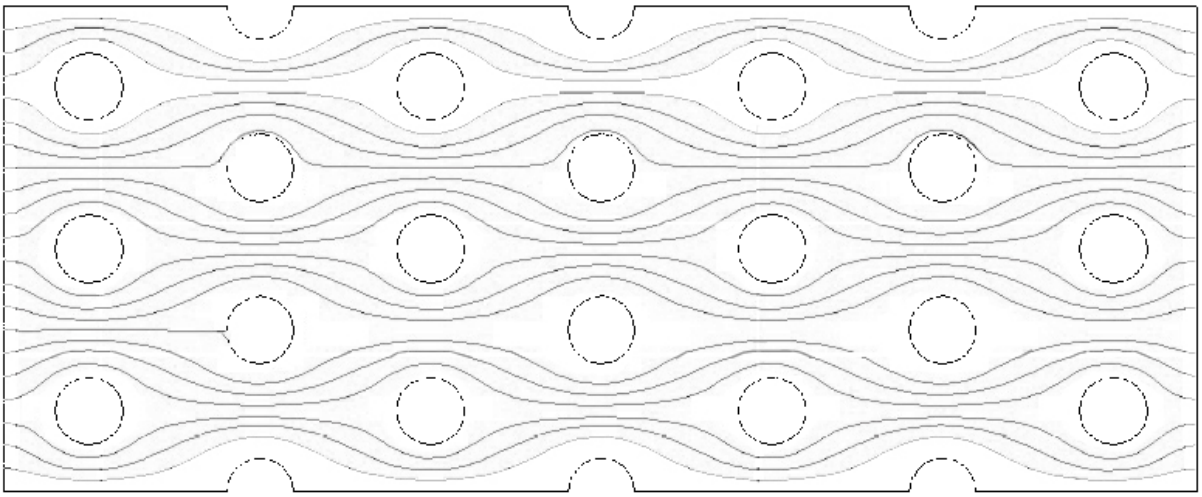

Figure A.2. Fluid streamlines for micro-model Configuration III generated by COMSOL

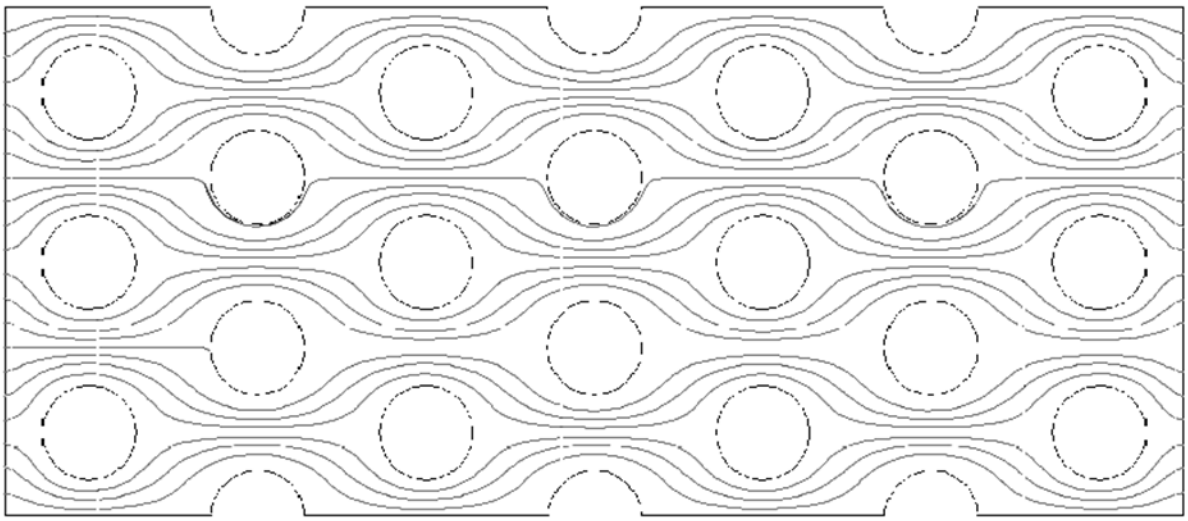

APPENDIX B

PARTICLE TRAJECTORY RESULTS

As explained in chapter 3, images from the displacement of particles are recorded by a high speed and high sensitivity camera with frame rate of up to 50 frames per second. Particles traversing the porous domain are tracked manually by ImageJ software. Results shown from figure 1 to 8 are examples of particles path-lines at different experiment condition such as flow rate, particle size and micro-model structures.

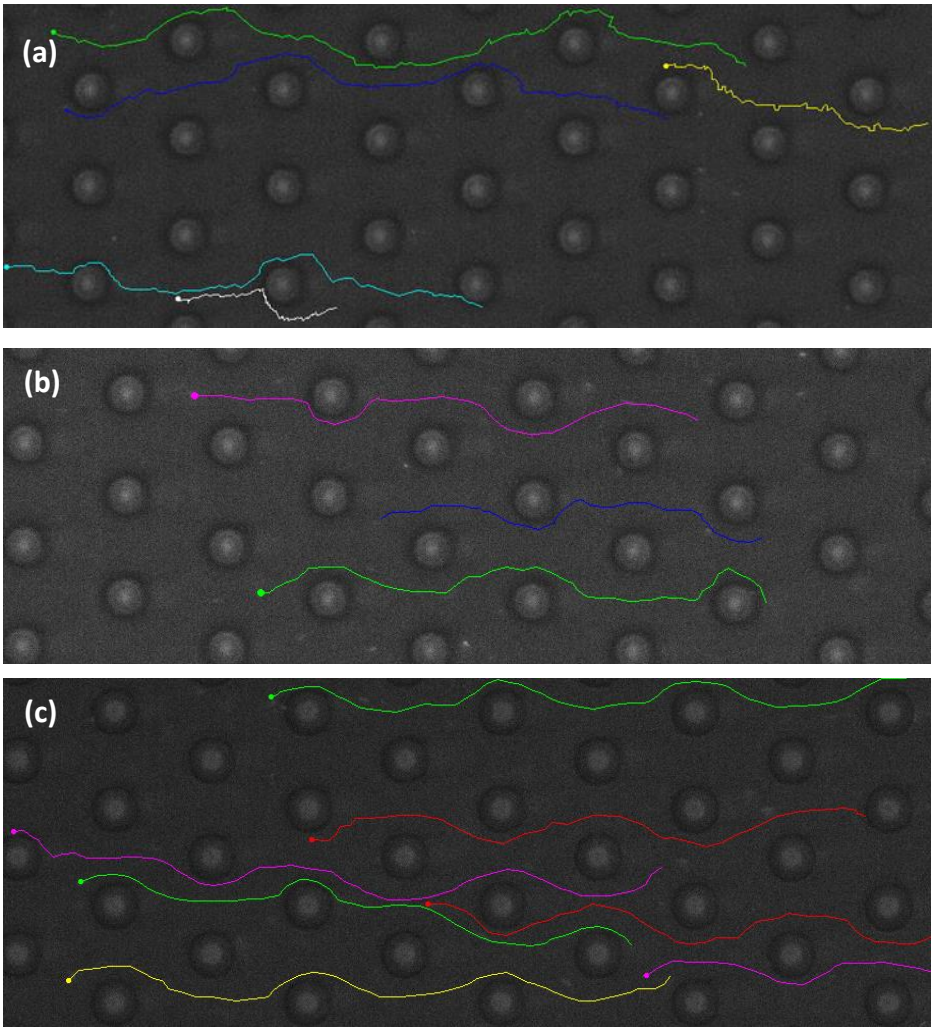

Figure B.1. Example of 200nm particle trajectory, 5-7 micromodel, at (a) Slow, (b) Intermediate and (c) High flow rates

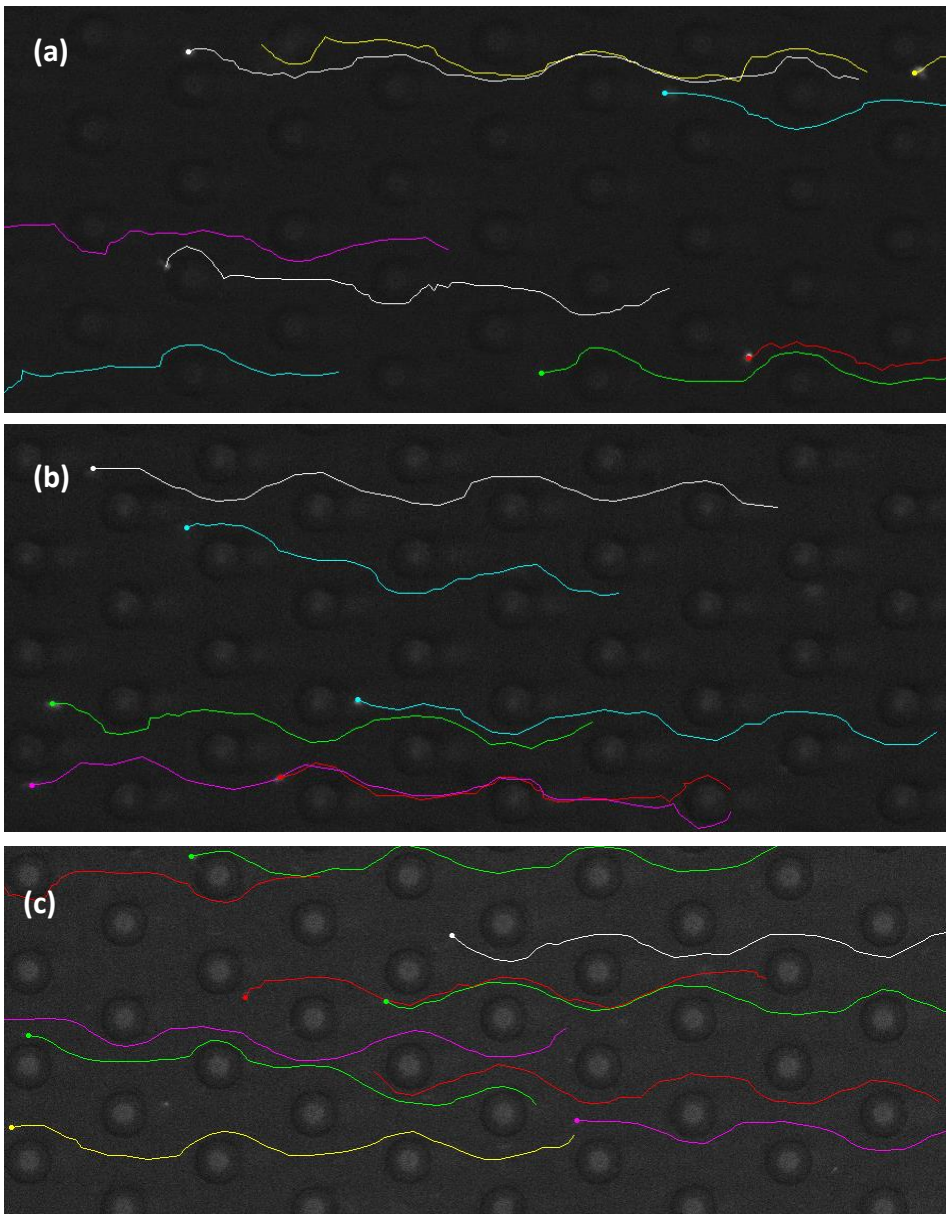

Figure B.2. Example of 500nm particle trajectory, 5-7 micromodel, at (a) Slow, (b) Intermediate and (c) High flow rates

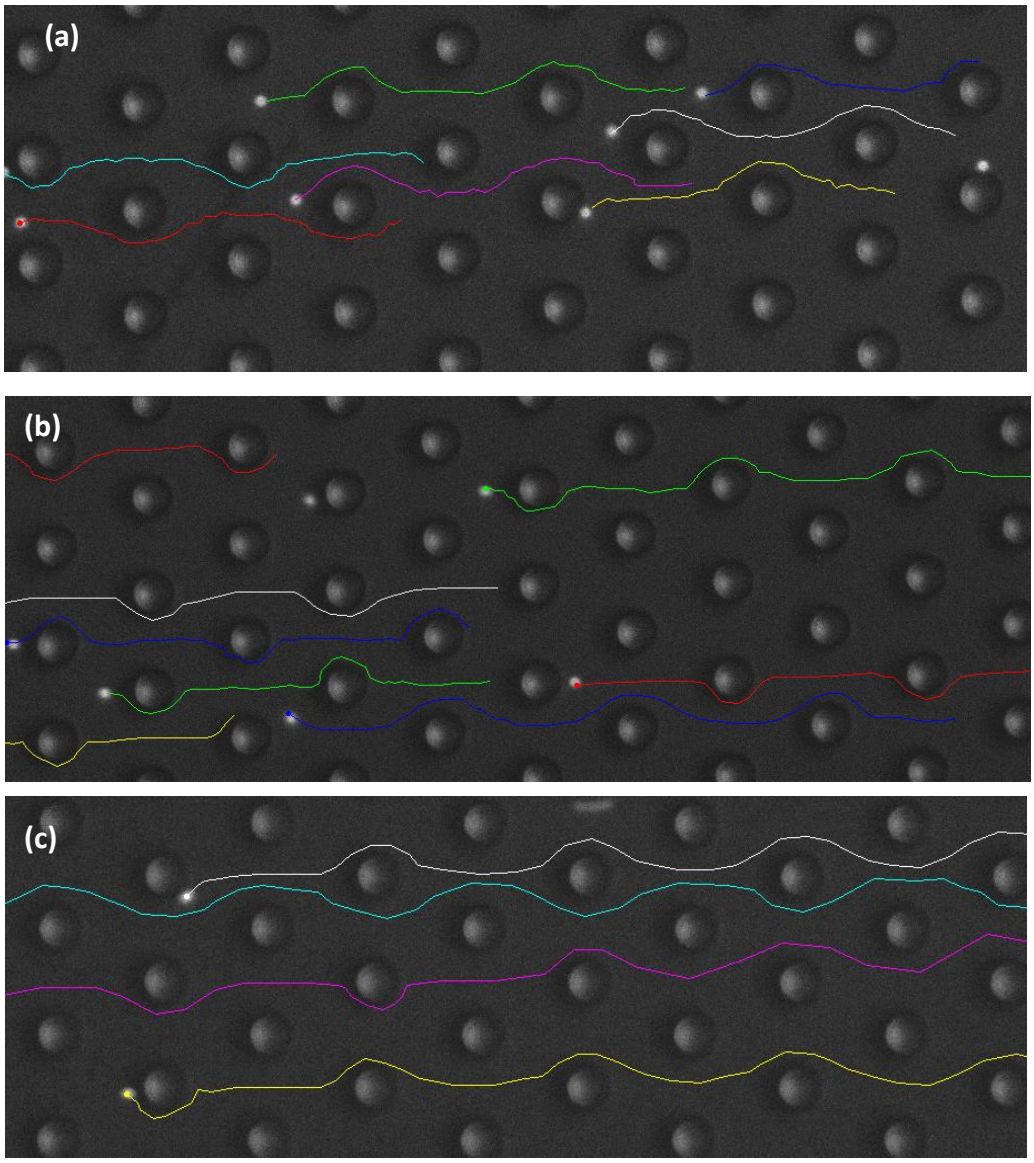

Figure B.3. Example of 1500nm particle trajectory, 5-7 micromodel, at (a) Slow, (b) Intermediate and (c) High flow rates

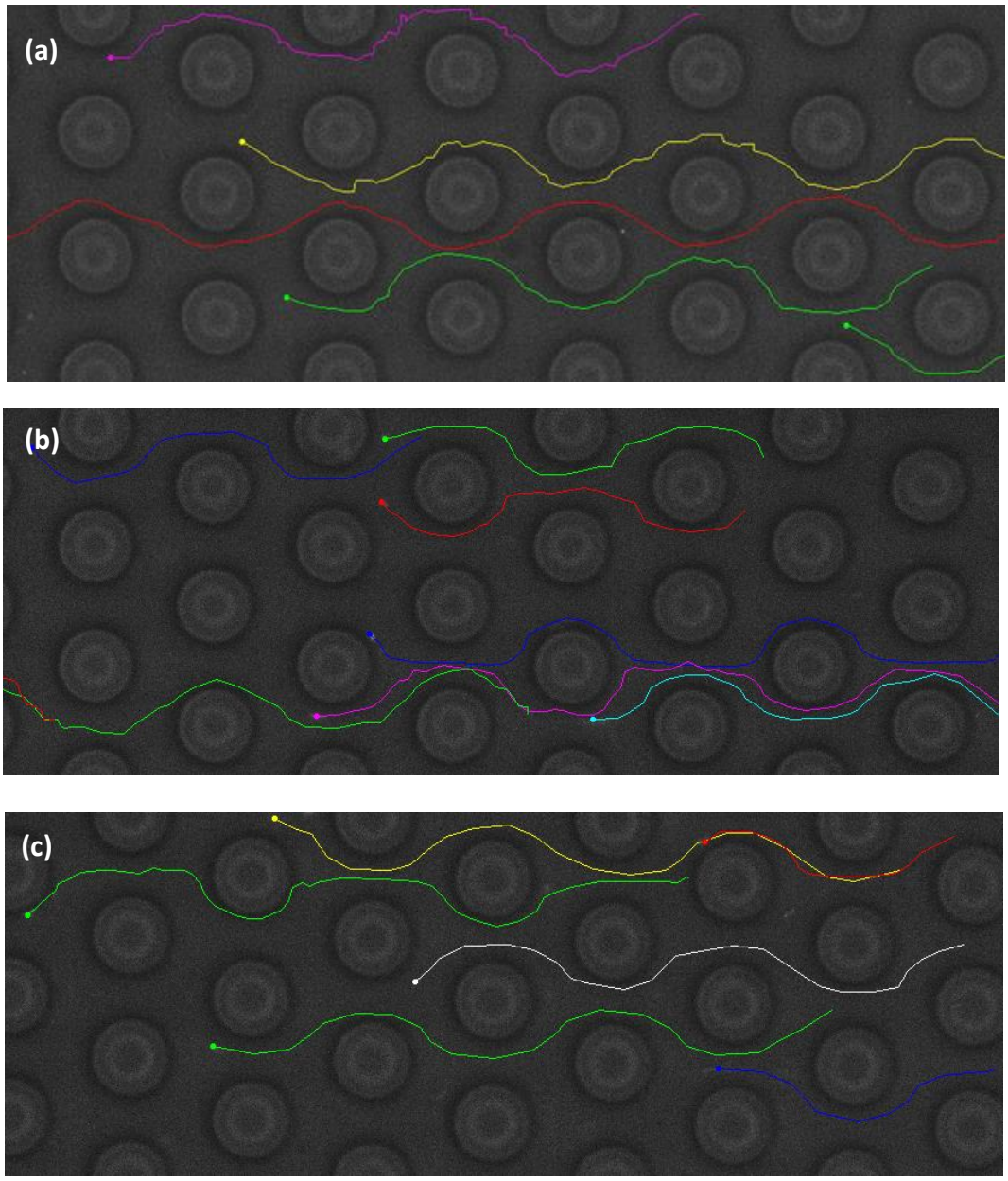

Figure B.4. Example of 200nm particle trajectory, 10-7 micromodel, at (a) Slow, (b) Intermediate and (c) High flow rates

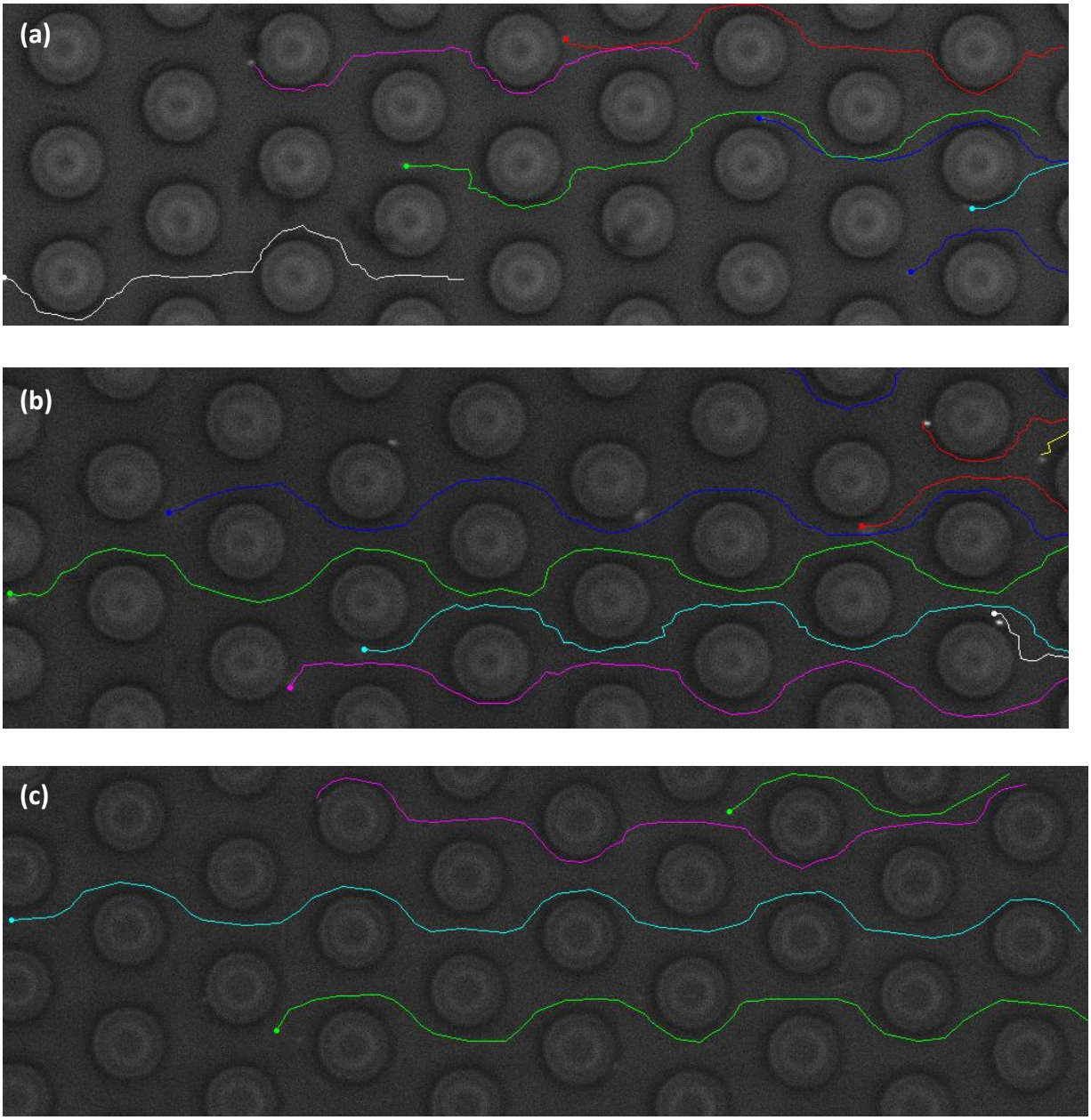

Figure B.5. Example of 500nm particle trajectory, 10-7 micromodel, at (a) Slow, (b) Intermediate and (c) High flow rates

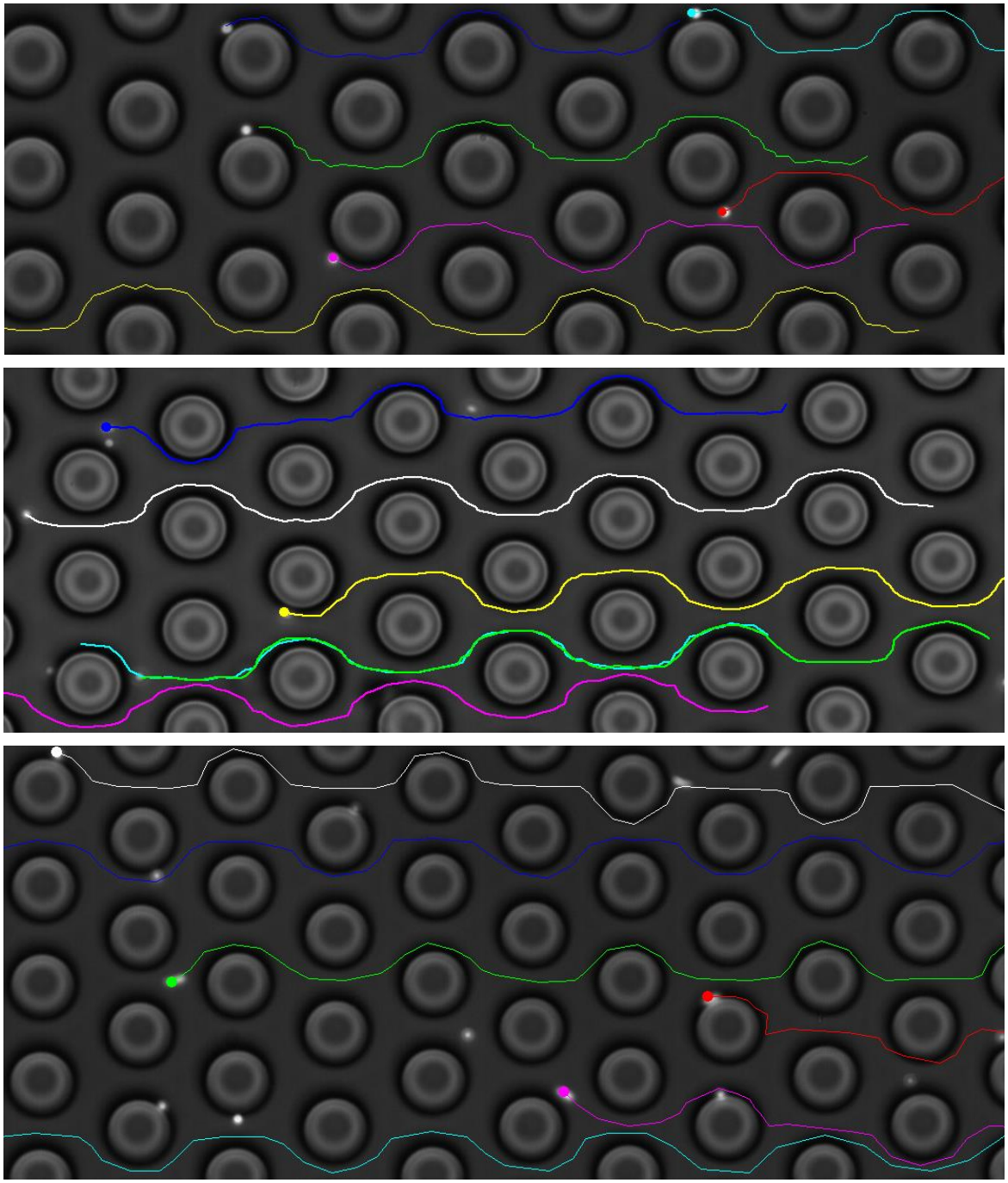

Figure B.6. Example of 1500nm particle trajectory, 10-7 micromodel, at (a) Slow, (b) Intermediate and (c) High flow rates

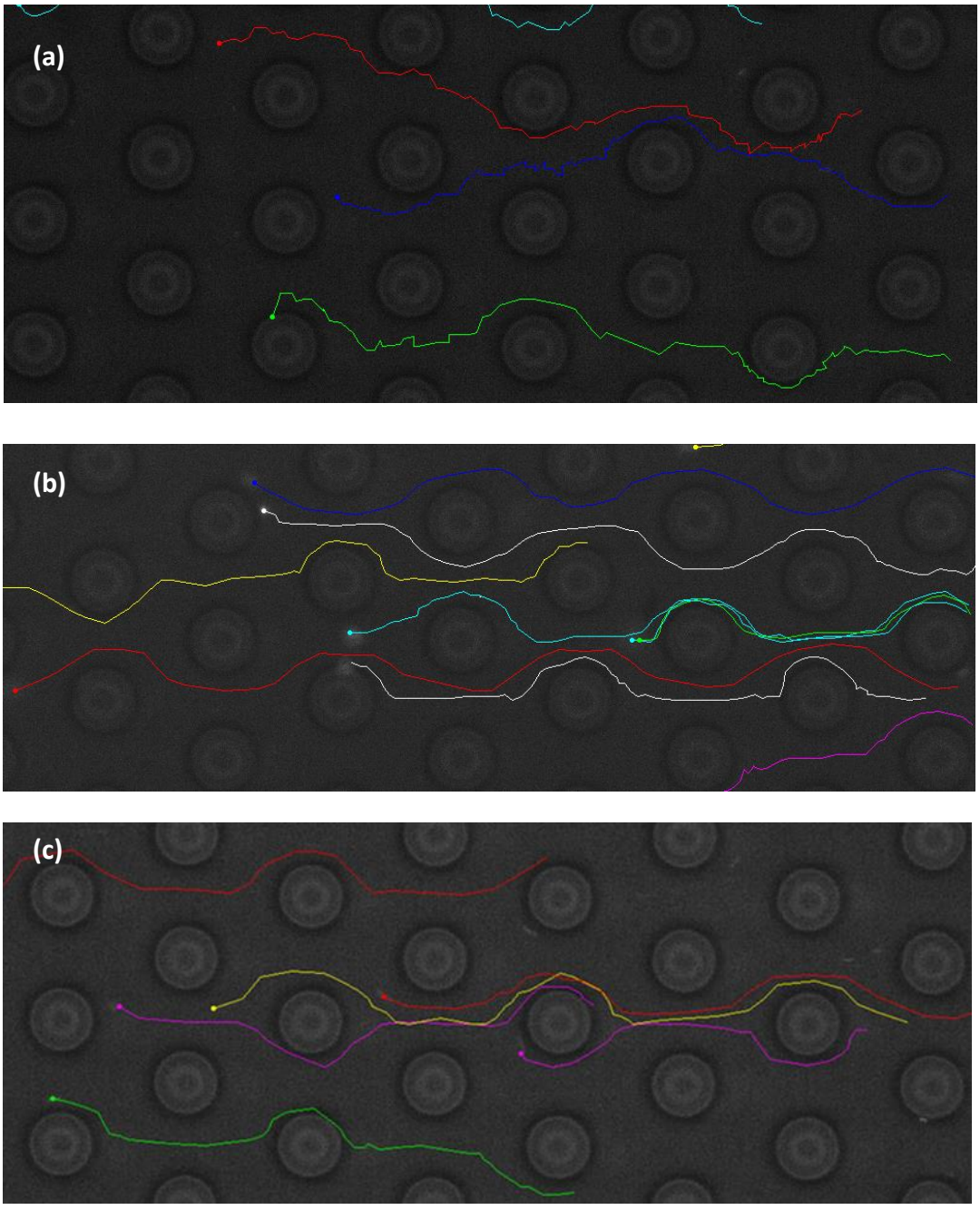

Figure B.7. Example of 200nm particle trajectory, 10-10 micromodel, at (a) Slow, (b) Intermediate and (c) High flow rates

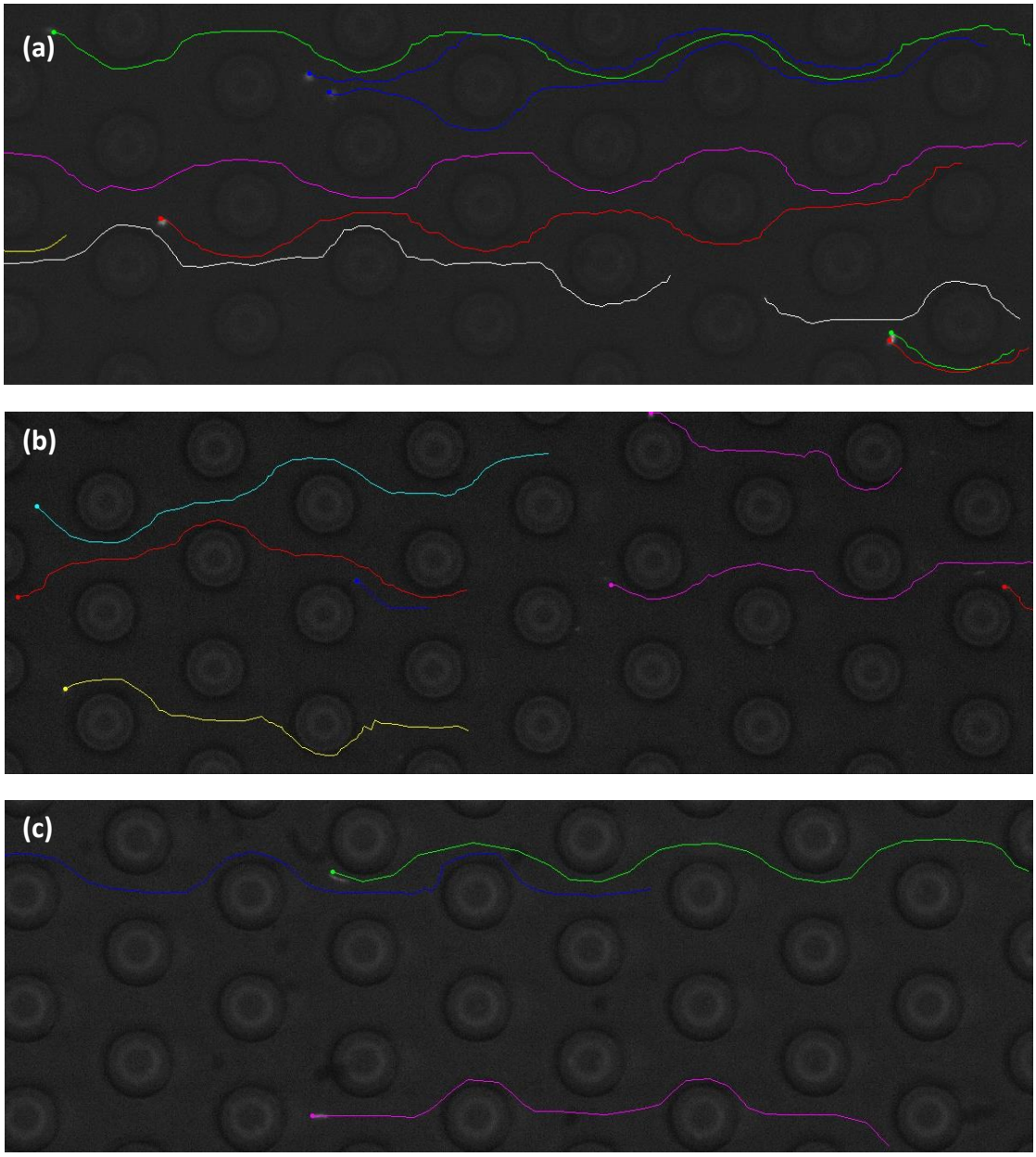

Figure B.8. Example of 500nm particle trajectory, 10-10 micromodel, at (a) Slow, (b) Intermediate and (c) High flow rates

APPENDIX C

POTENTIAL SOURCES OF ERRORS

Although all efforts were made to conduct the experiments in a diligent and consistent manner, there are potential errors inherent in the experimental work.

Errors involved in K_L computations consist of experimental errors, data processing errors and calculation errors. Experimental errors can occur because of inconsistency of the flow rate in micromodel (syringe, syringe pump, movement of tubes, etc). Data processing errors deals with errors in counting the particles because the procedure is manual and due to dealing with high concentrations sometimes it is not possible to distinguish two adjacent particles. And more than one particle might be assigned as one. Although particles are engineered in a way that they do not tend to aggregate, due to high concentrations it is possible to have some aggregations which will cause wrong assignment of clusters instead of individual particles.

APPENDIX D

IMAGE RECORDING TIMES FOR DILUTE SUSENSIONS

In the table below, the times (in minutes) at which still pictures were taken after suspensions were admitted to the test cell are reported. The first time is the time recording at the inlet and the second picture taken at the centre of the micro-model was approximately 0.1 minutes after the first picture.

Table D1. Image recording times

Conf. I	200nm	500nm	1500nm
Slow	23.1	23.2	23.2
Int.	7.7	7.8	7.8
Fast	4.1	4.1	4.1
Conf. II	200nm	500nm	1500nm
Slow	25	24	23.2
Int.	8.9	8.2	7.8
Fast	4.5	4.2	4.1
Conf. III	200nm	500nm	1500nm
Slow	23.2	23.1	22.9
Int.	7.8	7.7	7.7
Fast	4.1	4.1	4.1